ABSTRACT

Title of Dissertation: Near-Field Magnetic Microwave Microscope Studies of Vortex Dynamics in Superconductors

Chung-Yang Wang
Doctor of Philosophy, 2025

Dissertation Directed by: Professor Steven M. Anlage
Department of Physics

Superconductors host vortices when exposed to a magnetic field exceeding their first critical field B_{c1}. Understanding the dynamics of vortices is crucial for optimizing the performance of various applications of superconductors, including superconducting radio-frequency (SRF) cavities and superconducting digital and quantum circuits. In this thesis, a near-field magnetic microwave microscope is employed to locally stimulate superconductors with an intense rf magnetic field and measure the local nonlinear microwave response. Under the microscope probe, two distinct vortex-related phenomena are observed: the nucleation of rf vortices and the motion of pre-existing trapped vortices. To interpret the measured response, toy models of superconductors with local defects are introduced and analyzed using Time-Dependent Ginzburg-Landau (TDGL) simulations of probe/sample interactions.

This dissertation is divided into two parts. The first part investigates the nucleation of single/few rf vortices associated with surface defects by studying the third-harmonic response P_{3f} produced by the superconductor under intense stimulus at frequency f. Seven Nb/Cu films, grown

under different deposition conditions by collaborators at CERN, are measured. Their surface defect properties related to rf vortex nucleation are compared. The second part explores the dynamics of trapped vortices under oscillating magnetic fields by studying the second-harmonic response $P_{2\mathrm{f}}$. A superconducting Nb film with an antidot flux pinning array is measured. The results show that this measurement technique provides access to vortex dynamics at the micron scale, including depinning events of a small number of trapped vortices and spatially-resolved pinning properties. These findings contribute to a deeper understanding of microwave superconductivity and vortex-induced nonlinearities, shedding light on the fundamental interactions between rf fields, magnetic vortices, and defects in superconductors. Furthermore, they offer new insights into the design and optimization of superconducting devices for microwave applications.

Near-Field Magnetic Microwave Microscope Studies of Vortex Dynamics in Superconductors

by

Chung-Yang Wang

Dissertation submitted to the Faculty of the Graduate School of the
University of Maryland, College Park in partial fulfillment
of the requirements for the degree of
Doctor of Philosophy
2025

Advisory Committee:
Professor Steven M. Anlage, Chair/Advisor
Professor Johnpierre Paglione
Professor Nicholas P. Butch
Professor Aaron Sternbach
Professor Ichiro Takeuchi

Acknowledgments

This dissertation marks the end of a long and transformative journey, one filled with challenges, growth, and discovery. I could not have completed it without the support, encouragement, and patience of many people. I am deeply grateful to everyone who shared their wisdom, stood by me through difficult moments, and helped make this journey not only possible, but meaningful.

First of all, I want to thank my advisor, Professor Steven M. Anlage. Professor Anlage is both passionate and deeply supportive. As someone trained in theoretical physics from age 18 to 28, I faced a difficult transition when I switched to experimental physics at the end of my second year of graduate study. I knew almost nothing about microwave measurements, but Professor Anlage generously welcomed me into the world of microwave experiments, guiding me through everything from big-picture concepts to hands-on technical details. I still remember bringing him a set of experimental data that looked very strange during one of our regular meetings in my first semester in the lab. Instead of brushing it off, he came to the lab, patiently inspected the entire setup with me, and quickly identified the issue: a loose cable. His attention to detail, willingness to teach, and supportive presence have had a lasting impact on my growth as a physicist.

I thank the other committee members, Professor Johnpierre Paglione, Professor Nicholas P. Butch, Professor Aaron Sternbach, and Professor Ichiro Takeuchi for generously offering their time to review the thesis and serve on my defense committee.

I thank our collaborators for providing superconducting samples. I measure several Nb/Cu

films provided by collaborators at CERN, including Carlota Pereira, Stewart Leith, and Guillaume Rosaz. I also measure two Nb3Sn films provided by collaborators at Cornell University, including Matthias Liepe, Zeming Sun, and Thomas Oseroff.

I thank Javier Guzman from Seagate Technology for providing magnetic write heads. I thank the U.S. Department of Energy/High Energy Physics (grant No. DESC0017931), ARO/FSDL (grant ARO W911NF-24-1-0153), and the Maryland Quantum Materials Center.

I would like to thank all my labmates in the group: Bakhrom Oripov, Seokjin Bae, Tamin Tai, Shukai Ma, Lei Chen, Cougar Garcia, Jingnan Cai, Arthur Carlton-Jones, Jared Erb, Izel Giovannelli, Nadav Shaibe, Yilin Li, Daniil Ivannikov, and Khaled Keshk. In particular, I want to thank Bakhrom Oripov and Jingnan Cai. I continued the microwave microscope project that Bakhrom had been working on, and he taught me a great deal about the project during my first few months in the lab. Over the past five years, Jingnan has helped me a lot, from practical training on microwave equipment to using 3D design software. I truly appreciate their generosity with their time, experience, and knowledge.

Last but not least, I want to thank my family and friends for their strong support throughout this journey. It is not easy to study abroad, halfway across the Earth from home, and I am deeply grateful for their constant encouragement and emotional support. Their presence, near or far, has kept me grounded and given me strength during the most challenging times.

Table of Contents

List of Tables

List of Figures

List of Abbreviations

AFM	Atomic Force Microscopy
a.u.	Arbitrary Unit
BCS	Bardeen-Cooper-Schrieffer
Cu	Copper
dB	Decibel
dBm	Decibel Milliwatts
DC	Direct Current
GHz	GigaHertz
GL	Ginzburg-Landau
MHz	MegaHertz
MW	Microwave
Nb	Niobium
Nb_3Sn	Tri-Niobium Tin
NFMM	Near-Field Microwave Microscopy
NFMMM	Near-Field Magnetic Microwave Microscopy
PCB	printed circuit board
RBW	Resolution Bandwidth
rf	Radio Frequency
RSJ	Resistively Shunted Junction
SEM	Scanning Electron Microscope
SMA	SubMiniature version A
SPM	Scanning Probe Microscopy
SRF	Superconducting Radio-Frequency
TDGL	Time-Dependent Ginzburg-Landau

UMD University of Maryland

VBW Video Bandwidth

List of Papers

1. Chung-Yang Wang, Carlota Pereira, Stewart Leith, Guillaume Rosaz, and Steven M. Anlage, "Microscopic examination of rf-cavity-quality niobium films through local nonlinear microwave response," *Physical Review Applied* 22:054010, Nov 2024. DOI: https://doi.org/10.1103/PhysRevApplied.22.054010

2. Chung-Yang Wang and Steven M. Anlage, "Near-field nonlinear microwave microscope for fundamental superconducting studies," in *2024 IEEE/MTT-S International Microwave Symposium - IMS 2024*, pages 998–1001, 2024. DOI: 10.1109/IMS40175.2024.10600280

3. Chung-Yang Wang and Steven M. Anlage, "Microwave microscope studies of trapped vortex dynamics in superconductors," *arXiv preprint* arXiv:2503.02811, 2025. DOI: 10.48550/arXiv.2503.02811

List of Presentations

1. 2025 APS March Meeting, "Probing Trapped Vortices in Superconductors with Near-Field Magnetic Microwave Microscopy," March 19, 2025

2. 2024 The Applied Superconductivity Conference, "A New Near-Field Microwave Microscopy Approach to Exploring Trapped Vortices in Superconductors," September 3, 2024

3. 2024 International Microwave Symposium, "Near-Field Nonlinear Microwave Microscope for Fundamental Superconducting Studies," June 20, 2024

4. 2024 APS March Meeting, "Probing Trapped Vortices in Superconductors Using Local Microwave Stimulation," March 6, 2024

5. The 21st International Conference on Radio-Frequency Superconductivity (SRF 2023), "Nonlinear Microwave Microscopy of Superconducting Radio Frequency Accelerator Cavity Materials," June 25, 2023

6. 2023 APS March Meeting, "Microscopic Investigation of Nonlinear Microwave Response of Nb_3Sn in the Superconducting State," March 8, 2023

7. 2022 APS March Meeting, "Microscopic Investigation of Nb Film Impurities by Nonlinear Microwave Response," March 14, 2022

8. 2021 APS March Meeting, "Investigation of Local Nonlinear Microwave Response of Nb_3Sn in the Superconducting State," March 19, 2021

Chapter 1: Introduction

1.1 Introduction to Vortices in Superconductors

1.1.1 Fundamental Properties of Superconductors

Superconductivity is a macroscopic quantum phenomenon characterized by the complete disappearance of electrical resistance and the expulsion of magnetic fields (the Meissner effect) when a material is cooled below its critical temperature, T_c [1]. These remarkable properties arise from the formation of Cooper pairs [2], bound pairs of electrons that collectively condense into a macroscopic quantum state, leading to a dissipationless supercurrent.

A central concept in superconductivity is the order parameter, $\psi(x, y, z)$, which describes the local density and phase coherence of the superconducting state. In the Ginzburg-Landau (GL) theory [3], the magnitude of the order parameter provides a measure of the strength of superconductivity at a given point. The characteristic length scale over which the order parameter varies is known as the coherence length, $\xi(T)$, which defines the minimum size over which superconductivity can spatially change. Another fundamental length scale is the London penetration depth, $\lambda(T)$, which characterizes how deeply an external magnetic field can penetrate into a superconductor before being screened by supercurrents. These two length scales, ξ and λ, play a crucial role in determining the response of a superconductor to external magnetic fields.

When a superconductor is subjected to an external magnetic field, its behavior depends on the ratio of λ to ξ. This ratio, known as the Ginzburg-Landau parameter, $\kappa = \lambda/\xi$, classifies superconductors into two types:

- Type-I superconductors ($\kappa < 1/\sqrt{2}$) exhibit a complete Meissner effect, expelling magnetic fields up to a critical field, B_{c}, beyond which the material transitions to a normal state.
- Type-II superconductors ($\kappa > 1/\sqrt{2}$) allow partial magnetic field penetration beyond a first critical field, B_{c1}, where quantized flux lines known as vortices begin to form.

1.1.2 Vortex Structure and Vortex Penetration Field

A vortex consists of a normal-conducting core of radius $\sim \xi$, where superconductivity is strongly suppressed, surrounded by circulating supercurrents that screen the applied field over a distance λ. The order parameter $|\psi|$ is significantly reduced in the vortex core, approaching zero at its center, and recovers to its equilibrium value over a length scale ξ. Each vortex carries a single quantum of magnetic flux, $\Phi_0 = h/2e$, where h is Planck's constant and e is the elementary charge. As the applied field increases beyond a second critical field, $B_{\mathrm{c2}}(T)$, the vortex density increases until superconductivity is entirely suppressed.

In an ideal, defect-free superconductor, vortices begin to penetrate at the first critical field $B_{\mathrm{c1}}(T)$. However, in the presence of surface defects, vortices can nucleate at fields lower than B_{c1}. The field at which vortices first enter due to such imperfections is called the vortex penetration field $B_{\mathrm{vortex}}(T)$, which serves as a generalized form of the first critical field that accounts for local defects. This field depends on the nature of the defects, including their size, shape, and local suppression of superconductivity.

1.2 Microwave Properties of Vortices

1.2.1 Microwave Superconductivity

Superconductors exhibit unique electromagnetic properties that make them highly advantageous for microwave applications [4]. Unlike normal metals, which experience significant ohmic losses at high frequencies, superconductors can exhibit ultra-low surface resistance in the microwave regime, particularly at temperatures well below their critical temperature. This ability to sustain extremely low surface resistance at microwave frequencies enables superconducting radio-frequency (SRF) cavities used in particle accelerators with extraordinarily high quality factors (Q), often exceeding 10^{11} [5].

The microwave regime typically refers to the frequency range from 300 MHz (0.3 GHz) to 300 GHz, corresponding to wavelengths between 1 meter and 1 millimeter. Within this range, superconducting microwave devices operate in specific frequency windows depending on the application. For example, SRF cavities used in particle accelerators typically operate at frequencies between 0.5–4 GHz [5].

The electrodynamics of superconductors at microwave frequencies is governed by the interplay of superfluid screening currents, quasi-particle excitations, and nonlinear effects. The two-fluid model provides a phenomenological description, treating the superconductor as a combination of a lossless superfluid component and a dissipative normal-fluid component. At sufficiently low temperatures and frequencies below the superconducting energy gap Δ (specifically, $hf \ll 2\Delta$), microwave losses are exponentially suppressed due to the scarcity of thermally excited quasi-particles. These properties underpin a wide range of microwave technologies, including

high-performance resonators, superconducting transmission lines, and Josephson-based quantum circuits.

In this thesis, the terms “rf” and “microwave” are used interchangeably. The abbreviation “rf” stands for radio-frequency.

1.2.2 Microwave Response of Vortices

In type-II superconductors, the response to microwave fields becomes significantly more complex due to the presence of vortices. Unlike the dissipationless superfluid current, vortex motion under microwave excitation introduces additional dissipation, since the core of a vortex is normal-conducting.

The dynamics of vortices in microwave fields plays a central role in vortex-based dissipation and nonlinear microwave response. At low amplitudes, vortices exhibit a linear response, characterized by a viscous drag force proportional to their velocity. However, at high microwave fields, the interaction between the rf current and vortices becomes highly nonlinear, leading to phenomena such as harmonic generation, intermodulation distortion, etc.

1.3 Core Questions and Research Scope

In this thesis, we explore the following Core Questions:

- **Core Question 1:** What vortex-related phenomena can occur when a superconductor is stimulated by an oscillating magnetic field in the microwave regime (a few GHz)?
- **Core Question 2:** What information can be extracted from the resulting microwave response of the superconductor?

To address these questions, we consider two distinct scenarios:

- **Scenario 1:** If the amplitude of an oscillating magnetic field exceeds the vortex penetration field of the superconductor, it nucleates rf vortices. This phenomenon is discussed in Chapters 4 (simulations) and 5 (measurements), where we analyze the third-harmonic response (P_{3f}) as a tool for studying rf vortex nucleation. This scenario is explored in Ref. [6].

- **Scenario 2:** Pre-existing DC vortices are subjected to an oscillating magnetic field. This scenario is studied in Chapters 6 (simulations) and 7 (measurements), where we investigate the second-harmonic response (P_{2f}) associated with the dynamics of trapped vortices. This scenario is explored in Ref. [7].

A key distinction between DC vortices and rf vortices lies in their temporal behavior. A *DC vortex* is a stable, persistent object in the superconductor, whereas an *rf vortex* is transient, it nucleates and annihilates twice per rf cycle.

Figure 1.1 presents (over-simplified) schematic illustrating the transient nature of rf vortices in a superconductor subjected to an oscillating magnetic field. The red curve represents the applied magnetic field, $B_{\mathrm{rf}} \sin(\omega t)$, where the peak amplitude is set to be 1.5 times stronger than the first critical field of the superconductor, B_{c1}. The blue lines indicate $\pm B_{\mathrm{c1}}$. The superconductor alternates between the Meissner state (regions I, III, and V) and the vortex state (regions II and IV), depending on whether $|B_{\mathrm{rf}} \sin(\omega t)|$ exceeds B_{c1}. The black circles mark the transition points where $|B_{\mathrm{rf}} \sin(\omega t)| = B_{\mathrm{c1}}$, corresponding to vortex nucleation and annihilation events.

In reality, vortex nucleation and annihilation do not occur exactly at $|B_{\mathrm{rf}} \sin(\omega t)| = B_{\mathrm{c1}}$ due to the complex order parameter and vortex dynamics. Nevertheless, this simplified picture

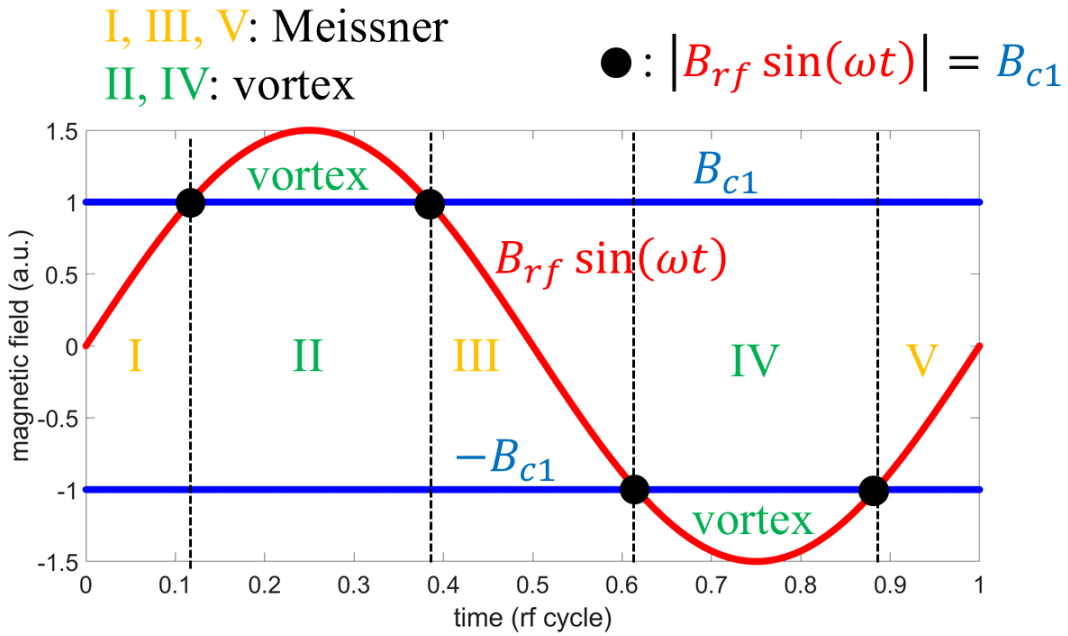

Figure 1.1: Illustration of the transient nature of rf vortices in a superconductor subjected to an oscillating magnetic field. The red curve represents the applied magnetic field, $B_{\rm rf}\sin(\omega t)$, where the peak amplitude is set to be 1.5 times stronger than the first critical field of the superconductor, $B_{\rm c1}$. The blue lines indicate $\pm B_{\rm c1}$.

effectively captures the essential mechanism of rf vortex nucleation. Unlike DC vortices, rf vortices are transient, they appear and disappear twice per rf cycle.

The first step toward analyzing the microwave response of vortices is to perform a Fourier transform, which decomposes the response into its fundamental and harmonic components. This approach provides a systematic way to extract key physical properties from experimental data. Section 1.4 introduces the Fourier framework and its application to superconducting vortex dynamics.

1.4 Linear Response, Odd Harmonic Response, Even Harmonic Response

1.4.1 Fourier Expansion and Harmonic Decomposition

The interaction of microwaves with a superconductor can be understood within the framework of a system driven by a sinusoidal driving force. The appropriate mathematical tool for analyzing its response is the Fourier transform. In the following, we explore the physical significance of these Fourier components in the context of superconducting microwave response.

Consider a system driven by a sinusoidal driving force with angular frequency ω, where the response function is denoted as $f(t)$. The Fourier expansion of $f(t)$ is given by

$$f(t) = \sum_{n=0}^{\infty} c_n \sin(n\omega t + \theta_n). \tag{1.1}$$

This expansion can be decomposed into three distinct components:

$$f(t) = \text{offset} + \text{linear response} + \text{nonlinear response}. \tag{1.2}$$

The nonlinear response further consists of contributions from both odd and even harmonics:

$$\text{nonlinear response} = \text{odd harmonic response} + \text{even harmonic response}. \tag{1.3}$$

Each of these terms is explicitly given by

$$\text{offset} = c_0, \tag{1.4}$$

$$\text{linear response} = c_1 \sin(\omega t + \theta_1), \tag{1.5}$$

$$\begin{aligned}\text{odd harmonic response} &= \sum_{n=1}^{\infty} c_{2n+1} \sin\left[(2n+1)\omega t + \theta_{2n+1}\right] \\ &= c_3 \sin(3\omega t + \theta_3) + c_5 \sin(5\omega t + \theta_5) + \ldots \end{aligned} \tag{1.6}$$

$$\begin{aligned}\text{even harmonic response} &= \sum_{n=1}^{\infty} c_{2n} \sin\left[2n\omega t + \theta_{2n}\right] \\ &= c_2 \sin(2\omega t + \theta_2) + c_4 \sin(4\omega t + \theta_4) + \ldots \end{aligned} \tag{1.7}$$

Here, the *offset term* represents the DC component of the response, while the *linear response* corresponds to the fundamental frequency component, which is directly proportional to the input signal. The *nonlinear response* consists of higher-order harmonics that arise from system nonlinearities. The *odd harmonic response* consists of terms with frequencies $(2n+1)\omega$, including the third-harmonic (3ω) and higher odd harmonics. In contrast, the *even harmonic response* consists of terms with frequencies $2n\omega$, including the second-harmonic (2ω) and higher even harmonics.

The presence and relative strength of these harmonic components provide insight into the underlying nonlinear mechanisms governing the system response.

As the leading-order term of odd harmonic responses, the third-harmonic response ($c_3 \sin(3\omega t + \theta_3)$) is frequently analyzed for studying odd harmonic response. Similarly, as the leading-order term of even harmonic responses, the second-harmonic response ($c_2 \sin(2\omega t + \theta_2)$) is frequently analyzed for studying even harmonic response.

The frequency of the sinusoidal driving force is denoted as f and is related to the angular frequency ω by

$$f = \frac{\omega}{2\pi}. \tag{1.8}$$

In this thesis, both f and ω are used frequently, depending on the context.

1.4.2 Microwave Response of Superconductors

In the context of this thesis, the system under study is a superconductor, the driving force is an oscillating magnetic field $B_{\mathrm{rf}}\sin(\omega t)$, and the response function $f(t)$ corresponds to the oscillating magnetic field generated by the superconductor, denoted as $B_{\mathrm{SC}}(t)$. The Fourier expansion of the superconductor response $B_{\mathrm{SC}}(t)$ is given by

$$B_{\mathrm{SC}}(t) = \sum_{n=0}^{\infty} B_{\mathrm{nf}} \sin(n\omega t + \theta_n). \tag{1.9}$$

where B_{nf} and θ_n correspond to the amplitude and phase of the nth harmonic component of the superconductor response $B_{\mathrm{SC}}(t)$, respectively. The subscript f in B_{nf} denotes frequency.

In principle, the full superconducting response $B_{\mathrm{SC}}(t)$ can be reconstructed by measuring all of its harmonic components. However, in practice, it is often sufficient—and far more efficient—to focus on the dominant terms. For example, when studying odd harmonic responses, the third-harmonic component, being the leading-order term, typically captures the most significant nonlinear effects and can provide valuable physical insight.

1.4.3 Linear versus Nonlinear Response

When a material experiences a small perturbation from an electromagnetic field, its response remains primarily linear. This regime includes measurements of local dielectric permittivity and electrical conductivity, where the material properties can be described by linear response theory. In contrast, when the applied electromagnetic field is sufficiently strong to significantly alter the material, nonlinear effects emerge. These nonlinear responses provide insights that are inaccessible through linear response measurements.

Vortex dynamics is inherently nonlinear, a feature that can be understood through a handwaving argument. In the vortex-free Meissner state, superconductivity varies smoothly across space, keeping the system well within the linear response regime. In contrast, the presence of vortices leads to strong suppression of superconductivity at the vortex core, representing a substantial deviation from the unperturbed Meissner state. This suppression is far beyond the scope of a small perturbation, indicating that the introduction of vortices fundamentally alters the superconducting state. Consequently, when vortices are subjected to an oscillating magnetic field, their dynamics inherently falls outside the linear response regime. As a result, nonlinear response measurements serve as a powerful tool for probing vortex dynamics and related phenomena.

In particular, for a type-II superconductor subjected to a strong rf magnetic field, the system enters a nonlinear regime where rf vortices are nucleated. This process gives rise to a pronounced third-harmonic response [6, 8–12], making third-harmonic measurements a powerful tool for studying rf vortex nucleation.

1.4.4 Odd versus Even Harmonic Response

Odd and even harmonic responses are fundamentally distinct due to their symmetry properties. In particular, even harmonic responses vanish when the response function $f(t)$ satisfies the symmetry condition

$$f(t) = -f\left(t + \frac{\pi}{\omega}\right). \tag{1.10}$$

This condition indicates that $f(t)$ exhibits perfect symmetry between the two half-cycles of the driving force. As a result, the presence of even harmonic responses directly reflects deviations from this symmetry, serving as a quantitative measure of *asymmetry* in the system dynamics between successive half-cycles of $f(t)$. In the context of superconducting response, the response function corresponds to the superconductor-generated magnetic field, i.e., $f(t) = B_{\mathrm{SC}}(t)$.

The response of a superconductor to an oscillating magnetic field, $B_{\mathrm{SC}}(t)$, can be classified based on symmetry (see Eq. 1.10) into two distinct categories: (i) linear response and odd harmonic responses and (ii) even harmonic responses. These two categories probe fundamentally different aspects of superconducting dynamics [13–22], with the former arising from dynamics that preserve symmetry between successive half-cycles and the latter serving as a signature of symmetry breaking in the superconducting response.

Linear response and odd harmonic responses [8–10, 23–30] capture contributions from a variety of mechanisms, including Meissner screening currents [31, 32], nonlinearities from current-dependent superfluid density variation, and rf vortex nucleation [6, 11]. In contrast, even harmonic responses [8, 24, 25, 33, 34] are known to vanish in the absence of time reversal invariance breaking [13, 15–17], such as when no DC magnetic field is applied and no vortices are trapped in

the superconductor. Notably, in the absence of an external offset (field or current), the second-harmonic response collects signals from trapped vortices exclusively, effectively filtering out contributions from other mechanisms. This exclusivity makes P_{2f} a powerful tool for studying trapped vortices [33].

1.5 A Microscopic Approach to Microwave Properties of Vortices

1.5.1 Limitations of Macroscopic Microwave Measurements

The study of microwave properties of superconductors has traditionally relied on *macroscopic* measurement techniques, such as resonator-based methods, transmission-line measurements, and cavity perturbation techniques [35, 36]. These methods have provided valuable insights into the global electrodynamics of superconductors, including their surface resistance, penetration depth, and nonlinearity. In particular, macroscopic studies have revealed the role of vortex motion in microwave dissipation and harmonic generation, helping to establish models for vortex dynamics in type-II superconductors [5, 37, 38].

While macroscopic measurements provide bulk-averaged responses, they fail to capture *local* variations in superconducting properties. In particular, surface defects, grain boundaries, and spatially inhomogeneous vortex pinning can strongly influence the microwave response of superconductors. Since vortex nucleation, motion, and pinning occur at microscopic scales comparable to the coherence length ξ and penetration depth λ, a detailed understanding of these processes requires a *microscopic* measurement technique capable of resolving local variations in microwave response.

1.5.2 Near-Field Magnetic Microwave Microscopy: A Local Probe

To address these limitations, we employ a Near-Field Magnetic Microwave Microscope (NFMMM) [39, 40], a homemade scanning probe system designed to measure the *spatially-resolved* microwave properties of superconductors. This technique allows us to *locally excite and detect* nonlinear responses, providing direct insight into vortex dynamics in the microwave regime.

At a fundamental level, NFMMM applies a localized rf magnetic field at the tip of a probe, which interacts with the superconducting sample beneath it, and collects locally-generated microwave response. The key steps in this process are:

1. A microwave input signal is delivered to the probe, generating a localized rf magnetic field at its tip.

2. The superconducting sample beneath the probe responds with a screening current, which distributes according to the local superconducting properties.

3. The same microscope probe collects the response microwave field associated with the screening current, which carries information about the local superconducting properties.

4. By analyzing the nonlinear responses ($P_{2\mathrm{f}}$ and $P_{3\mathrm{f}}$), we extract information about local properties of vortex dynamics.

1.5.3 Measurement of Harmonic Response Power

A key aspect of our measurements is that we measure the *power* of the nonlinear response (denoted as P_{nf}), rather than its phase. The power P_{nf} is proportional to the squared amplitude of

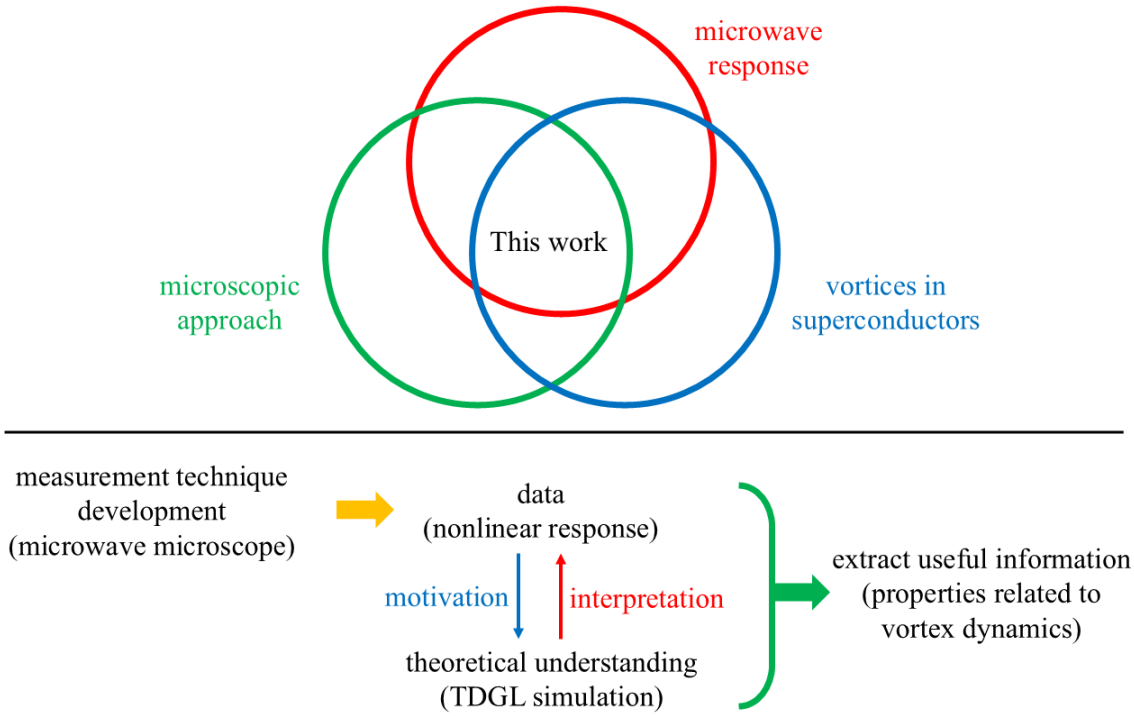

Figure 1.2: Conceptual framework of this thesis. Note that the color scheme in the top and bottom diagrams is independent—colors do not share a common meaning between the two figures.

the corresponding Fourier component of $B_{\mathrm{SC}}(t)$:

$$P_{\mathrm{nf}} \propto |B_{\mathrm{nf}}|^2 . \tag{1.11}$$

Despite the absence of phase information, the power of the harmonic response serves as an effective indicator of microwave-induced vortex motion. By correlating NFMMM measurements with simulations, we gain deeper insight into the microscopic origins of nonlinear microwave response in superconductors.

1.6 Thesis Overview and Research Approach

Since the NFMMM is a homemade system, it is crucial to develop a detailed understanding of what physically occurs beneath the probe. While experimental measurements provide direct observations of the nonlinear response, interpreting these results requires a deeper theoretical framework. To achieve this, we perform numerical simulations using toy models to gain insight into vortex dynamics and the resulting nonlinear microwave response. These simulations allow us to:

- Validate and interpret experimental measurements by comparing them with theoretical predictions.
- Investigate how vortices respond to localized microwave excitation under different conditions.
- Extract meaningful physical quantities from the measured harmonic response.

Figure 1.2 summarizes the conceptual framework of this thesis. The Venn diagram (top) illustrates the interdisciplinary nature of this work, which lies at the intersection of microwave response, vortices in superconductors, and a microscopic measurement approach. The schematic diagram (bottom) outlines the research methodology, integrating experimental data from NFMMM with theoretical insights from time-dependent Ginzburg-Landau (TDGL) simulations. Note that the color scheme in the top and bottom diagrams is independent—colors do not share a common meaning between the two figures.

The "measurement technique development" part of Fig. 1.2 is discussed in Appendix B. The main focus of this thesis is the remaining aspects shown in Figure 1.2, namely, performing nonlinear response measurements with a homemade NFMMM, conducting TDGL simulations, and

Introduction (Chapter 1)
Experimental setup (Chapter 2)
TDGL framework (Chapter 3)

	rf vortex nucleation and P_{3f}	Trapped vortex dynamics and P_{2f}
TDGL simulations	Chapter 4	Chapter 6
Experimental results	Chapter 5	Chapter 7

Conclusion (Chapter 8)

Figure 1.3: Overview of the thesis structure. See Sec. 1.7 for a detailed description.

extracting useful information about vortex dynamics. By combining experiment and simulation, we ensure a more comprehensive understanding of how superconducting vortices interact with localized rf magnetic fields, allowing us to extract valuable insights from the measured nonlinear response.

1.7 Outline of the Thesis

This thesis is structured as follows (summarized in Fig. 1.3):

- **Chapter 2** discusses the experimental setup of our Near-Field Magnetic Microwave Microscope (NFMMM). This includes details of the microscope probe, rf signal delivery, detection scheme, and spatial resolution, providing the necessary background for understanding the experimental results presented in later chapters.

- **Chapter 3** introduces the theoretical framework of the Time-Dependent Ginzburg-Landau (TDGL) theory and the simulation workflow used in this thesis. The chapter describes the governing equations, numerical implementation, and boundary conditions for simulating vortex dynamics under microwave excitation.

- **Chapter 4** presents TDGL simulations of rf vortex nucleation caused by surface defects and the resulting third-harmonic response (P_{3f}).

- **Chapter 5** presents the experimental results from seven Nb/Cu films intended for use in SRF accelerator cavity applications, focusing on rf vortex nucleation induced by surface defects through measurements of the third-harmonic response (P_{3f}). This chapter compares the films in terms of their effectiveness in suppressing rf vortex nucleation caused by surface defects.

- **Chapter 6** presents TDGL simulations of trapped vortex dynamics and the resulting second-harmonic response (P_{2f}).

- **Chapter 7** presents experimental results on a Nb film with an antidot flux pinning array, which is a prototype for flux moats used in superconducting digital and quantum computing applications. The focus is on trapped vortex dynamics and pinning properties, which are analyzed through measurements of the second-harmonic response (P_{2f}).

- **Chapter 8** concludes the thesis with a summary of key findings, implications for microwave vortex dynamics, and potential directions for future research.

In addition to the seven Nb/Cu films studied in Chapter 5, third-harmonic response measurements are also performed on two Nb_3Sn films, as presented in Appendix E.

The studies presented in Chapters 4 (simulations) and 5 (measurements) are published in Ref. [6], while the work in Chapters 6 (simulations) and 7 (measurements) is covered in Ref. [7].

Chapter 2: Near-Field Magnetic Microwave Microscopy

2.1 Overview of Near-Field Microwave Microscopy

Near-field microwave microscopy (NFMM) is a type of scanning probe microscopy (SPM) [41, 42] that utilizes microwaves to probe the electrodynamic response of materials [39, 40, 43]. The term "near-field" refers to the regime where the characteristic length scales of electromagnetic interactions, determined by the probe size and probe-sample separation, are much smaller than the free-space wavelength of the radio-frequency (rf) signal used for measurement. For example, a 1 GHz electromagnetic wave has a free-space wavelength of 30 cm, whereas typical NFMM probe sizes range from the nanoscale to the sub-micron scale.

By operating in the near-field regime, NFMM achieves subwavelength resolution beyond the diffraction limit by positioning a sharp probe in close proximity to the sample. In this regime, the electromagnetic field exhibits spatial variations dependent on the probe geometry and surrounding environment, while its instantaneous value oscillates at the rf frequency.

NFMM typically operates in a reflectometry mode, where microwaves are transmitted to the sample via a sharp probe, and the reflected signal is measured. This technique enables the study of inhomogeneous electromagnetic properties with nanoscale resolution across the GHz regime. Specifically, it is widely used for imaging local dielectric permittivity and electrical conductivity in high-impedance samples [44–48]. Depending on the probe design, NFMM-sample coupling

can be either capacitive (dominated by the electric field) or inductive (dominated by the magnetic field).

NFMM of materials properties [39, 40, 43, 49–63] has also proven to be very helpful in the study of superconducting microwave devices [4, 64–66]. For investigating the surface electrodynamics of a superconductor, the central theme of this thesis, inductively coupled probes are preferable, as they induce screening currents near the superconductor surface. Over the years, multiple generations of near-field magnetic microwave microscopes (NFMMs with magnetically dominated probe-sample coupling) have been developed in our group at UMD, as reviewed in Sec. 2.2.

2.2 Previous Generations of Near-Field Magnetic Microwave Microscopes

Members of the Anlage lab have been studying both the linear and nonlinear responses of superconductors using homemade near-field magnetic microwave microscopes (NFMMM) for over two decades. During this time, the resolution of the microscope probe has been continuously improved, and the experimental setup has undergone multiple upgrades.

The first NFMMM in our group was built by Sheng-Chiang Lee [23]. The microscope consists of a driven resonant coaxial transmission line connected to a Cu loop (loop probe), formed by shorting the inner conductor of a coaxial cable to the outer conductor. In addition to measuring the linear response [23], Lee used the microscope to study the nonlinear response. Specifically, he investigated the nonlinear Meissner effect [25] and imaged both the second-harmonic response P_{2f} and the third-harmonic response P_{3f} across the grain boundary of a YBCO film [8, 24, 67].

Dragos Mircea used the loop probe-based microscope to study the third-harmonic response

of a YBCO thin film [9]. In addition to measuring its amplitude, he also examined its phase and found a significant temperature dependence for T near T_c.

The next iteration of the NFMMM utilizes a conventional hard disk drive magnetic writer probe as its magnetic probe. This magnetic writer probe-based microscope was developed by Tamin Tai and Dragos Mircea [27]. Tamin used it to study the third-harmonic response of bulk Nb [10, 29]. Additionally, he investigated both the amplitude and phase of the linear response [30] and the third-harmonic response [28] of Nb films.

Finally, Bakhrom Oripov used the magnetic writer probe-based microscope to study several SRF-grade Nb samples [11, 68]. By measuring the third-harmonic response, he identified the surface defects of these samples. Additionally, he performed calculations based on the current-biased resistively shunted junction (RSJ) model [11] and numerical simulations based on the time-dependent Ginzburg-Landau (TDGL) model [12] to better interpret the measurement results.

The near-field magnetic microwave microscope I use [6, 7, 69] is similar to those used by Tai and Oripov. The magnetic writer probe, the core component of the microscope, is discussed in Sec. 2.3. The cryostat, measurement circuit, and electronics of the microscope are described in Sec. 2.4, and are similar to the Oripov setup [68].

2.3 Magnetic Writer Probe from Hard Disk Drive

The core component of our near-field magnetic microwave microscope is the magnetic writer probe, originally designed for magnetic reading and writing in conventional hard disk drives used in magnetic recording technology [70]. A magnetic writer consists of a magnetic medium and a magnetic writer head, which encodes information by locally magnetizing the medium. The

magnetic writer head is sub-micron in size and generates a localized magnetic field with both longitudinal and perpendicular components. The probe is engineered to operate with a GHz bandwidth.

In magnetic recording technology, the magnetic writer probe flips domains in a magnetized medium and creates permanent changes to the medium. In our microwave microscope, the probe is placed in a cryogenic environment and stimulated with GHz signals, and the material beneath it is a superconductor rather than a magnetized medium. We investigate how the superconductor responds when stimulated by the rf magnetic field generated by the probe.

Figure 2.1 presents images of the magnetic writer probe used in our near-field magnetic microwave microscope. We received tens of magnetic writer probes from Javier Guzman of Seagate Technology. As shown in Fig. 2.1(a), the probe consists of a slider, transmission lines, and an aluminum assembly that holds these components together. The slider, as shown in Fig. 2.1(b), houses the magnetic writer head, the primary functional element of the probe. The magnetic writer head is capable of generating a localized rf magnetic field, making it particularly well-suited for our microwave microscope. Figure 2.1(c) shows a scanning electron microscope (SEM) image of the magnetic writer head, with the surrounding magnetic shielding highlighted by a yellow circle. The yellow box in Fig. 2.1(c) provides a magnified view, focusing specifically on the magnetic writer head.

In our microwave microscope setup, a coaxial connector is directly soldered to soldering pads 3 and 4 at the end of the transmission lines of the probe. Figure 2.1(d) shows the soldering pads of an unused probe, while Fig. 2.1(e) shows soldering pads 3 and 4 with solder applied on a used probe. The connection can be checked by measuring the resistance between pads 3 and 4 which is $R_{\text{writer}} \approx 6\ \Omega$ at room temperature.

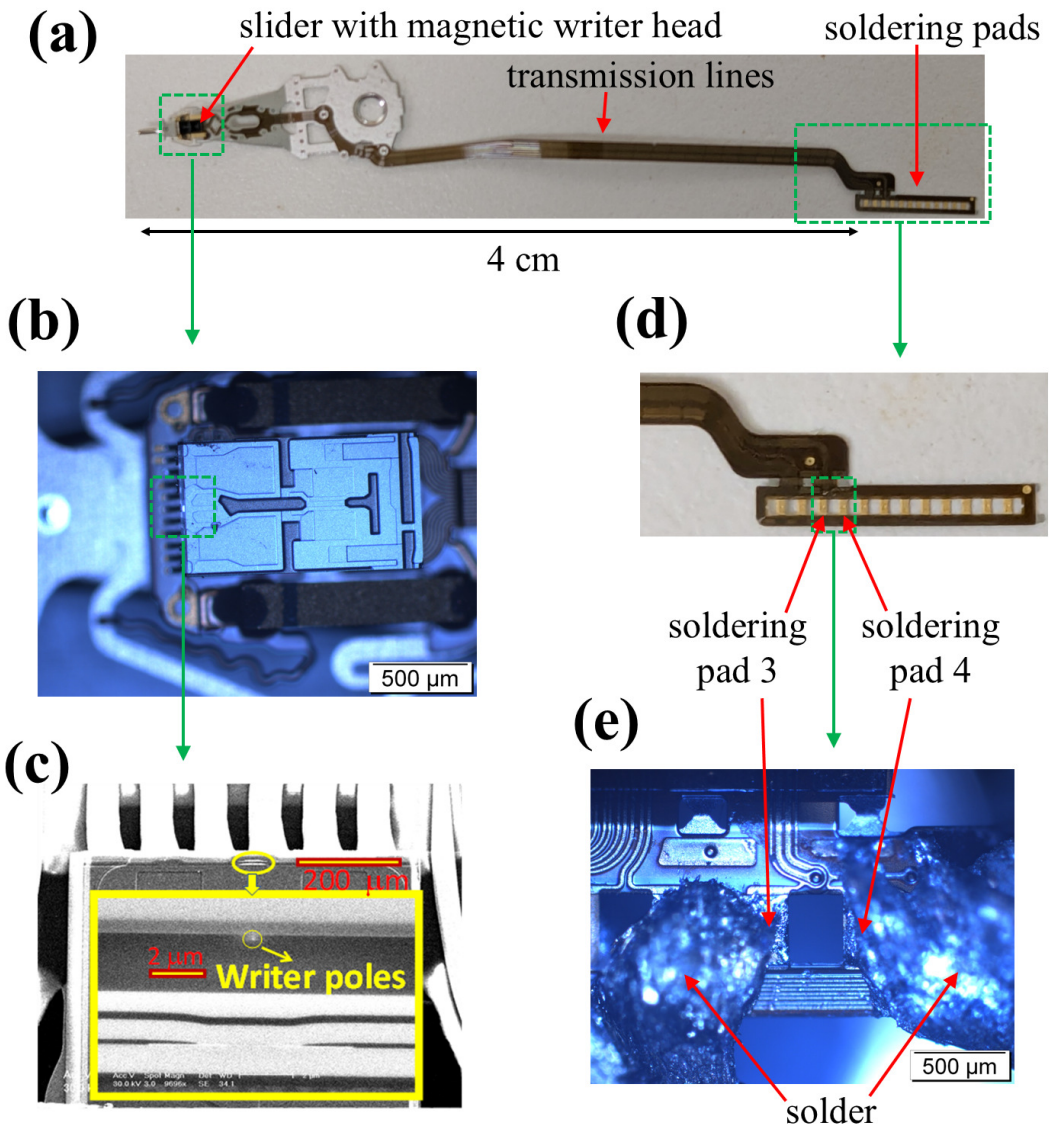

Figure 2.1: Images of the magnetic writer probe used in our near-field magnetic microwave microscope. (a) Photograph of the magnetic writer probe. (b) Optical microscope image of the slider region. (c) SEM image of the magnetic writer head. (d) Photograph of the soldering pads. (e) Optical microscope image of soldering pads 3 and 4, showing solder connections to an SMA coaxial connector (the connector is not shown here).

Typical solder contains lead, which becomes superconducting below its critical temperature of 7.2 K and thus can introduce unwanted nonlinearities for $T < 7.2$ K. To ensure that the measured nonlinearity originates from the sample rather than the measurement circuit, we use lead-free solder to connect the coaxial connector to the probe.

2.4 Experimental Setup

2.4.1 Overview of the Near-Field Magnetic Microwave Microscope Setup

The near-field magnetic microwave microscope setup consists of a magnetic writer probe integrated into a dry cryostat purchased from Entropy. Figure 2.2(a) presents a schematic of the setup, while Figs. 2.2(b) and (c) show photographs of the side and top views of the microscope head. Figure 2.3 displays photographs of a typical experimental setup below the 4 K cold plate, focusing on the microscope head. Figure 2.4 provides photographs of the Entropy cryostat and the relevant electronics.

The Entropy cryostat (represented by the green dashed box in Fig. 2.2(a)) has three plates: a room temperature top plate, a 70 K plate, and a 4 K cold plate. Each plate is equipped with a corresponding vacuum can. The microscope head (see Fig. 2.2(b) and (c)) is positioned below, and thermally anchored to, the 4 K cold plate (see Fig. 2.3). The superconducting sample and the thermometer (close to the sample) are both directly mounted on the 4 K cold plate to ensure good thermalization, as shown in Fig. 2.3. The base temperature for a sample in the cryostat is around 3.6 K.

A typical experimental setup below the 4 K cold plate is shown in Fig. 2.3. The superconducting samples consist of seven Nb films deposited on a common Cu substrate, which are studied in

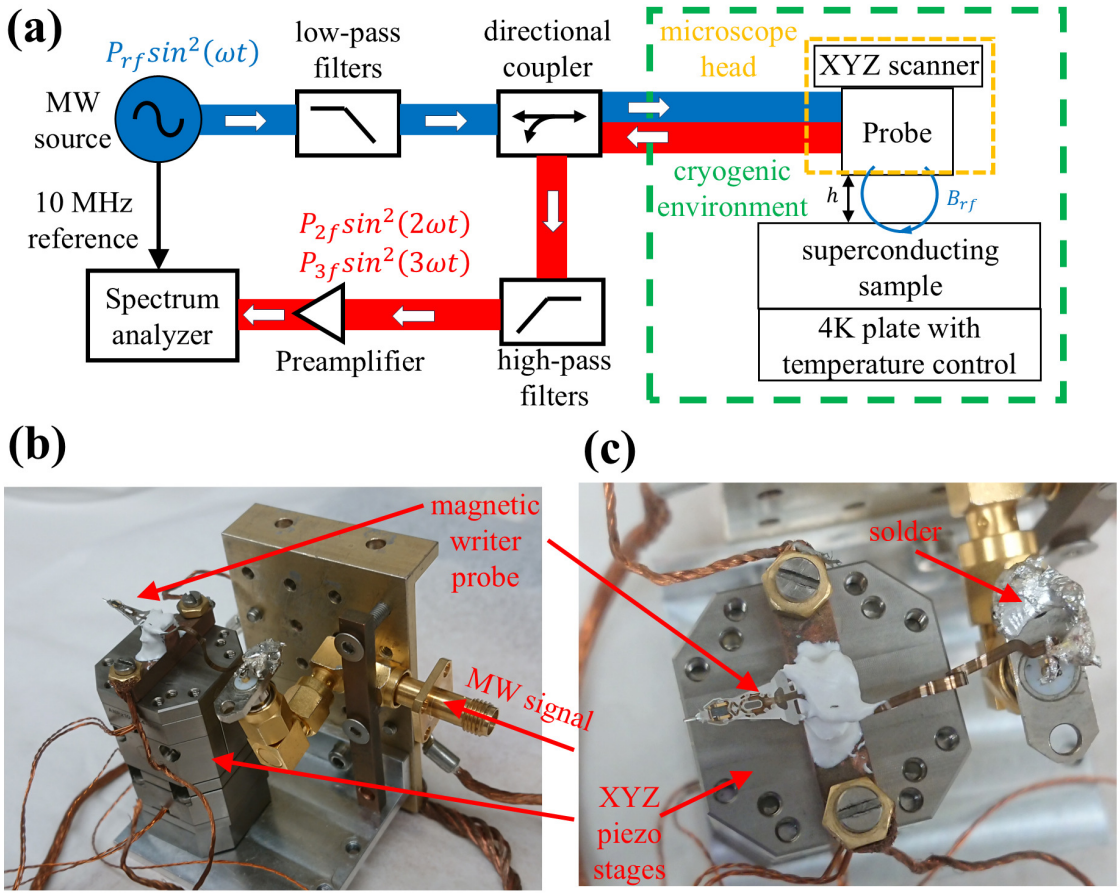

Figure 2.2: Near-field magnetic microwave microscope integrated into a dry cryostat. (a) Schematic of the microwave microscope, including both the room-temperature and cryogenic components. (b) Side view and (c) top view of the microscope head, highlighted by the yellow dashed box in (a).

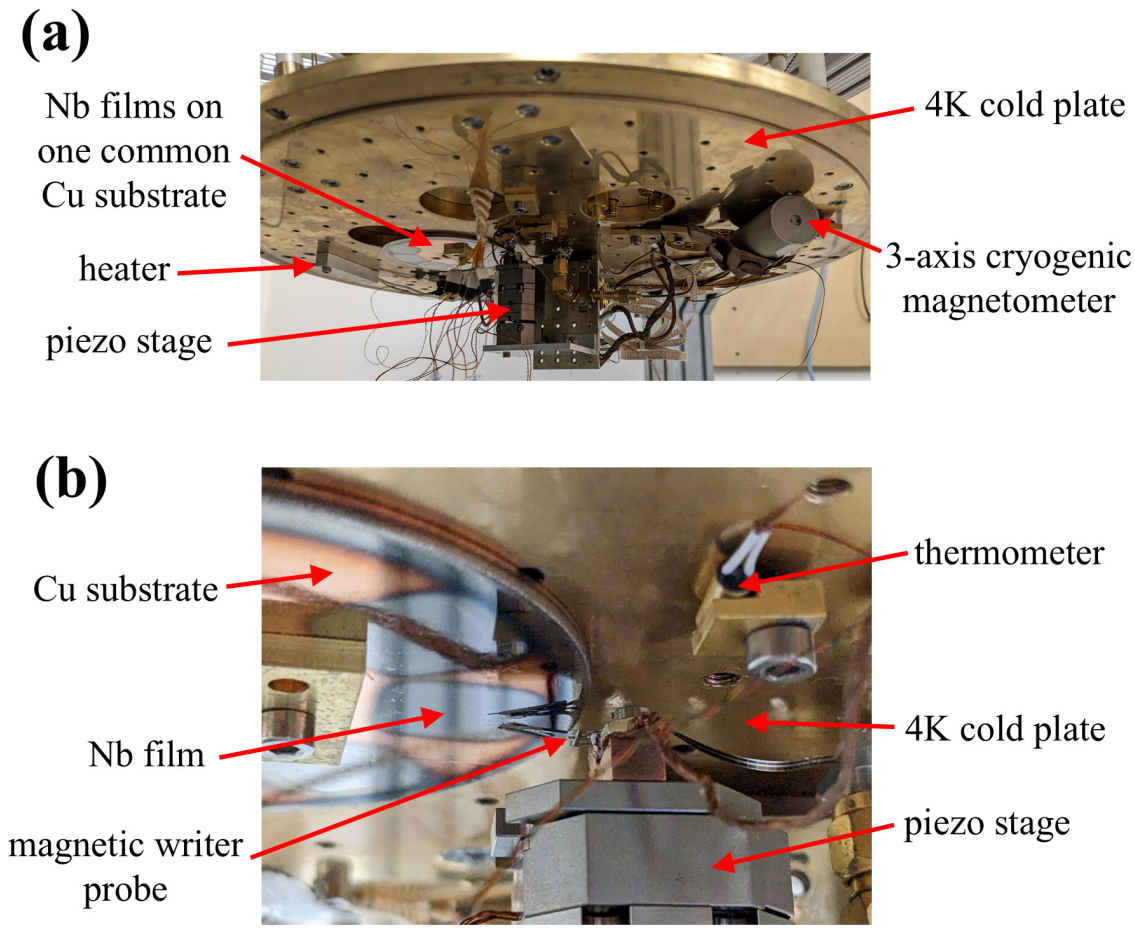

Figure 2.3: Photographs of a typical experimental setup. The superconducting samples are the Nb/Cu films studied in Chapter 5. (a) Side view of the experimental setup below the 4 K cold plate. (b) Close-up of (a), focusing on the microscope head and the superconducting samples.

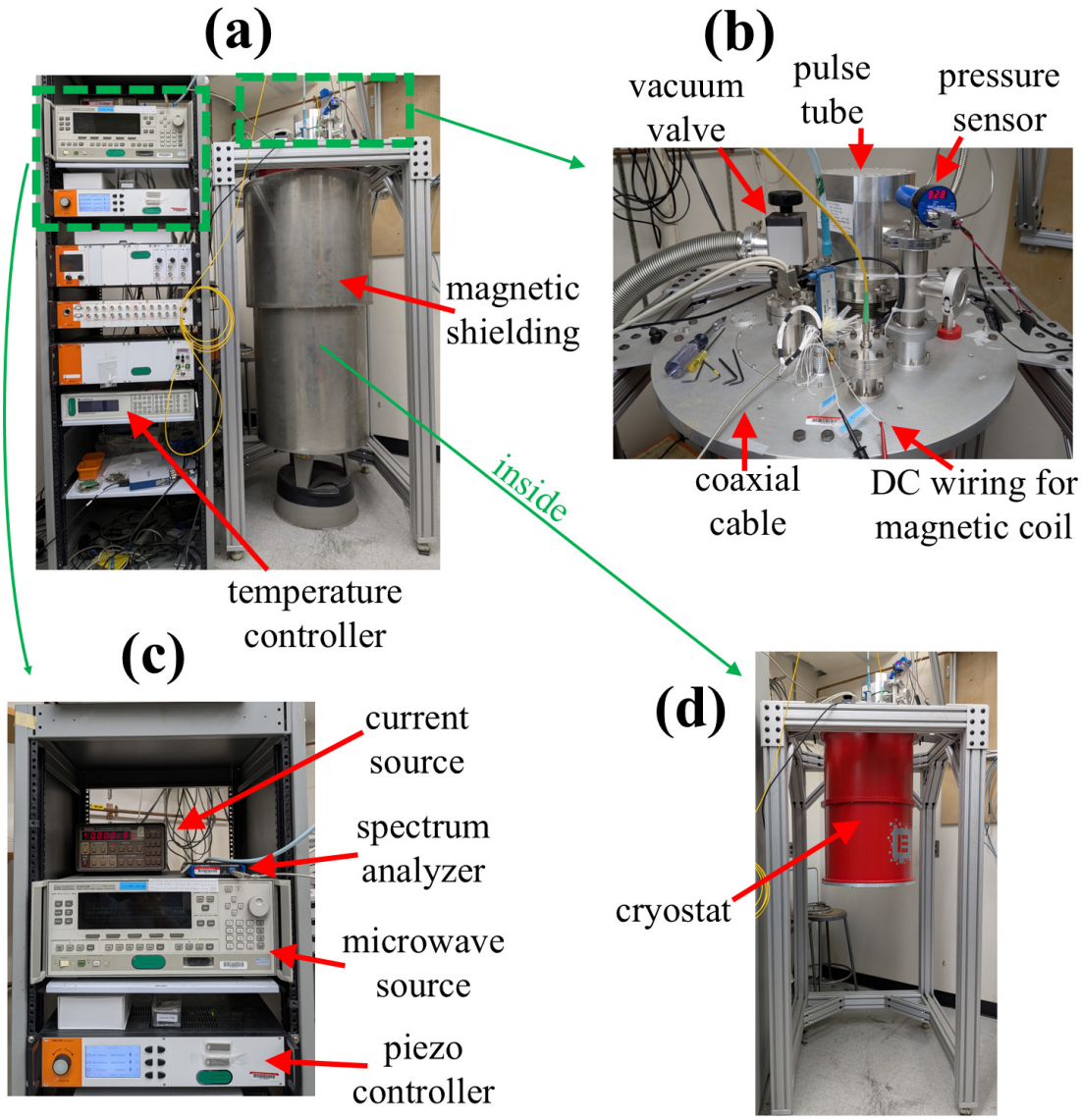

Figure 2.4: Photographs of the cryostat and relevant electronics. (a) Electronics setup (including the microwave source, piezo controller, temperature controller, etc.) and magnetic shielding of the cryostat. (b) Top view of the cryostat. (c) Close-up of selected electronics from (a). (d) The cryostat, surrounded by the magnetic shielding shown in (a).

Chapter 5. A Cernox thermometer is installed near the samples. A temperature controller (Lakeshore 340) is used to control the sample temperature.

2.4.2 Scanning System

In the experimental setup, a Seagate magnetic writer probe is attached to a cryogenic XYZ positioner (as shown in Fig. 2.2(b) and (c)) and employed in a scanning probe microscope fashion. The scanning system consists of 3 individual cryogenic piezo linear nanopositioners (2 of ANPx101/RES/LT and 1 ANPz101/RES/LT) controlled by a ANC350/3/RES Piezo Motion Controller. The nanopositioners and the controller are purchased from Attocube. Each positioner has a built-in resistive encoder which can be used to read-out the current position of the positioner with $200\,nm$ accuracy. Each positioner has a $5000\,\mu m$ travel range.

2.4.3 Probe-Sample Separation and Spatial Resolution

The probe is in contact with the sample during microwave measurements. However, the surfaces of the probe and the sample are not perfectly flat, resulting in a finite probe-sample separation h, which influences the spatial resolution of the microscope and the peak microwave magnetic field experienced by the sample B_{pk}. The height h is estimated to be less than 1 micron, and B_{pk} is estimated to fall within the range of tens of mT for a 0 dBm input microwave power [11]. The spatial resolution of the microscope ranges from sub-micron to micron scale, depending on the probe-sample separation, and the signal being analyzed.

The field of view of the probe is further discussed in Sec. 4.2.2, Sec. 6.3.3 and Sec. 7.6.2. In Sec. 4.2.2, the distribution of the screening current induced by an rf dipole at the surface of

bulk Nb obtained from numerical simulations is presented in Fig. 4.2 and Fig. 4.3(a), indicating a field of view on the order of hundreds of nanometers. In Sec. 6.3.3, the point-spread function for second-harmonic generation due to a trapped magnetic vortex obtained from numerical simulations is presented in Fig. 6.2, indicating a field of view on the order of hundreds of nanometers. In Sec. 7.6.2, the field of view for second-harmonic generation due to trapped DC magnetic vortices in experimental settings is estimated using a Monte Carlo approach, yielding a value of approximately $1.1\,\mu\mathrm{m}$.

2.4.4 Microwave Circuit and Measurement Procedure

A schematic of the rf circuit setup is presented in Fig. 2.2(a). The process begins with the production of a microwave signal $P_{\mathrm{rf}}\sin^2(\omega t)$ at frequency $f = \omega/2\pi$ by a microwave source (Keysight N5173B in the early stage of the research, later replaced by an HP 83620B). This signal is then directed to the magnetic writer probe inside the cryostat through a series connection of coaxial cables (filtering of the signals is discussed below). Notably, these include room-temperature coaxial cables outside the cryostat and cryogenic coaxial cables inside the cryostat. Thermal anchoring of the coaxial cables within the cryostat is ensured as they pass through the 70 K plate and the 4 K cold plate. The coaxial cable terminates with an SMA coaxial connector, which is directly soldered to the pads at the end of the magnetic writer probe transmission lines (see Figs. 2.2(b) and (c)). The probe then produces a local rf magnetic field $B_{\mathrm{rf}}\sin(\omega t)$ that acts on the sample surface. In response, the superconducting sample generates a time-dependent screening current on the surface in an effort to maintain the Meissner state. The magnetic field associated with this screening current is then coupled back to the same probe, creating a return propagating

signal on the transmission line structure. This response signal shares the same cryogenic coaxial cables with the input signal and is branched out by a directional coupler at room temperature.

The response signal consists of both linear and nonlinear components. The amplitude of the third-harmonic component $P_{3f}\sin^2(3\omega t)$ is projected out with a spectrum analyzer (Agilent E4407B in the early stage of the research, later replaced by an Aaronia RSA250X) at room temperature. A 10 MHz reference signal is generated by the microwave source and sent to the spectrum analyzer in order to synchronize the two instruments. This description applies specifically to third-harmonic response (P_{3f}) measurements, but the same procedure is followed for second-harmonic response (P_{2f}) measurements.

2.4.5 Filtering and Frequency Selection

To improve the signal-to-noise ratio, microwave filters are deployed in the following manner (as shown in Fig. 2.2(a)). First, low-pass filters are installed between the microwave source and the probe. These filters effectively block unwanted harmonic signals generated by the microwave source. Given that the response signal comprises both linear and nonlinear components, the next step involves the installation of high-pass filters between the probe and the spectrum analyzer. This placement prevents the fundamental input frequency signal (linear response [30]) from reaching the spectrum analyzer, thereby mitigating the generation of unwanted nonlinear signals. The frequency windows of the low-pass filters and the high-pass filters are 0 - 2.2 GHz and 2.9 - 8.7 GHz, respectively. The input frequency f is selected to fall within the range of 1.1 GHz to 2.2 GHz based on these frequency windows. This strategic choice ensures optimal filtering conditions and contributes to the overall improvement of the signal-to-noise ratio. This frequency range also

includes the operating frequency of superconducting radio-frequency Nb accelerator cavities [5].

2.4.6 Measurement Conditions and Instrument Settings

Measurements are performed with a variety of fixed input frequencies f between 1.1 GHz and 2.2 GHz, while temperature variations are explored within the range of 3.6 K to 20 K, and input power is adjusted across the spectrum from -40 dBm to +5 dBm. Since the response signal is precisely measured at a frequency of $3f$ in the spectrum analyzer, a narrow frequency span of 100 Hz, centered around $3f$, is sufficient. Both the resolution bandwidth (RBW) and the video bandwidth (VBW) of the spectrum analyzer are set at 3 Hz. With this configuration of the spectrum analyzer, the noise floor of the instrument is established at approximately -155 dBm, corresponding to about 2×10^5 photons/sec at 2 GHz.

Measurements of superconductor nonlinear response show tremendous dynamic range, often more than 20 dB [10, 11, 27–29]. The excellent instrumental nonlinear background of our measurements ($\sim$ -155 dBm) allows for very sensitive measurements of superconductor nonlinearity and its variation with temperature, driving rf power, location, and probe-sample separation. Note that measurements are recorded in dBm and later converted to linear power for further study.

2.4.7 Nonlinear Background Signal

The magnetic writer probe, serving as the probe in our microwave microscope, is composed of magnetic materials that exhibit nonlinearity, constituting the primary background signal (probe background) in the measurements of nonlinear response. The probe background is temperature-

independent, as confirmed both by P_{3f} measurements when the probe is not in contact with the superconducting sample and by P_{3f} measurements of a copper sample. The probe background can be determined by performing measurements above T_c of the superconducting sample. In this thesis, we study Nb samples, and T_c of Nb is around 9.3 K. In practice, probe background is determined by averaging the magnitude of $P_{3f}(T)$ between 9.5 K and 10 K.

Since the measured P_{3f} is the superposition of the probe background and the sample contribution, the probe background is subtracted from the total signal to isolate the sample response. However, the total measured signal may be weaker than the probe background if it is out of phase with the sample response. In the absence of phase information, we simply subtract the probe background from the total signal in a scalar manner. This naive background subtraction can result in negative P_{3f} values.

The phase information can be obtained by conducting measurements with a vector network analyzer [9, 28], which provides both amplitude and phase data, instead of a spectrum analyzer that only measures amplitude. However, due to its superior noise floor (approximately -155 dBm), we chose to use a spectrum analyzer for this work, rather than a vector network analyzer, which has a noise floor of around -130 dBm.

2.4.8 Magnetometer and Magnetic Shielding

To monitor the residual DC magnetic field near the sample at low temperatures, a cryogenic 3-axis magnetometer (Bartington Cryomag-100) is installed below the 4 K cold plate, as shown in Fig. 2.3(a). The magnetometer can operate at temperatures down to 2K and has a measurement range of 100 μT. It outputs three analog voltages (± 10 V), which are digitized using an analog-to-

digital converter (National Instruments NI 9239 BNC, 4-channel, ± 10 V) for computer readout.

During the measurements of the Nb/Cu films studied in Chapter 5, no magnetic shielding was used, and the residual DC magnetic field near the sample at low temperatures was approximately 35 μT. Later, magnetic shielding was implemented (as shown in Fig. 2.4(a)) for measurements of the antidot Nb film studied in Chapter 7. With magnetic shielding in place, the residual DC magnetic field near the sample at low temperatures was reduced to approximately 2.1 μT, as measured with the in-situ cryogenic 3-axis magnetometer.

2.4.9 Magnetic Coil for External Field Application

A magnetic coil is installed above the 4 K cold plate to generate an external DC magnetic field for studying trapped vortices in the antidot Nb film (Chapter 7). The sample is mounted below the 4 K cold plate and carefully aligned with the center of the magnetic coil to ensure uniform magnetic field application. The coil is driven by a Keithley 224 Programmable Current Source, capable of supplying stable DC currents from 0 to 100 mA. At its maximum current (100 mA), the coil generates a DC magnetic field of approximately 2.55 mT at the sample location. Since the magnetometer has a maximum measurement range of 100 μT, it is positioned sufficiently far from the magnetic coil so that the magnetic field at its location remains below this limit during the measurements described in Chapter 7.

After magnetic coil installation, the base temperature of the sample in the cryostat is approximately 3.8 K.

2.4.10 Final Remarks

Detailed operating procedures for the cryostat and the NFMMM are provided in Appendix A.

The NFMMM used in this thesis is based on a magnetic writer probe and has a spatial resolution ranging from sub-micron to micron scale. To further enhance spatial resolution, in addition to conducting measurements with this microscope, I have also worked on developing a next-generation microwave microscope based on Atomic Force Microscopy (AFM) architecture. Details on the early development of this new microscope are provided in Appendix B.

Chapter 3: Time-Dependent Ginzburg-Landau Theory: Equations and Simulation Framework

3.1 Introduction to the Time-Dependent Ginzburg-Landau Theory

Different theoretical frameworks describe and study superconductivity at various levels [1]. The London equations [71] and the two-fluid model [72] capture essential macroscopic properties of superconductors, such as the Meissner effect, and relate the electric current density inside a superconductor to the magnetic vector potential. The Bardeen-Cooper-Schrieffer (BCS) theory [2], developed in 1957, provides a microscopic understanding of superconductivity by describing the formation of Cooper pairs through electron-phonon interactions.

3.1.1 Phenomenological Ginzburg-Landau Theory

The Ginzburg-Landau (GL) theory (see Chapter 4 in Ref. [3]), in contrast, is a phenomenological approach that describes the superconducting phase transition from a thermodynamic perspective. It is a mean-field theory that is built upon a general approach to the theory of second-order phase transitions which Landau developed in the 1930s. In the GL theory, the superconducting phase is characterized by a complex order parameter, $\psi(x, y, z) = |\psi(x, y, z)|e^{i\theta(x,y,z)}$, which is zero in the normal state above the critical temperature T_c and becomes nonzero below T_c. Since ψ is a spatially

varying function, namely $\psi = \psi(x, y, z)$, it naturally accounts for inhomogeneous superconducting structures, including vortices [73]. Moreover, because ψ describes superconductivity as a macroscopic quantum state, the model inherently predicts magnetic flux quantization in vortices. Roughly speaking, $|\psi(x, y, z)|$ can be interpreted as the local strength of superconductivity at (x, y, z). In particular, $|\psi(x, y, z)|$ decreases significantly at the core of a vortex, where superconductivity is strongly suppressed.

3.1.2 Time-Dependent Ginzburg-Landau Theory

By extending the GL theory to include time dependence, namely $\psi = \psi(x, y, z, t)$, one obtains the time-dependent Ginzburg-Landau (TDGL) theory, which provides a dynamical description of superconducting phenomena. The fundamental equations of TDGL, which govern the temporal evolution of ψ and its coupling to electromagnetic fields, are discussed in Sec. 3.2.

TDGL is a widely used framework for studying vortex dynamics in superconductors [12, 74–83], as it naturally accounts for both spatial and temporal variations of the superconducting order parameter, $\psi = \psi(x, y, z, t)$. This capability makes TDGL particularly well-suited for investigating vortex motion, interactions, and pinning effects in type-II superconductors. Furthermore, the proximity effect is incorporated naturally in TDGL simulations. Due to these advantages, this thesis employs numerical simulations based on TDGL to explore vortex dynamics in superconductors through a series of toy models.

3.2 Fundamental Equations of TDGL

3.2.1 Ginzburg-Landau Theory

The basic postulate of the GL theory is that if ψ is small and varies slowly in space, the Ginzburg-Landau free energy F_{GL} of a superconductor can be expanded in a series as [1]

$$F_{GL} = \frac{-1}{2m_*} \left|(-i\hbar\nabla - e_* A)\,\psi\right|^2 + \alpha\left|\psi\right|^2 + \frac{\beta}{2}\left|\psi\right|^4 + \frac{1}{2\mu_0}\left|\nabla \times A - B_{\text{ext}}\right|^2. \tag{3.1}$$

Here $e_* = 2e$ is the charge of the Cooper pair, $m_* = 2m_e$ is the mass of the Cooper pair, ψ is the order parameter, A is the total vector potential (arising from both external and self-generated sources), B_{ext} is the external magnetic field, and both α and β are material-specific phenomenological parameters.

The two parameters α and β can be related to the penetration depth λ and the thermodynamic critical field B_{c} by

$$\lambda = \sqrt{\frac{m_*\beta}{\mu_0 e_*^2\left|\alpha\right|}} \tag{3.2}$$

and

$$B_{\text{c}} = \frac{\sqrt{\mu_0}\left|\alpha\right|}{\sqrt{\beta}}. \tag{3.3}$$

The GL theory is valid only near T_{c}. In this regime ($T \lesssim T_{\text{c}}$), the coefficient β remains a positive constant, while α follows the temperature dependence

$$\alpha(T) = \alpha_0\left(1 - \frac{T}{T_{\text{c}}}\right), \tag{3.4}$$

where α_0 is a negative constant.

In the absence of fields and gradients, we have

$$F_{GL} = \alpha |\psi|^2 + \frac{\beta}{2} |\psi|^4 . \tag{3.5}$$

The minimum of this free energy occurs when

$$|\psi|^2 = |\psi_\infty|^2 = -\frac{\alpha}{\beta}. \tag{3.6}$$

The notation ψ_∞ is conventionally used because ψ approaches this value infinitely deep in the interior of the superconductor, where fields and currents go to zero and the equilibrium value of ψ is achieved. The normalized order parameter is typically defined as ψ/ψ_∞, with its magnitude ranging from 0 to 1.

3.2.2 Time Evolution and the First TDGL Equation

The time evolution of the order parameter ψ can be introduced by considering its relaxation dynamics following a small perturbation from equilibrium. In the TDGL framework, these relaxation dynamics are assumed to be governed by the following equation [1, 84]:

$$-\gamma \left(\frac{\partial}{\partial t} + i \frac{e_*}{\hbar} \Phi \right) \psi = \frac{\delta F_{GL}}{\delta \psi^*}. \tag{3.7}$$

Here Φ is the electric potential, and $\gamma = \frac{\pi\hbar|\alpha|}{8k_B(T_c - T)}$ plays the role of a friction coefficient. This variational problem leads to the dynamics of ψ as (the first TDGL equation)

$$\gamma\left(\frac{\partial}{\partial t} + i\frac{e_*}{\hbar}\Phi\right)\psi = \frac{-1}{2m_*}\left(-i\hbar\nabla - e_*A\right)^2\psi - \alpha\psi - \beta\left|\psi\right|^2\psi. \tag{3.8}$$

3.2.3 Derivation of the Second TDGL Equation

Now consider the Ampère's law

$$\nabla \times B = \mu_0 J + \mu_0\epsilon_0\frac{\partial E}{\partial t}. \tag{3.9}$$

Assume the displacement current term ($\mu_0\epsilon_0\frac{\partial E}{\partial t}$) is negligible, and we have

$$\nabla \times B = \mu_0 J. \tag{3.10}$$

Apply Eq. 3.10 to the current J_{SC} and the magnetic field B_{SC} generated by the superconductor, and we get

$$\nabla \times B_{\mathrm{SC}} = \mu_0 J_{\mathrm{SC}}. \tag{3.11}$$

The total magnetic field B is the combination of the external magnetic field B_{ext} and the magnetic field generated by the superconductor B_{SC}, and hence we have

$$B_{\mathrm{SC}} = B - B_{\mathrm{ext}} = \nabla \times A - B_{\mathrm{ext}}. \tag{3.12}$$

The current generated by the superconductor J_{SC} is the combination of the supercurrent J_{s} and the normal current J_{n}

$$J_{\mathrm{SC}} = J_{\mathrm{s}} + J_{\mathrm{n}}. \tag{3.13}$$

Combine Eqs. 3.11, 3.12, and 3.13, and we obtain

$$\nabla \times (\nabla \times A - B_{\mathrm{ext}}) = \mu_0 \left(J_{\mathrm{s}} + J_{\mathrm{n}}\right). \tag{3.14}$$

The supercurrent J_{s} and the normal current J_{n} are given by

$$J_{\mathrm{s}} = \frac{-i\hbar e_*}{2m_*} \left(\psi^* \nabla\psi - \psi \nabla\psi^*\right) - \frac{e_*^2}{m_*} |\psi|^2 A \tag{3.15}$$

and

$$J_{\mathrm{n}} = \sigma E = \sigma \left(-\nabla\Phi - \frac{\partial A}{\partial t}\right). \tag{3.16}$$

Here σ is the electric conductivity of the normal state. Combine Eqs. 3.14, 3.15, and 3.16, and the Ampere's law now reads

$$\nabla \times (\nabla \times A - B_{\mathrm{ext}}) = \mu_0 \left[\frac{-i\hbar e_*}{2m_*} \left(\psi^* \nabla\psi - \psi \nabla\psi^*\right) - \frac{e_*^2}{m_*} |\psi|^2 A + \sigma \left(-\nabla\Phi - \frac{\partial A}{\partial t}\right)\right]. \tag{3.17}$$

Rearrange the time derivative of A to the left-hand side and we get the dynamics of A (the second TDGL equation)

$$\sigma \left(\nabla\Phi + \frac{\partial A}{\partial t}\right) = \frac{-i\hbar e_*}{2m_*} \left(\psi^* \nabla\psi - \psi \nabla\psi^*\right) - \frac{e_*^2}{m_*} |\psi|^2 A - \frac{1}{\mu_0} \nabla \times (\nabla \times A - B_{\mathrm{ext}}). \tag{3.18}$$

3.2.4 Final Form of the TDGL Equations

The scenarios of interest involve stimulating the superconductor with an oscillating magnetic field; therefore, no external current is present inside the superconductor. In other words,

$$\nabla \times B_{\text{ext}} = \mu_0 J_{\text{ext}} = 0 \tag{3.19}$$

in the superconducting domain. In addition, we choose the gauge such that the scalar potential is zero

$$\Phi = 0. \tag{3.20}$$

Combine Eqs. 3.8, 3.18, 3.19, and 3.20, the two TDGL equations in the superconducting domain become

$$\gamma \frac{\partial \psi}{\partial t} = \frac{-1}{2m_*} \left(-i\hbar\nabla - e_* A\right)^2 \psi - \alpha\psi - \beta \left|\psi\right|^2 \psi \tag{3.21}$$

and

$$\sigma \frac{\partial A}{\partial t} = \frac{-i\hbar e_*}{2m_*} \left(\psi^* \nabla\psi - \psi\nabla\psi^*\right) - \frac{e_*^2}{m_*} \left|\psi\right|^2 A - \frac{1}{\mu_0} \nabla \times \nabla \times A. \tag{3.22}$$

The two TDGL equations (Eqs. 3.21 and 3.22) form a set of coupled nonlinear partial differential equations that govern the dynamics of the order parameter $\psi(x, y, z, t)$ and the electromagnetic field $A(x, y, z, t)$ inside the superconductor. Notably, Maxwell's equations are inherently included, as Eq. 3.22 originates from Ampère's law.

In numerical simulations, we solve for the full dynamics of (ψ, A), including both its spatial variation and time evolution, using Eqs. 3.21 and 3.22. This allows us to track how the order parameter and electromagnetic field evolve in space and time. The computed results of (ψ, A) are then used to compute the nonlinear response. The details of the simulation setup are provided in Sec. 3.4.

In practice, the dimensionless form of the two TDGL equations (Eqs. 3.21 and 3.22) is used in numerical simulations. Different choices of dimensionless scaling, corresponding to different changes of variables, lead to distinct forms of the dimensionless TDGL equations. This thesis employs two different dimensionless formulations for simulations, both of which are presented in Appendix C.

The TDGL simulations in this thesis are performed using COMSOL Multiphysics. The implementation details of these simulations in COMSOL are provided in Appendix D.

3.3 Useful Equations for TDGL Simulations and Analysis

In this section, we provide some useful equations for TDGL simulations and analysis.

The coherence length ξ characterizes the length scale over which the order parameter ψ varies spatially. In the GL theory, it is given by

$$\xi = \frac{\hbar}{\sqrt{2m_* |\alpha|}}. \tag{3.23}$$

The penetration depth λ characterizes the length scale over which the magnetic field B varies

spatially. Their ratio, known as the Ginzburg-Landau parameter, is defined as

$$\kappa = \frac{\lambda}{\xi}. \tag{3.24}$$

A superconductor is type-I if $\kappa < \frac{1}{\sqrt{2}}$ and is type-II if $\kappa > \frac{1}{\sqrt{2}}$.

The diffusion coefficient D can be related to γ by

$$\gamma = \frac{\hbar^2}{2m_* D}. \tag{3.25}$$

The Ginzburg-Landau order parameter relaxation time τ_{GL} is given by

$$\tau_{GL} = \frac{\xi^2}{D} = \frac{\pi\hbar}{8k_B\left(T_\mathrm{c} - T\right)} = \left(3 \cdot 10^{-12}\ \mathrm{s}\right)\left(\frac{\mathrm{K}}{T_\mathrm{c} - T}\right), \tag{3.26}$$

Note that the dynamics of a superconductor driven by an rf field at a few GHz ($\frac{1}{1\ \mathrm{GHz}} = 10^{-9}$ s) typically falls within the adiabatic limit, defined by $\frac{1}{f} \gg \tau_{GL}$, where f is the frequency of the rf field. This condition holds unless the temperature is extremely close to T_c, specifically when $T_\mathrm{c} - T < 10^{-2}$ K.

For stimulations in the THz regime, the period of oscillation becomes comparable to the relaxation timescale of the Ginzburg-Landau order parameter. As a result, the dynamics of a superconductor driven by a THz field are no longer adiabatic.

The temperature dependence of some key quantities is discussed below. Note that the GL theory is valid only for $T \approx T_\mathrm{c}$, and therefore, these temperature dependencies hold only in this

regime.

$$\xi(T) \approx \frac{\xi(T=0)}{\sqrt{1-\frac{T}{T_c}}}. \tag{3.27}$$

$$\lambda(T) \approx \frac{\lambda(T=0)}{\sqrt{1-\left(\frac{T}{T_c}\right)^4}}. \tag{3.28}$$

$$\kappa(T) \approx \kappa(T=0). \tag{3.29}$$

$$\psi_\infty(T) \approx \sqrt{1-\left(\frac{T}{T_c}\right)^4}\,\psi_\infty(T=0). \tag{3.30}$$

$$B_c(T) \approx \left[1-\left(\frac{T}{T_c}\right)^2\right] B_c(T=0). \tag{3.31}$$

3.4 Simulation Setup

3.4.1 Modeling the Localized rf Magnetic Field: rf Magnetic Dipole Model

In our microwave microscope measurements, a superconducting sample is stimulated by a localized rf magnetic field generated by the microscope probe (a magnetic writer head), as described in Sec. 2.3 and Sec. 2.4. To better understand the superconductor dynamics beneath the probe, we replicate this scenario in TDGL simulations using toy models.

The rf magnetic field produced by the probe is non-uniform and contains both longitudinal and perpendicular components [70]. Its exact configuration is complex and depends on the detailed design of the magnetic writer, which is not available in the open literature and therefore is beyond the scope of this study. The objective of the TDGL simulations in this thesis is to qualitatively, rather than quantitatively, understand the superconducting dynamics beneath the probe and the resulting nonlinear responses collected by the probe, which arise from time-dependent screening

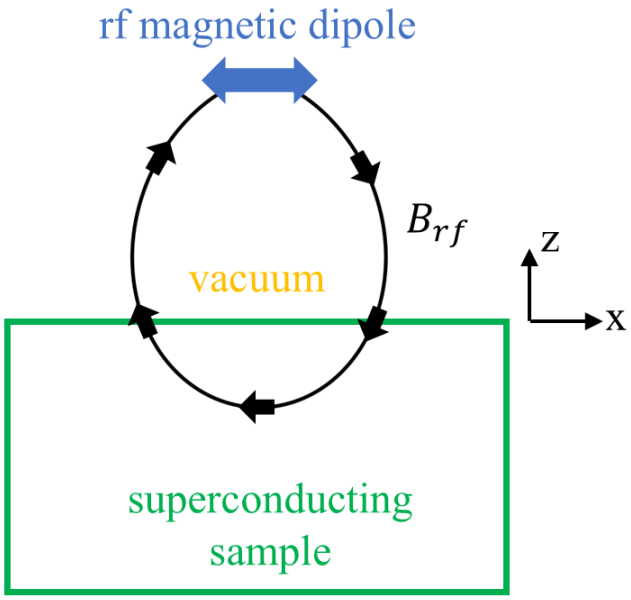

Figure 3.1: Schematic of an rf magnetic dipole positioned above a superconducting sample. The blue double arrow represents the rf magnetic dipole. The black curve (B_{rf}) represents the rf magnetic field generated by the dipole.

currents and magnetic fields generated by the sample. Accurately reproducing the detailed field configuration of the microscope probe is not the goal. Instead, we focus on modeling a localized magnetic field that captures the essential characteristic of the actual probe field: the presence of both longitudinal and perpendicular components. To this end, we approximate the probe field using the magnetic field of a point dipole oriented parallel to the superconducting surface, which provides a reasonable and physically motivated toy model for our simulations.

Figure 3.1 presents a schematic of an rf magnetic dipole positioned above a superconducting sample (the rf magnetic dipole model). The blue double arrow represents the rf dipole. The black curve (B_{rf}) represents the rf magnetic field generated by the dipole. Since the superconducting sample experiences both longitudinal and perpendicular components of the rf magnetic field, this dipole model serves as a reasonable approximation of the applied magnetic field distribution

beneath the magnetic writer head. For simplicity, the term "rf dipole" will hereafter refer to the rf magnetic point dipole.

It is worth noting that the detailed field configuration of the microscope probe, as well as losses in the measurement circuit due to imperfections, are not included in the rf dipole model. This is because the primary objective of the TDGL simulations is to capture the qualitative behavior—rather than quantitative accuracy—of the nonlinear responses collected by the microscope probe.

It is important to note that the rf dipole serves two purposes: (1) it illuminates the sample with a sinusoidal magnetic field at frequency f, and (2) it picks up a complex time-domain signal from the superconductor, which includes frequency responses at f, $2f$, $3f$, etc.

Experimentally, the time dependence of the superconducting order parameter is not measured directly. Instead, the probe (modeled as an rf dipole in simulations) detects the magnetic fields generated by the sample, which arise from time-dependent screening currents within the superconductor.

3.4.2 Simulation Domain and External Field

Figure 3.2 presents a schematic of the simulation setup. The simulation consists of two domains (both are cylindrical): a vacuum domain occupying the $z > 0$ region and a smooth, flat superconducting sample occupying the $z < 0$ region.

The probe is approximated as a pointlike magnetic dipole located at $(x_{\mathrm{dp}}, y_{\mathrm{dp}}, h_{\mathrm{dp}}) = (0, 0, 400\,\mathrm{nm})$. The dipole is oriented along the x-direction and has a sinusoidal time-dependent

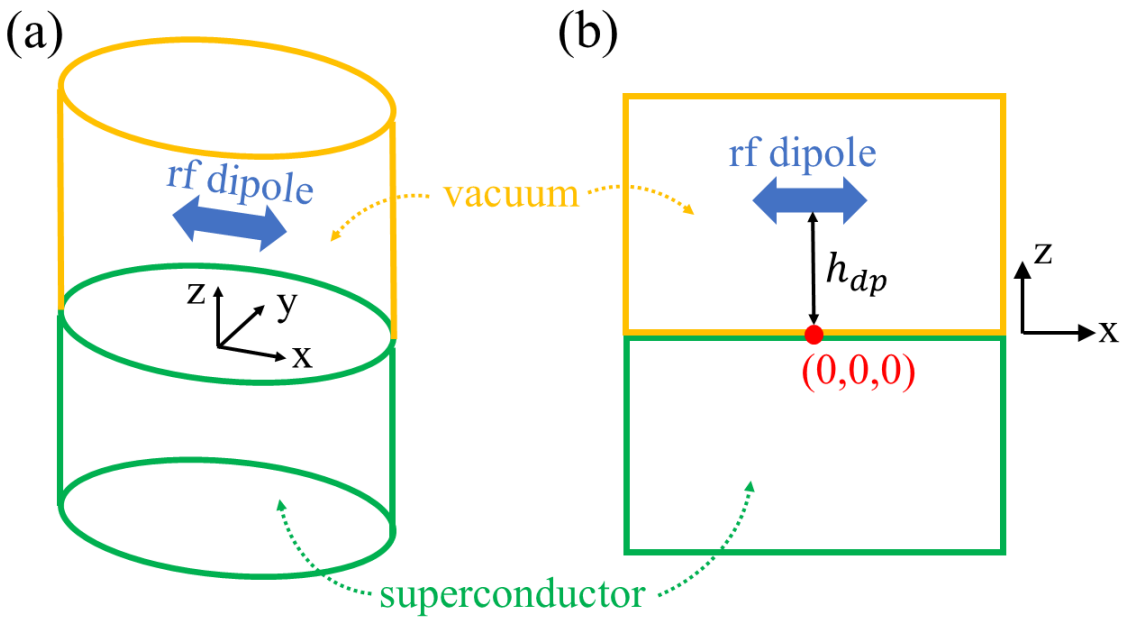

Figure 3.2: Schematic of the simulation setup. (a) Three-dimensional view. (b) Side view illustrating the spatial arrangement of the rf dipole (blue double arrow) positioned above a superconducting sample (green cylinder), with a vacuum region (yellow cylinder) above. The rf dipole is modeled as a point source located at $(x_{\mathrm{dp}}, y_{\mathrm{dp}}, h_{\mathrm{dp}}) = (0, 0, h_{\mathrm{dp}})$, with its magnetic moment oscillating in the x-direction. The red point at $(0, 0, 0)$ marks the location in the sample experiencing the strongest rf magnetic field.

magnetic moment $M(t)$ given by

$$M(t) = (M_{\mathrm{dp}} \sin(\omega t), 0, 0), \tag{3.32}$$

where the frequency is $f = \omega/2\pi = 1.7$ GHz. The magnetic field B_{dp} and the vector potential A_{dp} produced by the point dipole (the external field in the simulations) are

$$B_{\mathrm{dp}} = \frac{\mu_0}{4\pi} \frac{1}{r^3} \left[3(M \cdot \hat{r})\hat{r} - M\right] \tag{3.33}$$

and

$$A_{\mathrm{dp}} = \frac{\mu_0}{4\pi} \frac{M \times r}{r^3}, \tag{3.34}$$

where $r = (x - x_{\mathrm{dp}}, y - y_{\mathrm{dp}}, z - h_{\mathrm{dp}})$.

To quantify the strength of the rf magnetic field, we define B_{pk} as the peak rf magnetic field amplitude experienced by the superconductor. The strongest field occurs at $(x, y, z) = (0, 0, 0)$ within the sample; therefore, B_{pk} represents the rf field amplitude at this location.

Since the rf field is highly localized, non-trivial sample dynamics, such as vortex nucleation, are expected to occur only in the region directly beneath the rf dipole (i.e., near $(x, y, z) = (0, 0, 0)$). In contrast, regions far from the rf dipole remain in the vortex-free Meissner state.

3.4.3 Boundary Conditions and Numerical Implementation

Figure 3.3 presents a schematic of the "multi-domain 3D simulations", illustrating the equations solved in each domain and the imposed boundary conditions. The model is inhomogeneous in that it consists of two distinct domains: a vacuum domain, which hosts the rf dipole as a source

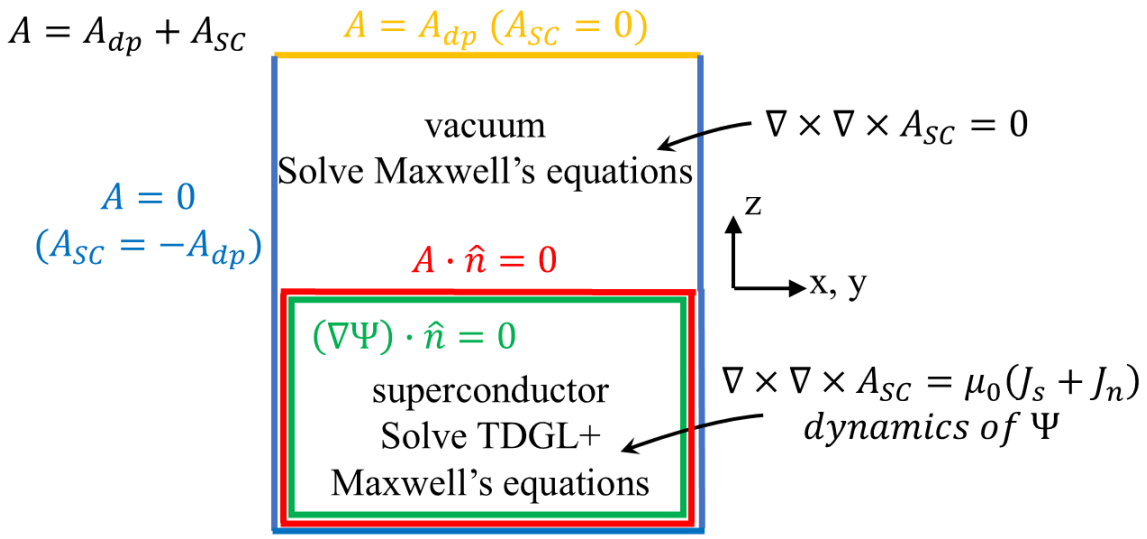

Figure 3.3: Schematic of the multi-domain 3D simulations, illustrating the equations solved in each region and the imposed boundary conditions. The total vector potential is given by $A = A_{\mathrm{dp}} + A_{\mathrm{SC}}$. In the vacuum domain (top region), Maxwell's equations are solved, with A_{SC} satisfying $\nabla \times \nabla \times A_{\mathrm{SC}} = 0$. The superconducting domain (bottom region) hosts the coupled TDGL and Maxwell's equations, where A_{SC} obeys $\nabla \times \nabla \times A_{\mathrm{SC}} = \mu_0(J_{\mathrm{s}} + J_{\mathrm{n}})$. Boundary conditions (indicated by the colorful lines) are applied to all surfaces of the two domains, including the vacuum-superconductor interface.

of high-frequency magnetic fields (as illustrated in Fig. 3.2), and a superconducting domain.

Note that the total vector potential A consists of two contributions: the dipole vector potential A_{dp} and the superconducting response A_{SC}. That is,

$$A = A_{\mathrm{dp}} + A_{\mathrm{SC}}. \tag{3.35}$$

Since A_{dp} is known (see Eqs. 3.34), the quantity that must be solved for is A_{SC} rather than A.

In the vacuum domain (top region in Fig. 3.3), Maxwell's equations are solved, with A_{SC} satisfying $\nabla \times \nabla \times A_{\mathrm{SC}} = 0$. In the superconducting domain (bottom region in Fig. 3.3), the coupled TDGL and Maxwell's equations are solved, where A_{SC} obeys $\nabla \times \nabla \times A_{\mathrm{SC}} = \mu_0(J_{\mathrm{s}} + J_{\mathrm{n}})$. The simulation domain is finite, and no periodic boundary conditions are imposed. However, since primary non-trivial sample dynamics occur near the origin, finite-size effects are mitigated by selecting a sufficiently large simulation domain and applying appropriate boundary conditions. The boundary conditions (indicated by the colorful lines in Fig. 3.3) are applied to all surfaces of the two domains, including the vacuum-superconductor interface.

In regions far from the rf dipole, the total magnetic field is very weak and is approximated as zero, as indicated by the blue lines in Fig. 3.3. The presence of the rf dipole is incorporated through an appropriate boundary condition. Specifically, we impose $A = A_{\mathrm{dp}}$ at the top surface of the vacuum domain, as indicated by the yellow line in Fig. 3.3.

Any current passing through the boundary between a superconductor and a vacuum is unphysical. Therefore, the boundary conditions must be enforced along the entire enclosing boundary $\partial\Omega$ of the superconducting simulation domain, including the sides and bottom surfaces.

Specifically, we expect [12]

$$J \cdot \hat{n} = 0 \quad \text{on} \quad \partial\Omega. \tag{3.36}$$

Here $\hat{n}$ is the unit vector normal to the boundary. Recall that the supercurrent J_{s} is (see Eq. 3.15)

$$J_{\mathrm{s}} = \frac{-i\hbar e_*}{2m_*} \left(\psi^* \nabla\psi - \psi \nabla\psi^*\right) - \frac{e_*^2}{m_*} |\psi|^2 A. \tag{3.37}$$

The boundary condition in Eq. 3.36 should apply to J_{s} and remain valid even when $A = 0$, which leads to

$$\nabla\psi \cdot \hat{n} = 0 \quad \text{on} \quad \partial\Omega. \tag{3.38}$$

Combine Eqs. 3.36, 3.15, and 3.38 and we obtain

$$A \cdot \hat{n} = 0 \quad \text{on} \quad \partial\Omega. \tag{3.39}$$

Equations 3.38 (as indicated by the green rectangle in Fig. 3.3) and 3.39 (as indicated by the red rectangle in Fig. 3.3) are applied as the boundary conditions along the entire enclosing boundary $\partial\Omega$ of the superconducting simulation domain.

3.4.4 Comparison with Other TDGL Approaches

Many TDGL treatments assume a two-dimensional sample with fields that are uniform along the third dimension. This oversimplification introduces "artificial features that extend uniformly" in the third dimension, leading to infinitely long vortices in the superconductor. In contrast, our approach employs "multi-domain 3D simulations", which do not rely on such unrealistic

assumptions. However, these fully three-dimensional TDGL simulations are computationally demanding in terms of both memory usage and processing time.

In our case, since the superconductor is subjected to a time-dependent and inhomogeneous rf magnetic field, the full TDGL equations must be solved. Unlike many simplified models, we do not assume or impose any spatial symmetries. Instead, we explicitly solve Maxwell's equations both in free space above the superconductor and within the superconducting region [12].

3.5 Workflow of TDGL Simulations

3.5.1 Overview of the Simulation Process

This section discusses the typical workflow of the TDGL simulations, summarized in Fig. 3.4.

In the simulations, TDGL is used to calculate the time evolution of the order parameter ψ and the vector potential A as the superconducting sample is stimulated by the time-dependent rf field produced by the horizontal point dipole above it. The process begins by solving the TDGL equations with initial conditions (I.C.) and boundary conditions (B.C.), where the boundary conditions are detailed in Sec. 3.4. For the initial conditions, we apply the rf magnetic field starting at $t = 0$, and set $\psi = \psi_\infty$ throughout the entire superconducting domain.

Note that for the electromagnetic field degree of freedom, instead of solving for the total vector potential A, we solve for the superconducting response A_{SC}, since the dipole contribution A_{dp} is known, as discussed in Sec. 3.4.

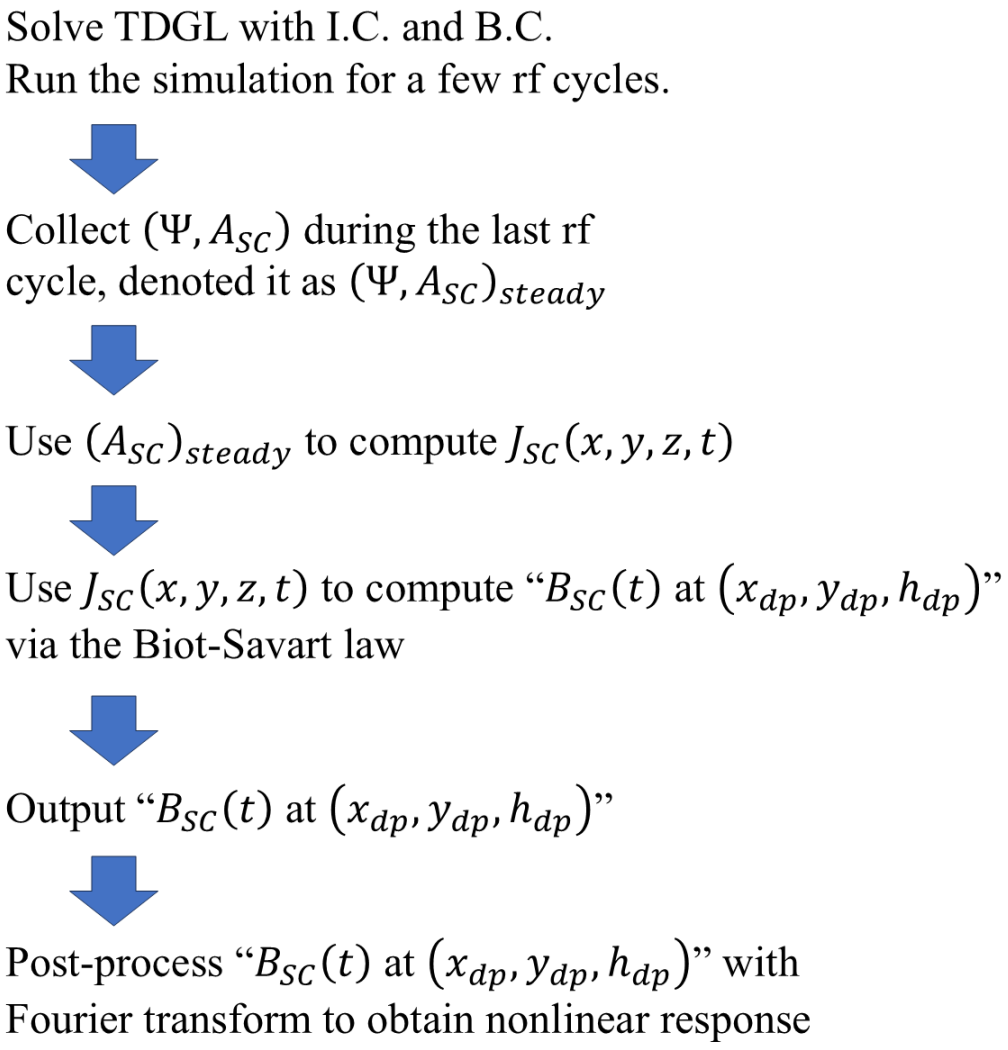

Figure 3.4: Schematic workflow of the TDGL simulations. The process begins by solving the TDGL equations with initial conditions (I.C.) and boundary conditions (B.C.) over multiple rf cycles until steady state is achieved, and ends with extracting the nonlinear response with Fourier transform.

3.5.2 Time Evolution and Steady-State Solution

During the time evolution, the superconductor dynamics initially undergoes a transient state before converging to a steady state. To ensure that the system reaches this steady state, the simulation is run for several rf cycles. The steady-state solutions, $(\psi, A_{\mathrm{SC}})_{\mathrm{steady}}$, are then collected during the final rf cycle.

The rate at which the superconductor dynamics converges to its steady state depends on the type of dynamics under consideration. For the nucleation of rf vortex semi-loops, as discussed in Chapter 4, the dynamics converges relatively quickly. In this case, the simulation is run for two rf cycles, and (ψ, A_{SC}) is collected during the second rf cycle and treated as $(\psi, A_{\mathrm{SC}})_{\mathrm{steady}}$. Conversely, for the dynamics of trapped vortices, as discussed in Chapter 6, convergence is slower. Here, the simulation is run for five rf cycles, and (ψ, A_{SC}) is collected during the fifth rf cycle and treated as $(\psi, A_{\mathrm{SC}})_{\mathrm{steady}}$.

3.5.3 Extracting the Superconductor Response

In our microwave microscope measurements, the response of the superconducting sample is collected using the microscope probe, which is modeled as an rf dipole in TDGL simulations. To compare the simulation results with experimental data, we evaluate the superconductor response at the location of the rf dipole $(x_{\mathrm{dp}}, y_{\mathrm{dp}}, h_{\mathrm{dp}})$, and denote its x-component as $B_{\mathrm{SC}}^{\mathrm{dp\ location}}$. Since the microscope probe is modeled as an rf dipole oriented along the x-direction, we focus on the x-component of the superconductor response in our analysis. In experiments, it is assumed that the time-varying magnetic field at the probe, which corresponds to $B_{\mathrm{SC}}^{\mathrm{dp\ location}}$ in TDGL simulations, induces a voltage wave that propagates to a spectrum analyzer at room temperature. The procedure

for obtaining $B_{\mathrm{SC}}^{\mathrm{dp\ location}}$ is discussed below.

The superconducting current density $J_{\mathrm{SC}}(x, y, z, t)$ is computed using

$$J_{\mathrm{SC}} = \frac{1}{\mu_0} \nabla \times B_{\mathrm{SC}} = \frac{1}{\mu_0} \nabla \times \nabla \times A_{\mathrm{SC}}, \tag{3.40}$$

where the steady-state vector potential, $A_{\mathrm{SC}_{\mathrm{steady}}}(x, y, z, t)$, is used in place of $A_{\mathrm{SC}}(x, y, z, t)$. The next step is to integrate $J_{\mathrm{SC}}(x, y, z, t)$ over the entire superconducting domain to obtain $B_{\mathrm{SC}}^{\mathrm{dp\ location}}(t)$ via the Biot-Savart law.

The Biot-Savart law is used to compute the magnetic field contribution at the location of the rf dipole based on the superconducting current density $J_{\mathrm{SC}}(x, y, z, t)$. The field at a given point $\mathbf{r}$ is obtained by integrating over the entire superconducting domain:

$$B_{\mathrm{SC}}^{\mathrm{dp\ location}}(t) = \frac{\mu_0}{4\pi} \int_{\Omega} \frac{J_{\mathrm{SC}}(\mathbf{r}', t) \times (\mathbf{r} - \mathbf{r}')}{|\mathbf{r} - \mathbf{r}'|^3} dV', \tag{3.41}$$

where $\mathbf{r}$ is the observation point (i.e., the location of the rf dipole), $\mathbf{r}'$ represents points within the superconducting volume Ω, and $J_{\mathrm{SC}}(\mathbf{r}', t)$ is the superconducting current density at $\mathbf{r}'$. The integral is evaluated over the entire superconducting region.

All these computations are performed within COMSOL Multiphysics. We then output $B_{\mathrm{SC}}^{\mathrm{dp\ location}}(t)$, the superconductor response at the location of the rf dipole based on the dynamics observed during the last rf cycle. The nonlinear response of the superconductor is then analyzed by post-processing $B_{\mathrm{SC}}^{\mathrm{dp\ location}}(t)$ via Fourier transform.

3.5.4 Fourier Analysis and Nonlinear Response

The Fourier expansion of $B_{\mathrm{SC}}^{\mathrm{dp\ location}}(t)$ can be expressed as

$$B_{\mathrm{SC}}^{\mathrm{dp\ location}}(t) = B_0 + B_{1\mathrm{f}}\sin(\omega t + \theta_1) + B_{2\mathrm{f}}\sin(2\omega t + \theta_2) + B_{3\mathrm{f}}\sin(3\omega t + \theta_3) + \ldots \quad (3.42)$$

where B_0 represents the DC component, and B_{nf} and θ_n correspond to the amplitude and phase of the nth harmonic component, respectively.

Finally, the power of the nth-harmonic response, denoted as P_{nf}, is proportional to the squared amplitude of the corresponding Fourier component:

$$P_{\mathrm{nf}} \propto |B_{\mathrm{nf}}|^2 . \quad (3.43)$$

Notably, P_{nf} is the quantity measured in experiments (second-harmonic response $P_{2\mathrm{f}}$ and third-harmonic response $P_{3\mathrm{f}}$, in particular) and serves as the basis for comparing TDGL simulations with experimental results.

3.6 Toy Model Setup: Superconducting Nb with Local Defects

3.6.1 Introduction to Local Defects

The superconducting samples studied in this thesis are Nb films. From the perspective of vortex dynamics, these Nb films are not defect-free or perfectly homogeneous; instead, they contain local defects that influence vortex behavior. Specifically, Chapters 4 and 5 investigate rf vortex nucleation induced by surface defects in Nb/Cu films, while Chapters 6 and 7 focus on the

dynamics of trapped vortices pinned by pinning sites. Consequently, in the TDGL simulations, the superconducting domain is modeled as Nb with local defects.

3.6.2 Modeling Local Defects in TDGL Simulations

In the toy models studied in this thesis, local defects are modeled as regions composed of a low-T_c impurity phase. In other words, the superconducting domain consists of both Nb and a low-T_c impurity phase, making it inhomogeneous.

Equations 3.21 and 3.22 are applied to both the Nb region and the low-T_c impurity phase region, with inhomogeneity incorporated through the spatial variation of five material-specific parameters: T_c, α, β, γ, and σ. In practice, the values of α and β are determined for a given choice of λ and B_c using Eqs. 3.2 and 3.3.

3.6.3 Material Parameters of Toy Models

Material parameters (penetration depth λ, Ginzburg-Landau parameter κ, etc.) of Nb films vary from one sample to another. For simplicity, in the TDGL simulations, the Nb region adopts the material parameters of bulk Nb, as listed in the first row of Table 1 in Ref. [85]. These adopted values are summarized in the "Nb" sector of Table 3.1.

The choice of material parameters for the low-T_c impurity phase in the toy models is now discussed. For simplicity, the normal state conductivity of the low-T_c impurity phase is set equal to that of Nb. The transition temperature of the impurity phase is chosen as 3 K. Since the penetration depth of the impurity phase is expected to be larger than that of Nb (40 nm), it is set to 90 nm. Since the thermodynamic critical field of the impurity phase is expected to be lower than that of

Parameter name		Symbol	Value
Dipole height		h_{dp}	400 nm
Period of applied rf field		$\frac{1}{f}$	$5.88 \cdot 10^{-10}$ s
Nb	Critical Temperature	$T_{\mathrm{c}}^{\mathrm{Nb}}$	9.3 K
	Penetration depth	λ^{Nb}	40 nm
	Critical field	$B_{\mathrm{c}}^{\mathrm{Nb}}$	200 mT
impurity	Critical Temperature	$T_{\mathrm{c}}^{\mathrm{impurity}}$	3.0 K
	Penetration depth	$\lambda^{\mathrm{impurity}}$	90 nm
	Critical field	$B_{\mathrm{c}}^{\mathrm{impurity}}$	120 mT

Table 3.1: Values of parameters used in TDGL simulations. The superconducting domain of the toy models contains Nb and the low-T_{c} impurity phase.

Nb (200 mT), it is set to 120 mT. The parameters used in the TDGL simulations are summarized in Table 3.1, where the "impurity" sector specifies the material parameters of the low-T_{c} impurity phase region in the toy models.

Chapter 4: TDGL Modeling of rf Vortex Nucleation and Third-Harmonic Response

The studies presented in this chapter are published in Ref. [6].

4.1 Introduction

The objective of this chapter is to investigate the third-harmonic response (P_{3f}) arising from rf vortex nucleation at surface defects through numerical simulations. These simulations provide key insights into the underlying mechanisms of P_{3f}, which will be used to interpret the experimental results presented in Chapter 5. The framework for the TDGL simulations used in this study is detailed in Chapter 3.

To establish a foundation for understanding rf vortex nucleation and nonlinear response, we first examine the case of a defect-free bulk Nb sample ($T_c = 9.3$ K) in Sec. 4.2. We then introduce a phenomenological surface defect toy model (Sec. 4.3) and analyze the key features of the resulting P_{3f} (Sec. 4.4). In particular, we show that the temperature and rf field amplitude dependence of P_{3f} can be qualitatively explained by two parameters of the toy model: (1) the depth to which an rf vortex semi-loop penetrates a sample through a surface defect and (2) the number of surface defects that nucleate rf vortices in each half of the rf cycle. These effects are explored in Secs. 4.5 and 4.6.

In the simulations, the external field is a *localized* rf magnetic field generated by an rf dipole

(see Fig. 3.1). Unlike infinitely extended vortices, the vortices nucleated by the rf dipole are *finite-sized* magnetic vortex semi-loops (rf vortex semi-loops), which are thought to be the generic types of rf vortex excitations created at the surface of SRF cavities [11, 12, 86].

4.2 Defect-Free Bulk Nb

4.2.1 Time-Domain Analysis of rf Vortex Dynamics

Unlike a DC vortex whose behavior shows no time dependence, an rf vortex shows non-trivial dynamics, and should be examined in a time-domain manner. Recall that the transient nature of rf vortices is illustrated in Fig. 1.1. Here we demonstrate the time-domain analysis (focusing on the dynamics of rf vortices) for a specific rf field amplitude ($B_{\rm pk} = 61.6$ mT) and a specific temperature (8.23 K). Material parameters of Nb are used in the defect-free bulk Nb simulations. See Table 3.1.

The dynamics of rf vortex semi-loops for bulk Nb during the first half of an rf cycle (frequency=1.7 GHz, period=5.88×10^{-10}s) is shown in Fig. 4.1, for a fixed rf field amplitude ($B_{\rm pk} = 61.6$ mT) and a fixed temperature (8.23 K). Figure 4.1 (a)-(g) show the space and time dependence of the square of the normalized order parameter ($|\psi/\psi_\infty|^2$) (here 1 means full superconductivity and 0 means no superconductivity); the black region is where $|\psi/\psi_\infty|^2 < 0.03$. Since the order parameter is suppressed significantly at the center of a vortex core, a vortex can be visualized by tracking the black region. Here $\psi_\infty = \psi_\infty(T)$ is the value of the order parameter deep inside bulk Nb at temperature T.

In the early stage of the rf cycle, there is no rf vortex (Fig. 4.1 (a) and (b)), and then an rf vortex semi-loop that is parallel to the direction of the rf dipole (which points in the x-direction)

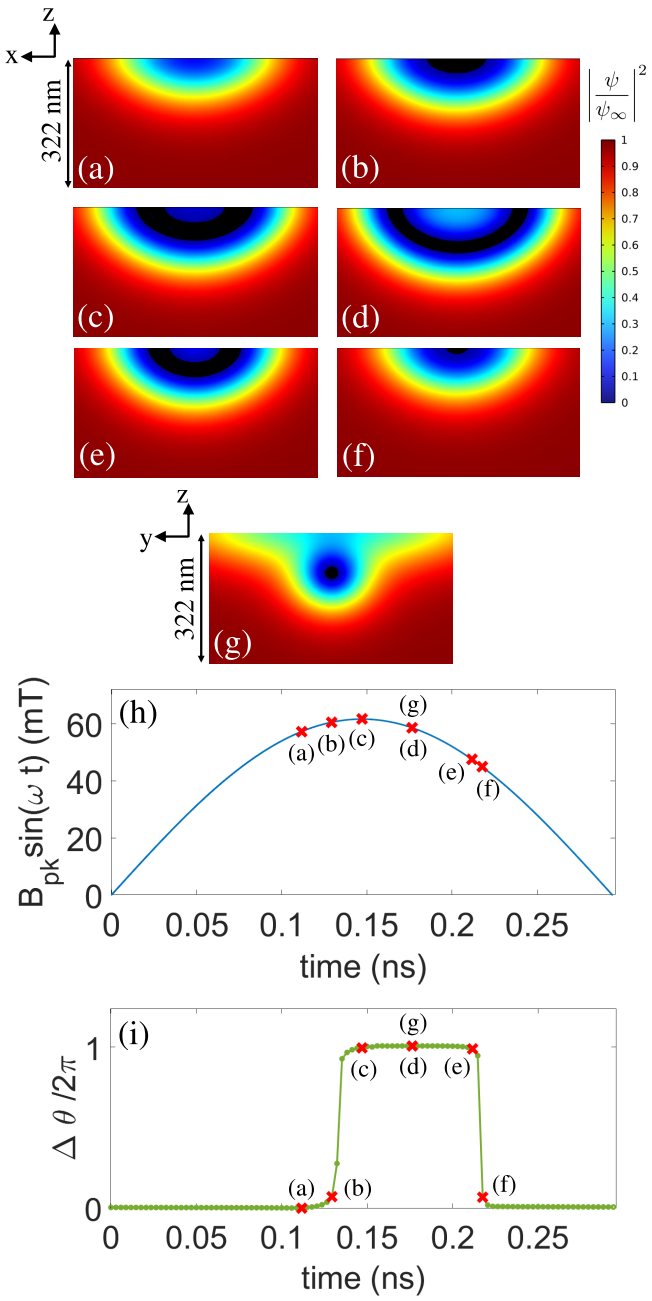

Figure 4.1: Time-domain analysis for the dynamics of rf vortex semi-loops in bulk Nb. A time-dependent magnetic moment (rf dipole) is 400 nm above the superconductor surface, pointing in the x-direction, and producing $B_{\rm pk} = 61.6$ mT at T=8.23 K. (a)-(f) show the square of the normalized order parameter ($|\psi/\psi_\infty|^2$) on the XZ plane cross-section at different times during the first half of the rf cycle. The black region is where $|\psi/\psi_\infty|^2 < 0.03$. (g) shows $|\psi/\psi_\infty|^2$ on the YZ plane cross-section at the same moment as (d). (h) rf field at $(x, y, z) = (0, 0, 0)$ versus time during the first half of the rf cycle. (i) Phase change for a closed contour (on the YZ plane) that is large enough to enclose the entire non-trivial region. Red crosses in (h) and (i) correspond to snapshots (a)-(g).

shows up (Fig. 4.1 (c), (d), (e) and (g)). The rf vortex semi-loop disappears later in the rf cycle (Fig. 4.1 (f)).

Besides examining the spatial distribution of the order parameter, another signature of vortices is the phase of the order parameter. Because Ginzburg-Landau theory is based on the existence of a single-valued complex superconducting order parameter ($\psi = |\psi|e^{i\theta}$), the phase θ must change by integral multiples of 2π in making a closed contour (see equation (4.45) in [1]), namely

$$\oint ds \cdot \nabla\theta = 2\pi N, \tag{4.1}$$

where N is a positive or negative integer, or zero. The integral $\frac{1}{2\pi}\oint ds \cdot \nabla\theta$ is quantized, and corresponds to the number of vortices enclosed by the closed contour.

Figure 4.1 (i) shows the value of the integral $\frac{1}{2\pi}\oint ds \cdot \nabla\theta$ (namely $\Delta\theta/2\pi$) as a function of time. The contour is on the YZ plane and is large enough to enclose the entire non-trivial region. Note that Figs. 4.1 (h) and (i) share a common horizontal axis. Based on Fig. 4.1 (i), there are no vortices at the moments of (a), (b) and (f), and there is one vortex at the moments of (c), (d) and (e), which agrees with the order parameter analysis (Fig. 4.1 (a)-(g)).

The time-domain analysis described here (space and time dependence of the order parameter (Fig. 4.1 (a)-(g)) and $\Delta\theta/2\pi$ (Fig. 4.1 (i))) is applied to all TDGL simulations in this chapter whenever we check whether or not there are rf vortex semi-loops.

4.2.2 Screening Current Distribution and Superconductor Response

In addition to the spatial and temporal behavior of the order parameter, it is also informative to examine the screening current density J_{sc}.

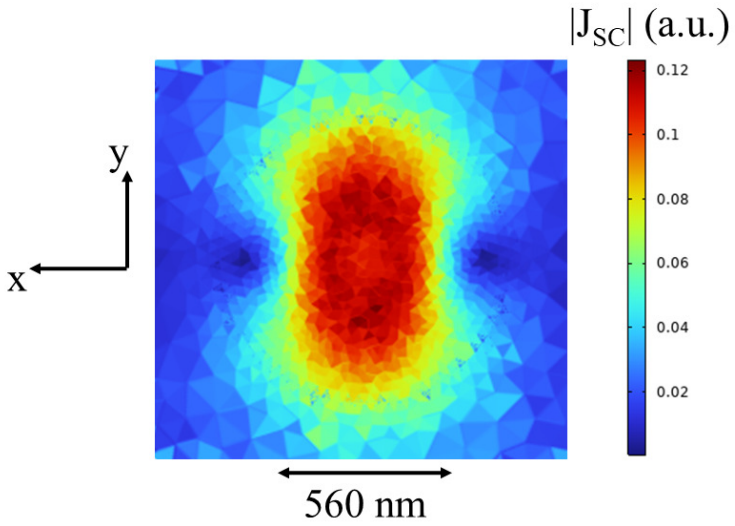

Figure 4.2: Spatial distribution of the screening current density $J_{\rm sc}(x, y)$ at the surface ($z = 0$) of bulk Nb, obtained from a TDGL simulation. The superconductor is subjected to a localized rf magnetic field generated by a time-dependent magnetic moment (rf dipole) located 400 nm above the superconductor surface, oriented along the x-direction, and producing a peak field amplitude of $B_{\rm pk} = 61.6$ mT. The simulation is performed at a temperature of $T = 7.77$ K, under which the superconductor remains in the Meissner state (no rf vortex semi-loops). The snapshot is taken at $t = \pi/2$, corresponding to the moment when the rf field reaches its maximum. The origin $(x, y) = (0, 0)$ is at the center of the image. The color scale represents the magnitude of $J_{\rm sc}$ in arbitrary units (a.u.).

Figure 4.2 shows the spatial distribution of the screening current density $J_{\rm sc}(x, y)$ at the surface ($z = 0$) of bulk Nb, obtained from a TDGL simulation. The superconductor is subjected to a localized rf magnetic field generated by a time-dependent magnetic moment (rf dipole) located 400 nm above the superconductor surface, oriented along the x-direction, and producing a peak field amplitude of $B_{\rm pk} = 61.6$ mT. The simulation is performed at a temperature of $T = 7.77$ K, under which the superconductor remains in the Meissner state (no rf vortex semi-loops). The snapshot is taken at $t = \pi/2$, corresponding to the moment when the rf field reaches its maximum. The origin $(x, y) = (0, 0)$ is at the center of the image. The color scale represents the magnitude of $J_{\rm sc}$ in arbitrary units (a.u.).

The red region in Fig. 4.2 corresponds to areas of strong screening current. The screening current distribution shown in Fig. 4.2 indicates that the field of view of the rf dipole—corresponding to the microwave microscope probe used in experiments—is confined to sub-micron length scales.

Figure 4.3(a) shows the TDGL simulation result of the spatial distribution of the screening current density $J_{\rm sc}(x, y)$ at the surface ($z = 0$) of bulk Nb, subjected to a localized rf magnetic field. The field is generated by a time-dependent magnetic moment (rf dipole) located 400 nm above the superconductor surface, oriented along the x-direction, and producing a peak field amplitude of $B_{\rm pk} = 61.6$ mT. The simulation temperature is $T = 8.32$ K. For this combination of $B_{\rm pk}$ and T, an rf vortex semi-loop nucleates in the superconductor. The snapshot is taken at $t = \pi/2$, corresponding to the moment when the rf field reaches its maximum. The origin $(x, y) = (0, 0)$ is at the center of the figure. The color scale represents the magnitude of $J_{\rm sc}$ in arbitrary units (a.u.).

The red region in Fig. 4.3(a) corresponds to areas of strong screening current. The screening current distribution shown in Fig. 4.3(a) indicates that the field of view of the rf

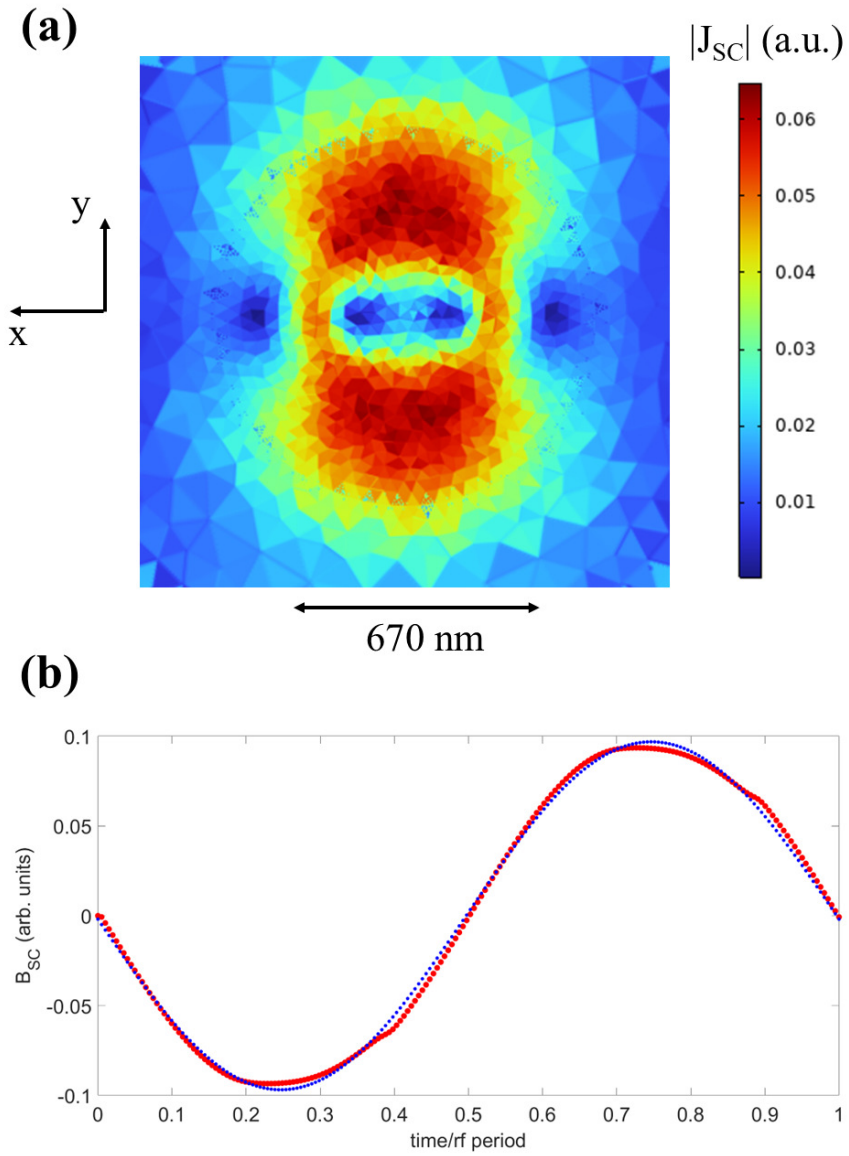

Figure 4.3: TDGL simulation result of bulk Nb, subjected to a localized rf magnetic field. The field is generated by a time-dependent magnetic moment (rf dipole) located 400 nm above the superconductor surface, oriented along the x-direction, and producing a peak field amplitude of $B_{\rm pk} = 61.6$ mT. The simulation temperature is $T = 8.32$ K. For this combination of $B_{\rm pk}$ and T, an rf vortex semi-loop nucleates in the superconductor. (a) shows the spatial distribution of the screening current density $J_{\rm sc}(x, y)$ at the surface ($z = 0$) of bulk Nb. The snapshot is taken at $t = \pi/2$, corresponding to the moment when the rf field reaches its maximum. The origin $(x, y) = (0, 0)$ is at the center of the figure. The color scale represents the magnitude of $J_{\rm sc}$ in arbitrary units (a.u.). (b) The red curve shows the superconducting response $B_{\rm sc}$ at the dipole location over one rf cycle, while the blue curve represents its linear (fundamental frequency) component.

dipole—corresponding to the microwave microscope probe used in experiments—is confined to sub-micron length scales.

The superconducting response B_{sc}—the magnetic field generated by the screening current—is shown in Fig. 4.3(b) at the dipole location over one rf cycle. In the figure, the red curve corresponds to the full B_{sc} signal, while the blue curve represents its linear (fundamental frequency) component. The clear deviation of the red curve from the blue curve indicates the presence of nonlinear components in the superconducting response.

Note that the field of view of the rf dipole is confined to sub-micron length scales, regardless of whether the superconductor remains in the Meissner state (Fig. 4.2) or an rf vortex semi-loop nucleates (Fig. 4.3(a)).

4.2.3 Temperature Dependence of rf Vortex Dynamics and $P_{3\mathrm{f}}$

Equipped with the picture of rf vortex nucleation, now let's move on to the resulting $P_{3\mathrm{f}}$. The simulation result of $P_{3\mathrm{f}}(T)$ for a fixed rf field amplitude ($B_{\mathrm{pk}} = 61.6$ mT) for bulk Nb is shown in Fig. 4.4 (a). The bell-shaped structure $P_{3\mathrm{f}}(T)$ in Fig. 4.4 (a) can be decomposed into three segments (separated by the two dashed vertical black lines) and can be understood with the vortex penetration field $B^{\mathrm{rf}}_{\mathrm{vortex}}(T)$ and the strength of superconductivity. (The vortex penetration field $B^{\mathrm{rf}}_{\mathrm{vortex}}(T)$ will be explored in more detail in the next section.) An rf vortex semi-loop shows up when $B_{\mathrm{pk}} > B^{\mathrm{rf}}_{\mathrm{vortex}}(T)$. Below 8.1 K, $B^{\mathrm{rf}}_{\mathrm{vortex}}(T) > B_{\mathrm{pk}}$ and hence the entire bulk Nb is in the vortex-free Meissner state (see Fig. 4.4 (b) and the purple curve in (f)), whose nonlinear response is weak. As temperature increases, $B^{\mathrm{rf}}_{\mathrm{vortex}}(T)$ decreases and hence B_{pk} would be greater than $B^{\mathrm{rf}}_{\mathrm{vortex}}(T)$ at a certain temperature depending on the strength of the rf stimulus. In this simulation

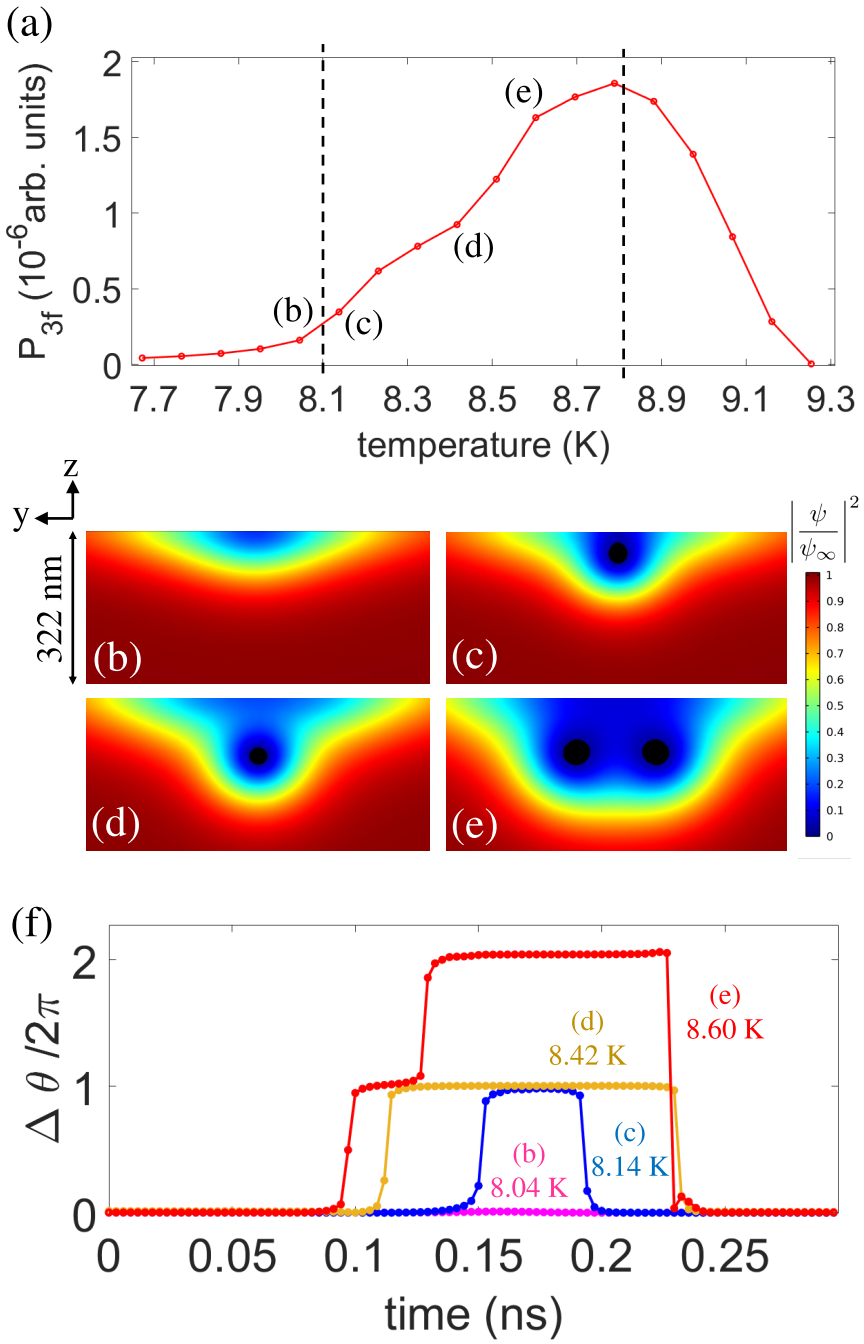

Figure 4.4: (a) TDGL simulation result of $P_{3f}(T)$ for a fixed rf field amplitude ($B_{pk} = 61.6$ mT) imposed by a point dipole source for bulk Nb. From left to right, P_{3f} is weak at low temperatures (below 8.1 K), then increases with temperature (between 8.1 K and 8.8 K), and drops with the temperature at high temperatures (above 8.8 K). (b)-(e) show $|\psi/\psi_\infty|^2$ on the YZ plane cross-section at 8.04 K, 8.14 K, 8.42 K, and 8.60 K, respectively. The black region is where $|\psi/\psi_\infty|^2 < 0.03$. These snapshots are taken at $\omega t = 0.6\pi$. (f) shows $\Delta\theta/2\pi$ versus time for the four temperatures.

($B_{\rm pk} = 61.6$ mT), from the full time-domain simulation (see the discussion for Fig. 4.1) one finds that there is one rf vortex semi-loop (beneath the rf magnetic dipole) that penetrates the surface of the bulk Nb when the temperature is around 8.14 K (see Fig. 4.4 (c) and the blue curve in (f)). Roughly speaking, this implies that $B^{\rm rf}_{\rm vortex}(T = 8.14\ {\rm K}) \approx 61.6$ mT. As temperature increases, $B^{\rm rf}_{\rm vortex}(T)$ drops and vortex nucleation is favorable, and indeed the second rf vortex semi-loop shows up around 8.6 K (see Fig. 4.4 (e) and the red curve in (f)) and thus $P_{\rm 3f}$ increases with temperature between 8.1 K and 8.8 K. Besides examining the order parameter (Fig. 4.4 (b)-(e)), Fig. 4.4 (f) also shows how the vortex number and duration change with temperature.

The nonlinear response of the superconductor is determined not only by the number of vortices (as described above in the language of $B^{\rm rf}_{\rm vortex}(T)$) but also by the strength of superconductivity. As the temperature approaches the transition temperature of a superconductor, its superconductivity and hence nonlinear response becomes weak. Such a temperature dependence leads to the decreasing tail of $P_{\rm 3f}(T)$ above 8.8 K in Fig. 4.4 (a).

The simulation results shown in Fig. 4.4 are based on the rf dipole model described in Sec. 3.4.1. This model serves as a first-order approximation to the magnetic field produced by the microwave microscope probe in the experiment. The objective of the TDGL simulations in this thesis is to qualitatively—rather than quantitatively—capture the essential physics beneath the probe. Specifically, we do not aim to reproduce the exact geometry of an rf vortex semi-loop nucleated beneath the probe, nor to precisely reproduce the quantitative details of the resulting $P_{\rm 3f}(T)$.

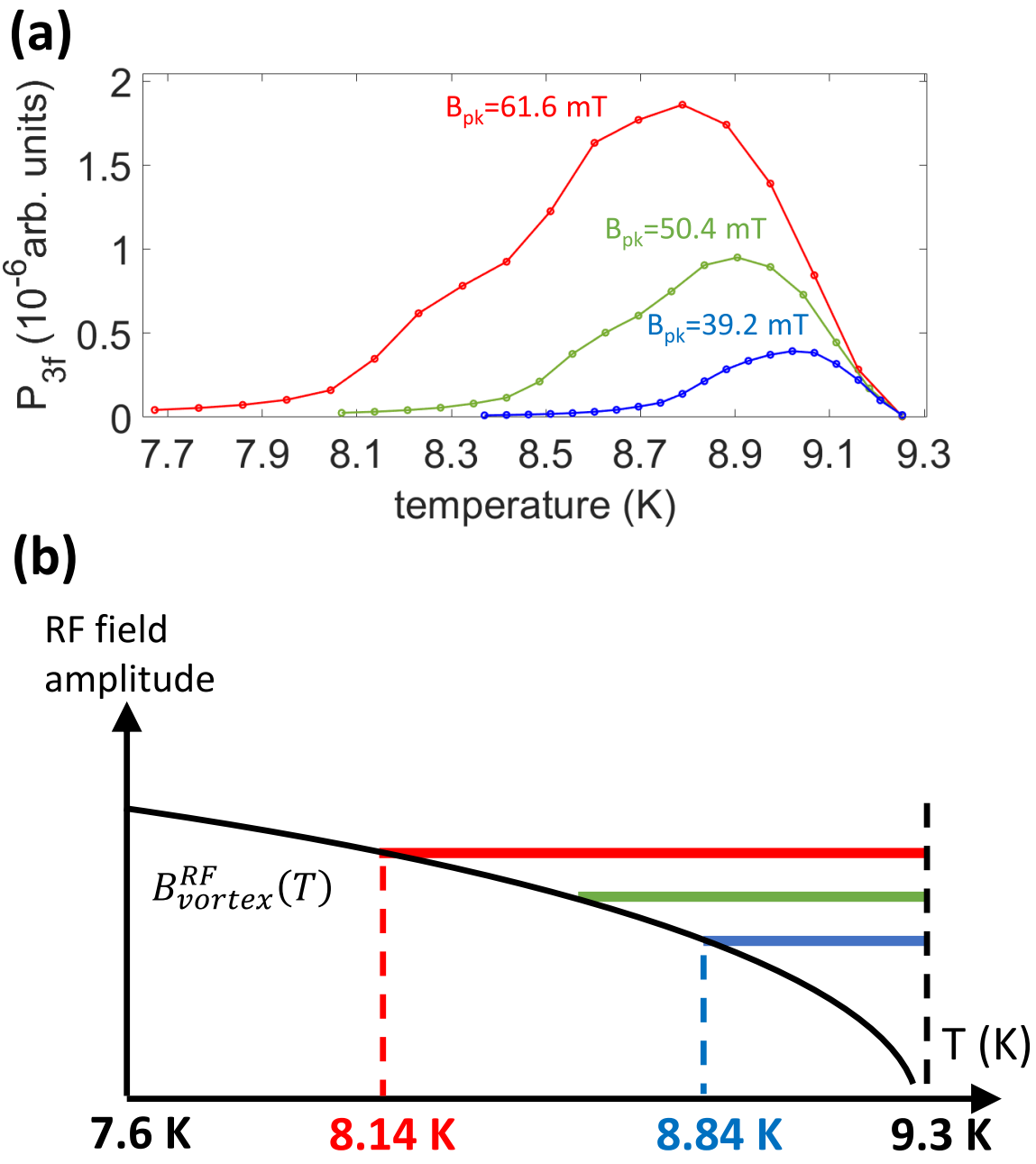

Figure 4.5: (a) TDGL simulation result of $P_{3f}(T)$ for three different rf field amplitudes for bulk Nb. (b) Schematic of the vortex penetration field $B^{rf}_{vortex}(T)$ (the black curve) and the temperature range of $P_{3f}(T)$ bell-shaped structure for the three rf field amplitudes (the three colorful horizontal lines). The y-axis is the rf field amplitude. Note that (a) and (b) share the same horizontal axis and the same color-coded rf field amplitudes.

4.2.4 Vortex Penetration Field and rf Field Dependence of $P_{3f}(T)$

Figure 4.5 (a) summarizes the simulation results of $P_{3f}(T)$ for three different rf field amplitudes for bulk Nb. For all three rf field amplitudes, P_{3f} is weak at low temperatures ($B_{pk} < B^{rf}_{vortex}(T)$, vortex-free Meissner state), arises at high temperatures ($B_{pk} > B^{rf}_{vortex}(T)$, rf vortex semi-loops), and then drops with temperature as the temperature is near the critical temperature. For the red curve, the first vortex semi-loop shows up around 8.14 K, which implies $B^{rf}_{vortex}(T = 8.14\text{ K}) \approx 61.6$ mT; for the blue curve, the first vortex semi-loop shows up around 8.84 K, which implies $B^{rf}_{vortex}(T = 8.84\text{ K}) \approx 39.2$ mT. Figure 4.5 (b) illustrates $B^{rf}_{vortex}(T)$ and the rf field amplitude dependence of the temperature range of $P_{3f}(T)$ bell-shaped structure. In this rf field amplitude-temperature phase diagram, the region below $B^{rf}_{vortex}(T)$ corresponds to the vortex-free Meissner state, while rf vortex semi-loops show up in the region above $B^{rf}_{vortex}(T)$. It is clear that the $P_{3f}(T)$ bell-shaped structure extends to lower temperatures as the rf field amplitude becomes stronger (from the blue to the green to the red in Fig. 4.5 (a) and (b)) because of the temperature dependence of $B^{rf}_{vortex}(T)$.

Having developed an understanding of P_{3f}, rf vortex semi-loops, and their dependence on temperature and rf field amplitude in defect-free bulk Nb, we now turn to the case of Nb with surface defects.

4.3 rf Vortex Nulceation in Grain Boundaries

4.3.1 Two Key Phenomenological Parameters for rf Vortex Nucleation

Quantitatively comparing the details of the measured P_{3f} among different Nb films is challenging for two main reasons. Firstly, the specifics of P_{3f} depend on the probe-sample separation, which is difficult to reproduce. Secondly, different Nb films might possess different types of surface defects that nucleate rf vortices. For example, grain boundaries may be the primary sources of P_{3f} for one Nb film, while dislocations could be the main sources of P_{3f} for another Nb film.

Although the details of rf vortex nucleation (and the resulting P_{3f}) by various surface defects are complicated and depend on details, we can analyze the dynamics of rf vortex nucleation in a phenomenological way and extract qualitative information. On the phenomenological level, the dynamics of rf vortices penetrating a sample surface through surface defects can be quantified by means of two key aspects: how many surface defects that nucleate rf vortices (ρ^{defect}) exist, and how deep do rf vortices travel into a sample through surface defects in half an rf cycle ($h^{\text{defect}}_{\text{penetration}}$)?

Here we illustrate the concept of $h^{\text{defect}}_{\text{penetration}}$ by considering rf vortex nucleation at grain boundaries in Nb films. For a given grain boundary that nucleates an rf vortex, the depth the rf vortex travels into the Nb film through the grain boundary in half an rf cycle ($h^{\text{defect}}_{\text{penetration}}$) is determined by multiple factors, including the width of the grain boundary, the angle between the grain boundary and the Nb film surface, the material properties of the impurity phases in the grain boundary, etc. Instead of considering the details of all possible microstructures, we adopt a phenomenological approach, where $h^{\text{defect}}_{\text{penetration}}$ serves as the phenomenological characterization of

the depth the rf vortex travels into the Nb film through the grain boundary in half an rf cycle.

4.3.2 Surface Defect Toy Model: Low-T_c Material in Nb Grain Boundaries

Nb is known to contain low-T_c impurity phases, such as the oxides of Nb [87–92]. In such phases, oxygen forms a solid solution in Nb and produces materials with critical temperatures below the bulk T_c of pure Nb (9.3 K) [93–95]. Nb samples with higher oxygen content tend to have a lower critical temperature. For instance, T_c drops to around 7.33 K for 2% oxygen content, and drops to around 6.13 K for 3.5% oxygen content [94]. Another class of low-T_c impurity phases in Nb are the niobium hydrides [96, 97], and some of these phases exhibit superconducting transitions around 1.3 K [98].

Motivated by the existence of these low-T_c impurity phases, here we consider a phenomenological surface defect toy model in which the grain boundaries of Nb host the low-T_c material (impurity phases). Such grain boundaries might serve as weak spots for vortex nucleation. As shown later in this chapter, the proximity effect is active in this model of the grain boundaries. Here we consider one possible toy model realization of "Nb grain boundaries filled with low-T_c material". Of course, the phenomenological toy model (a grain boundary model) considered here is just one possible scenario of surface defects that might be able to qualitatively explain the experimental results. rf vortices are more prone to nucleate at wide grain boundaries compared to narrow ones. Consequently, instead of characterizing a typical grain boundary in Nb films, the toy model is designed to characterize specifically those that are wide.

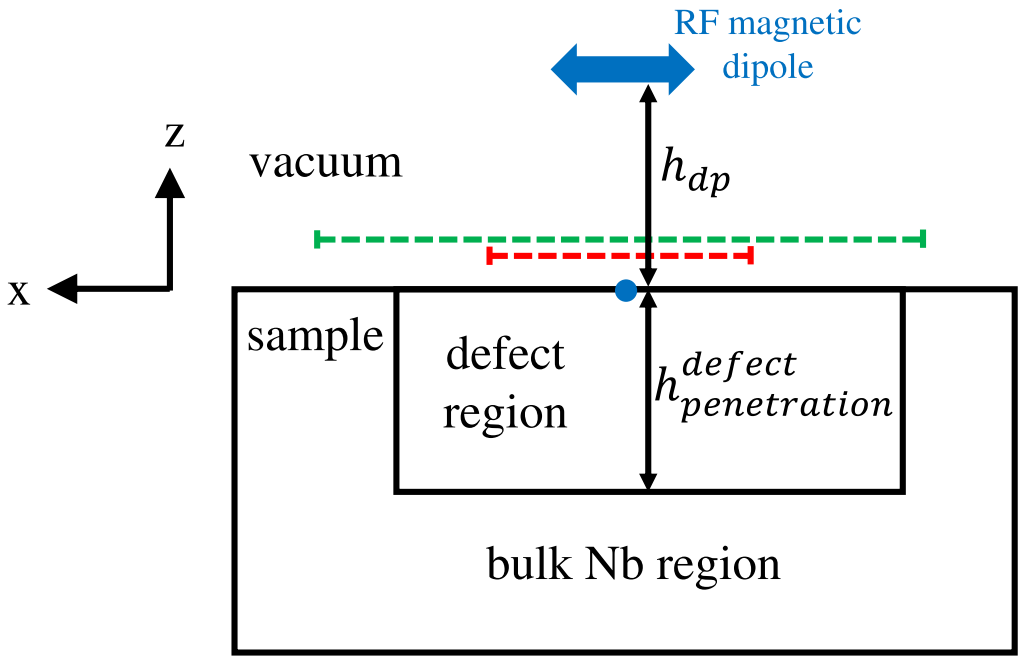

Figure 4.6: Sketch of the side view (XZ plane) of the grain boundary model. The origin is marked by a blue dot. The rf dipole is represented by the blue double arrow. The schematic is not to scale (h_{dp}=400 nm and $h^{\mathrm{defect}}_{\mathrm{penetration}}$=200 nm). Since the physics around the origin plays a dominant role, the region far away from the origin is set to be defect-free bulk Nb to reduce computational time. In addition, the region below $z = -h^{\mathrm{defect}}_{\mathrm{penetration}}$ is also set to be bulk Nb for simplicity. Note that the model is not cylindrically symmetric. The top view of the region indicated by the red dashed line is shown in Fig. 4.7 (b), and the top view of the region indicated by the green dashed line is shown in Fig. 4.8.

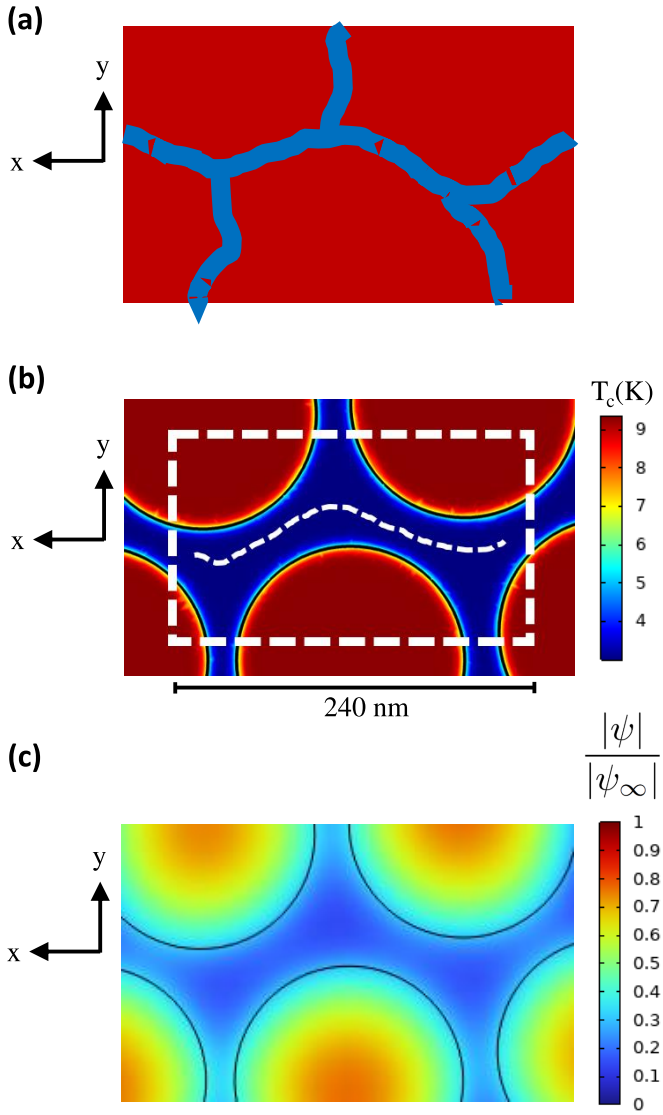

Figure 4.7: A top view schematic of the grain boundary model. (a) Illustration of Nb grains and grain boundaries, with red being Nb grains and blue being grain boundaries filled with impurity phases. The realization of this illustration used in the TDGL simulations is shown in (b). (b) The distribution of critical temperature on the XY plane around the origin (corresponds to the region indicated by the red dashed line in Fig. 4.6), with red being Nb and blue being the low-T_c impurity phase with $T_c^{\text{impurity}} = 3$ K. Here $(x, y, z) = (0, 0, 0)$ is at the center. The rf dipole is located at $(x, y, z) = (0, 0, 400 \text{ nm})$ and points in the x-direction. The white dashed curve indicates the grain boundary that is roughly parallel to the x-direction. The model defect region is indicated by the white dashed rectangle. (c) A snapshot of the distribution of normalized order parameter $|\psi/\psi_\infty|$ obtained by a TDGL simulation with the temperature being 5.2 K (higher than T_c^{impurity}) and $B_{\text{pk}} = 50.9$ mT. This snapshot is taken at the end of an rf cycle, namely when the rf field drops to zero ($\omega t = 2\pi$ and hence $B_{\text{rf}}\sin(\omega t) = 0$). The normalized order parameter of the dark blue region is around 0.18.

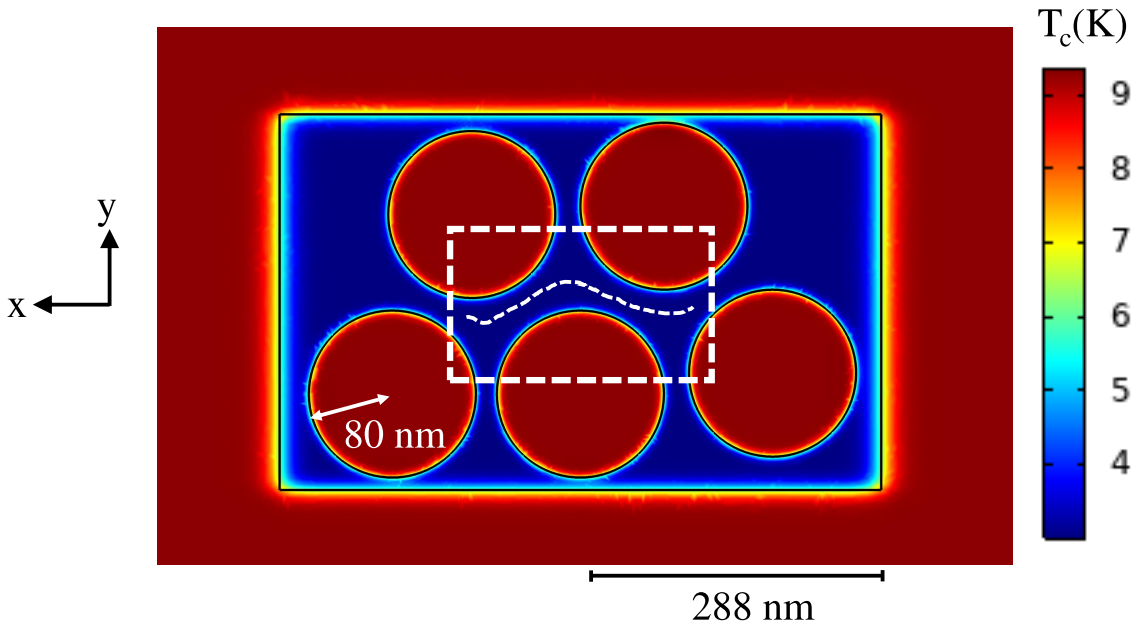

Figure 4.8: A spatially extended view of the distribution of critical temperature on the XY plane for the grain boundary model. The region shown here corresponds to the region indicated by the green dashed line in Fig. 4.6.

4.3.3 Geometry and Parameters of the Grain Boundary Model

Fig. 4.6 shows the side view of the grain boundary model. By the very definition of $h^{\text{defect}}_{\text{penetration}}$, we constrain the rf vortices to only probe the region of $0 > z > -h^{\text{defect}}_{\text{penetration}}$, and hence the details in the region of $z < -h^{\text{defect}}_{\text{penetration}}$ play a minor role. As a result, this region can be treated as bulk Nb as an approximation. (In summary, $z = 0$: sample surface; $0 > z > -h^{\text{defect}}_{\text{penetration}}$: defect whose XY cross-section is shown in Fig. 4.7 (b); $z < -h^{\text{defect}}_{\text{penetration}}$: bulk Nb.) Here $h^{\text{defect}}_{\text{penetration}}$ is set to be 200 nm.

The rf dipole is located at $(0, 0, h_{\text{dp}})$ and hence vortex semi-loops first show up near $(x, y, z) = (0, 0, 0)$. Therefore, the physics around the origin plays a dominant role. As an approximation, surface defects (Nb grain boundaries filled with low-T_{c} material) are introduced

near the origin (illustrated in Fig. 4.6), while the region far away from the origin is set to be defect-free bulk Nb to reduce computational time. As a result, only the region around the origin characterizes the grain boundary scenario accurately (the model defect region), and thus the screening current is collected only from this region when calculating $P_{3\mathrm{f}}$.

The side view of the grain boundary model is shown in Fig. 4.6, and the top view ($(x, y, z = 0)$) is shown in Fig. 4.7. Figure 4.7 (a) is an illustration of an Nb surface containing Nb grains (red) and grain boundaries filled with low-T_c impurity phases (blue). The realization used in the TDGL simulations is shown in Fig. 4.7 (b). Figure 4.7 (b) is a top view of the sample critical temperature distribution around the origin of the grain boundary model: the red region means Nb with $T_\mathrm{c} = 9.3$ K, and the blue region means the low-T_c impurity phase with $T_\mathrm{c}^{\mathrm{impurity}} = 3$ K. (Parameters of the grain boundary model are given in Table 3.1.) The origin is at the center of Fig. 4.7 (b). The geometry is intentionally asymmetric in both the x-direction and the y-direction to prevent symmetry-induced artifacts. A top view of the sample critical temperature distribution with a broader scope (containing the defect region together with the bulk Nb region) is shown in Fig. 4.8. Compared to Fig. 4.7 (b), Fig. 4.8 shows the setup over a broader spatial extent as indicated by the green dashed line in Fig. 4.6. Figure 4.8 contains the entire defect region (the five Nb grains and the blue region) and part of the bulk Nb region as shown in Fig. 4.6.

An rf vortex semi-loop that nucleates in the sample tends to be parallel to the direction of the rf dipole, which points in the x-direction. Therefore, as $B_\mathrm{pk} > B_{\mathrm{vortex}}^{\mathrm{rf}}(T)$, rf vortex semi-loops show up in the grain boundaries that are roughly parallel to the x-direction. Note that there is one grain boundary in Fig. 4.7 (b) that is roughly parallel to the x-direction, which is marked by a white dashed curve.

It is worth mentioning that the proximity effect shows up naturally in TDGL simulations.

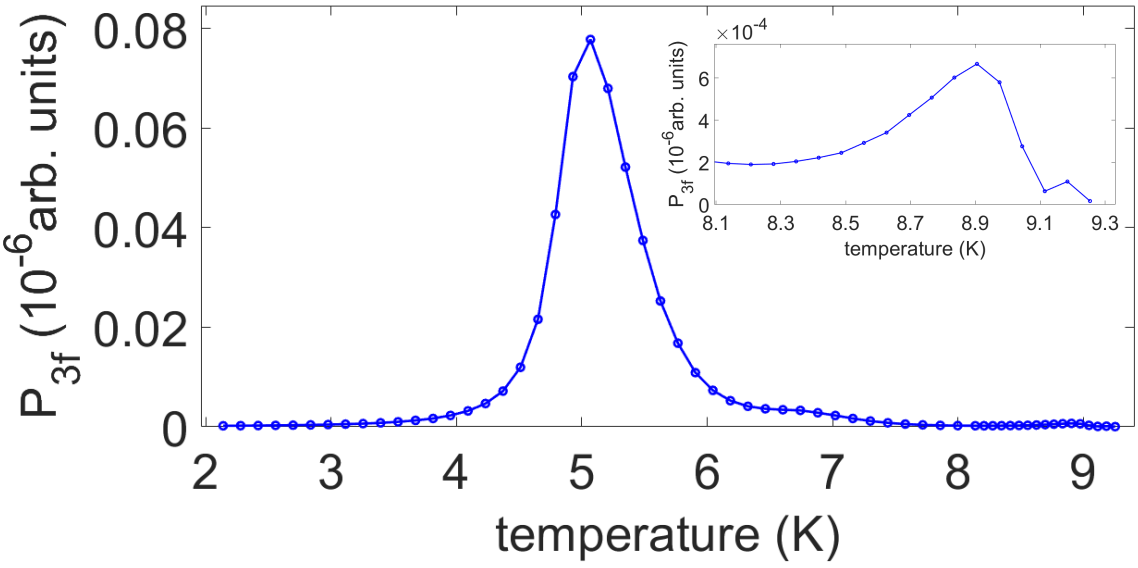

Figure 4.9: TDGL simulation result of $P_{3f}(T)$ for the grain boundary model presented in Sec. 4.3.3. Here $h^{\text{defect}}_{\text{penetration}} = 200$ nm and $B_{\text{pk}} = 50.9$ mT. Inset: enlargement of the figure above 8.1 K.

Fig. 4.7 (c) shows a snapshot of the distribution of normalized order parameter $|\psi/\psi_\infty|$ (here 1 means full superconductivity and 0 means no superconductivity) obtained by a TDGL simulation with the temperature being 5.2 K and $B_{\text{pk}} = 50.9$ mT. This snapshot is taken at the end of an rf cycle, namely when the rf field drops to zero ($\omega t = 2\pi$ and hence $B_{\text{rf}}\sin(\omega t) = 0$). Due to the proximity effect, the normalized order parameter of the dark blue region is around 0.18 but not zero, even though the temperature (5.2 K) is higher than $T_{\text{c}}^{\text{impurity}}$ (3 K). As a result, a grain boundary filled with a low-T_{c} impurity phase can host rf vortices even for $T > T_{\text{c}}^{\text{impurity}}$.

4.3.4 rf Vortex Nucleation and $P_{3f}(T)$

Figure 4.9 shows the simulation result of $P_{3f}(T)$ for the grain boundary model presented in Sec. 4.3.3. Compared to the P_{3f} around 8.9 K, the P_{3f} between 4.5 K and 6 K is much stronger. In other words, in the presence of surface defects, P_{3f} generated by surface defects is much stronger

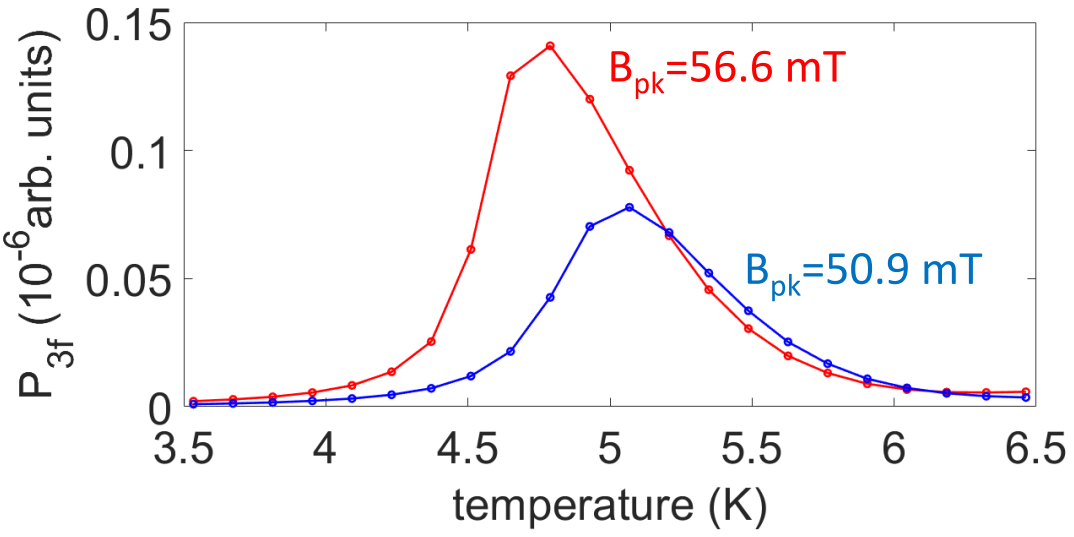

Figure 4.10: TDGL simulation result of $P_{3f}(T)$ for two different rf field amplitudes for the grain boundary model presented in Sec. 4.3.3. Here $h^{\text{defect}}_{\text{penetration}} = 200$ nm.

than the intrinsic P_{3f} of Nb. In the following, we focus on the P_{3f} generated by surface defects.

Figure 4.10 shows the simulation result of $P_{3f}(T)$ for two different rf field amplitudes for the grain boundary model. At low temperatures, the sample is in the Meissner state and P_{3f} is weak. As temperature increases, rf vortex semi-loops nucleate in the grain boundary marked by the white dashed curve in Fig. 4.7 (b) and result in strong P_{3f}. (The existence of rf vortex semi-loops is verified by examining the order parameter in a time-domain manner as described in Fig. 4.1.) This can be interpreted as $B_{\text{pk}} > B^{\text{rf}}_{\text{vortex}}(T)$, where $B^{\text{rf}}_{\text{vortex}}(T)$ is the vortex penetration field of the region around that specific grain boundary. Note that rf vortex semi-loops show up in the grain boundary, indicating that the grain boundary serves as the weak spot for rf vortex nucleation.

As the rf field amplitude increases (blue to red in Fig. 4.10), the $P_{3f}(T)$ maximum increases; in addition, the $P_{3f}(T)$ maximum and the $P_{3f}(T)$ low-temperature onset both show up at a lower temperature.

Here the upper onset temperature of P_{3f} is around 6 K. In the following, such a P_{3f} onset temperature is called the P_{3f} transition temperature and is denoted as $T_c^{P_{3f}}$. The grain boundary model is a mixture of the $T_c^{Nb} = 9.3$ K Nb and the $T_c^{impurity} = 3$ K impurity phase, and hence $T_c^{P_{3f}}$ is between 3 K and 9.3 K. Of course, the numerical value of $T_c^{P_{3f}}$ depends on how the Nb and the impurity phase are distributed. Our objective with this model is not to propose a specific microstructure of the sample, but to illustrate the generic nonlinear properties of a proximity-coupled defective region of the sample.

4.4 Four Key Features of $P_{3f}(T)$ Due to rf Vortex Nucleation

The $P_{3f}(T)$ due to rf vortex nucleation in the grain boundary model (see Fig. 4.9 and Fig. 4.10) exhibits four key features:

1. $P_{3f}(T)$ onsets at a temperature $T_c^{P_{3f}}$ below the bulk T_c of Nb and follows a bell-shaped curve.

2. The maximum value of $P_{3f}(T)$ increases with increasing rf field amplitude.

3. The temperature at which $P_{3f}(T)$ reaches its maximum decreases as the rf field amplitude increases.

4. The low-temperature onset of $P_{3f}(T)$ shifts to lower temperatures for stronger rf field amplitudes.

Besides the grain boundary model, these four key features are also clearly observed for defect-free bulk Nb, as shown in Fig. 4.5 (a), with one exception: in Fig. 4.5 (a), the onset temperature of $P_{3f}(T)$ coincides with $T_c = 9.3$ K, rather than appearing below it. This difference

arises because the simulation in Fig. 4.5 models defect-free bulk Nb rather than a superconductor with surface defects.

The fact that both defect-free bulk Nb and the grain boundary model exhibit the same four key features of $P_{3f}(T)$ suggests that these features are intrinsic signatures of rf vortex nucleation. Therefore, the physical picture illustrated in Fig. 4.5 (b) can also be applied to the grain boundary model, with two modifications: (1) the onset temperature $T_c^{P_{3f}}$ is 6 K rather than 9.3 K, and (2) $B_{\text{vortex}}^{\text{rf}}(T)$ represents the vortex penetration field of the region around the specific grain boundary, rather than a bulk property.

In Chapter 5, we will see that these four key features of $P_{3f}(T)$ are consistently observed in the experimental measurements of Nb/Cu films.

4.5 Effect of $h_{\text{penetration}}^{\text{defect}}$ on $P_{3f}(T)$

In Sec. 4.3.4, $h_{\text{penetration}}^{\text{defect}}$ is set to be 200 nm. Here we consider the effect of varying $h_{\text{penetration}}^{\text{defect}}$, with everything else being the same as described in Sec. 4.3.4.

Figure 4.11 (a) shows the result for $h_{\text{penetration}}^{\text{defect}} = 160$ nm. In Fig. 4.11 (a), a stronger rf field amplitude leads to a stronger P_{3f} for all temperatures. On the contrary, $P_{3f}(T)$ in Fig. 4.10 ($h_{\text{penetration}}^{\text{defect}} = 200$ nm) shows a "crossing" effect: a stronger rf field amplitude leads to a weaker P_{3f} (the red curve is below the blue curve) for temperatures close to $T_c^{P_{3f}}$. The temperature where the red curve ($P_{3f}(T)$ with a strong rf field amplitude) and the blue curve ($P_{3f}(T)$ with a weak rf field amplitude) cross is denoted as T^*. The numerical value of the crossing temperature T^* depends on the choice of the two rf field amplitudes (Here $B_{\text{pk}} = 56.6$ mT and 50.9 mT). For Fig. 4.11 (a), there is no crossing and hence $T^* = T_c^{P_{3f}} = 6$ K. For Fig. 4.10, $T^* = 5.2$ K $< T_c^{P_{3f}} = 6$ K.

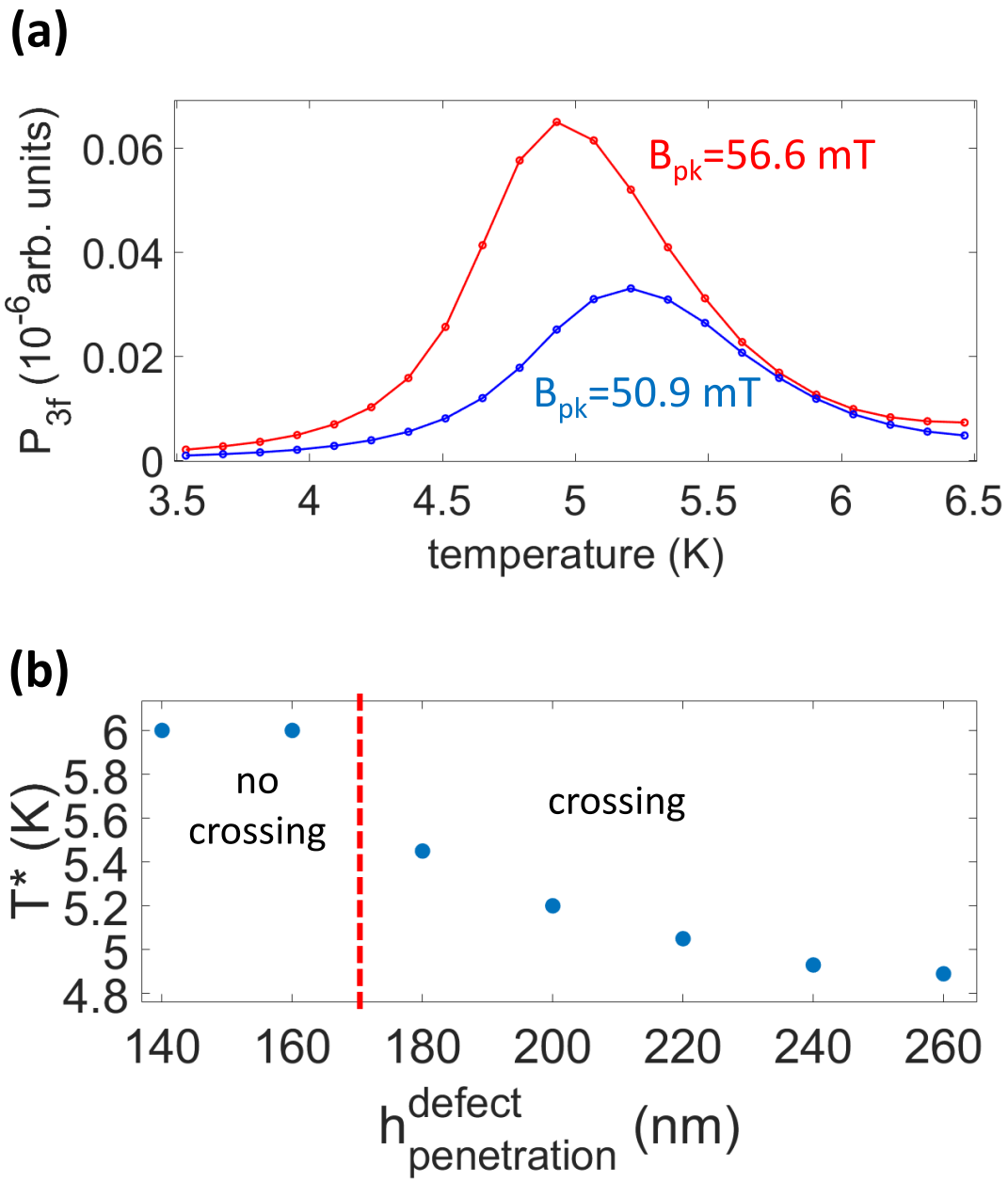

Figure 4.11: (a) TDGL simulation result of $P_{3f}(T)$ for two different rf field amplitudes for the grain boundary model presented in Sec. 4.3.3 for $h^{\text{defect}}_{\text{penetration}} = 160$ nm. (b) Crossing temperature T^* as a function of $h^{\text{defect}}_{\text{penetration}}$.

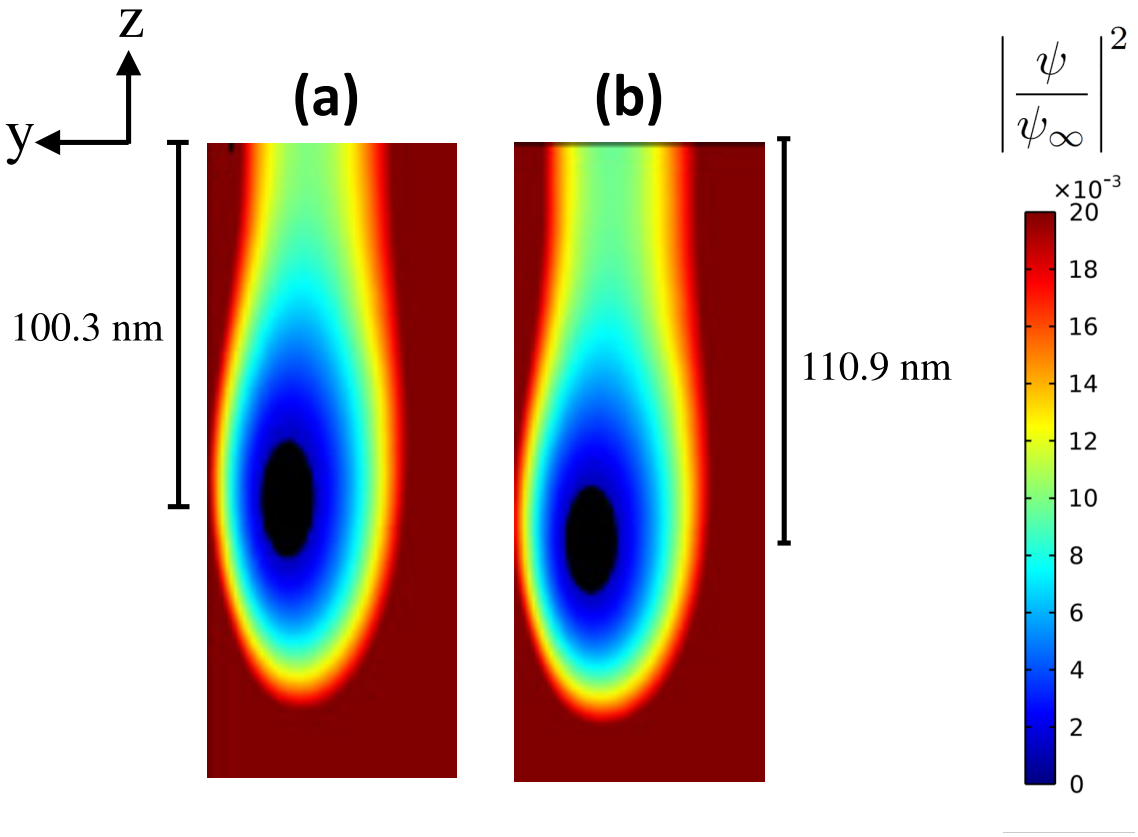

Figure 4.12: A snapshot of the vortex core obtained by the TDGL simulation for the grain boundary model presented in Sec. 4.3.3 for $B_{\rm pk} = 50.9$ mT (a) and for $B_{\rm pk} = 56.6$ mT (b), with the temperature being 5.5 K and $h^{\rm defect}_{\rm penetration} = 200$ nm. This snapshot is taken when the rf field reaches its maximum in an rf cycle ($\omega t = \pi/2$ and hence $B_{\rm rf}\sin(\omega t) = B_{\rm rf}$). The snapshot shows the distribution of the square of the normalized order parameter on the YZ plane immediately below the dipole around the grain boundary that nucleates an rf vortex semi-loop. The black region is where $|\psi/\psi_\infty|^2 < 0.001$.

Figure 4.11 (b) shows how the crossing temperature T^* changes with $h^{\text{defect}}_{\text{penetration}}$. For a small $h^{\text{defect}}_{\text{penetration}}$, there is no crossing and hence $T^* = T_c^{P_{3f}}$. The crossing shows up when $h^{\text{defect}}_{\text{penetration}}$ is beyond a critical depth. As $h^{\text{defect}}_{\text{penetration}}$ becomes larger, the crossing effect becomes more significant (T^* becomes smaller, which means that the temperature window that a stronger rf field amplitude leads to a weaker P_{3f} becomes larger) and eventually tends to saturate.

The crossing effect can be understood as follows. In TDGL simulations, P_{3f} is collected at the rf dipole location, which is at $z = h_{dp}$ (above the sample surface). For a weak rf field amplitude, the rf vortex semi-loop in the grain boundary stays close to the sample surface ($z = 0$). As the rf field amplitude increases, the rf vortex semi-loop in the grain boundary is pushed toward the bottom of the grain boundary that it can penetrate ($z = -h^{\text{defect}}_{\text{penetration}}$)(A visualization of this effect is presented in Fig. 4.12.), which means that the rf vortex semi-loop is farther away from the rf dipole location ($z = h_{dp}$), and hence the P_{3f} collected at the rf dipole location becomes weaker. Such a phenomenon shows up only when the rf vortex semi-loop in the grain boundary can be pushed far away from the sample surface. For a small $h^{\text{defect}}_{\text{penetration}}$, the rf vortex semi-loop always stays just below the sample surface instead of penetrating deep into the sample, and hence P_{3f} does not decrease as the rf field amplitude increases (no crossing effect).

An rf vortex semi-loop is roughly parallel to the direction of the rf dipole, which points in the x-direction, and hence the cross-section of the rf vortex semi-loop is on the YZ plane. Figure 4.12 visualizes an rf vortex semi-loop in the grain boundary marked by the white dashed curve in Fig. 4.7 (b), with the vortex core corresponding to the black region, where $|\psi/\psi_\infty|^2 < 0.001$. The rf vortex semi-loop penetrates the sample surface and the vortex core is around 100.3 nm deep for $B_{pk} = 50.9$ mT (Fig. 4.12 (a)) and is around 110.9 nm deep for $B_{pk} = 56.6$ mT (Fig. 4.12 (b)).

Note that the results presented in Fig. 4.11 are obtained using the grain boundary model,

which is meant to be a phenomenological toy model. Therefore, the numerical values of $h^{\text{defect}}_{\text{penetration}}$ should not be interpreted literally. The key insight here is that there is no crossing effect for a small $h^{\text{defect}}_{\text{penetration}}$ (shallow penetration), and the crossing effect becomes apparent for a large $h^{\text{defect}}_{\text{penetration}}$ (deep penetration).

4.6 A Defect Model with Two Grain Boundaries

In the grain boundary model discussed in Sec. 4.3.4 and Sec. 4.5, there is only one single grain boundary beneath and roughly parallel to the rf dipole, and thus rf vortex semi-loops nucleate in one single grain boundary and $P_{3\text{f}}(T)$ shows a single-peak feature. Such a scenario corresponds to the case where the density of the sample grain boundaries that nucleates rf vortices (ρ^{defect}) is low. For a sample with a high density of grain boundaries that nucleates rf vortices, it can be modeled as a grain boundary model that contains two grain boundaries beneath and roughly parallel to the rf dipole.

Here we consider a grain boundary model that contains two grain boundaries that are near the origin and roughly parallel to the x-direction. The basic setting of the model is the same as described in Sec. 4.3.3. The only difference is how the Nb and the impurity phase are distributed horizontally, as shown in Fig. 4.13 (a). Figure 4.13 (a) shows the top view of the critical temperature distribution, and Fig. 4.13 (b) shows the TDGL simulation result of $P_{3\text{f}}(T)$ for this model.

The two-peak feature of $P_{3\text{f}}(T)$ in Fig. 4.13 (b) can be understood as follows. At low temperatures, the sample is in the Meissner state and $P_{3\text{f}}$ is weak. As temperature increases, around 4.50 K an rf vortex semi-loop nucleates in the top grain boundary and results in the lower

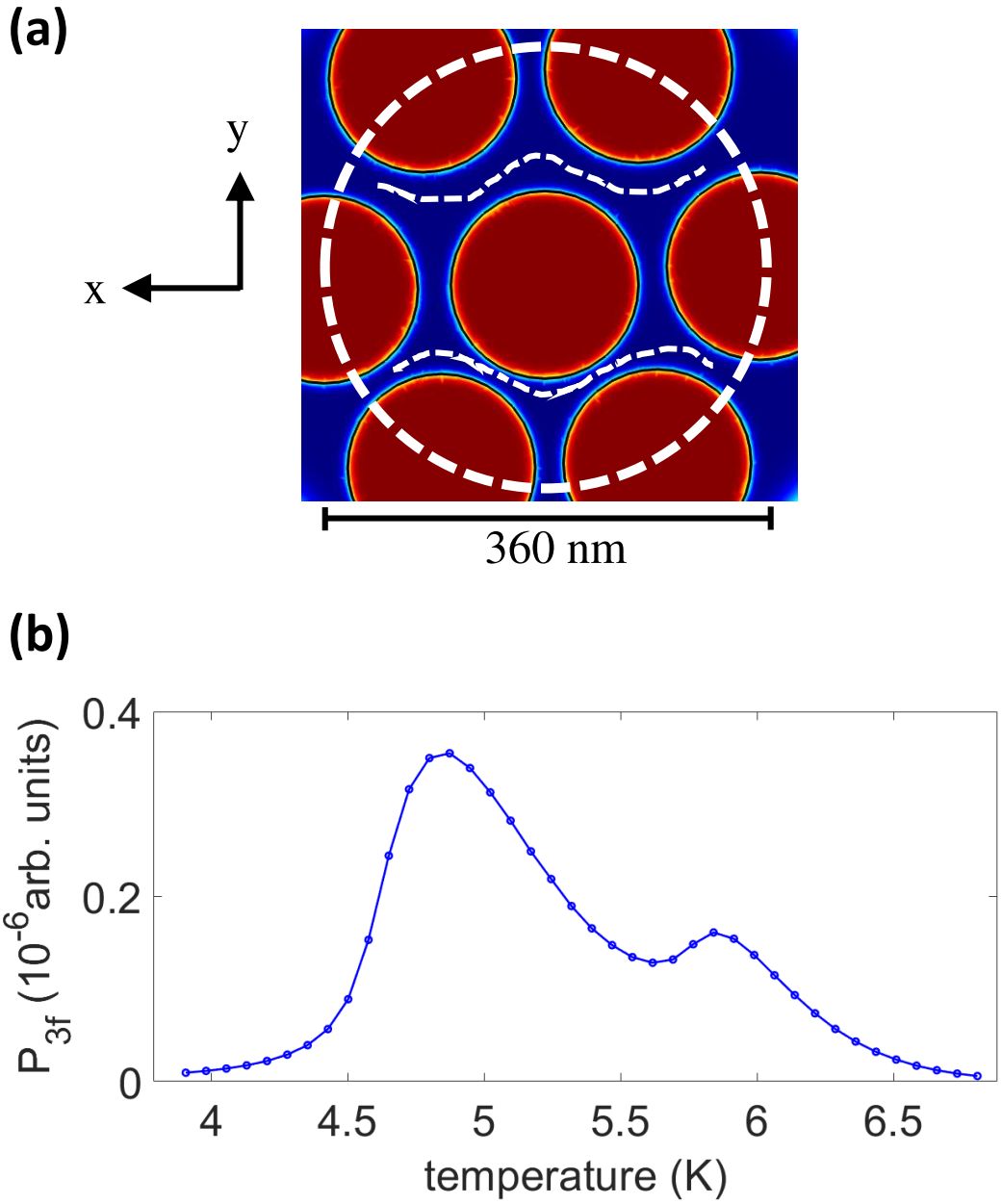

Figure 4.13: A grain boundary model containing two grain boundaries that are roughly parallel to the x-direction. (a) The distribution of critical temperature on the XY plane around the origin, with red being Nb and blue being the low-T_c impurity phase with $T_c^{\text{impurity}} = 3$ K. Here $(x, y, z) = (0, 0, 0)$ is at the center. The rf dipole is located at $(x, y, z) = (0, 0, 400\text{ nm})$, which is above the center of the image, and points in the x-direction. The two white dashed curves indicate the grain boundaries (the top grain boundary and the bottom grain boundary) that are roughly parallel to the x-direction. The model defect region is indicated by the white dashed circle. (b) TDGL simulation result of $P_{3f}(T)$ for the grain boundary model shown in (a). Here $h_{\text{penetration}}^{\text{defect}} = 280$ nm, and $B_{\text{pk}} = 50.9$ mT.

temperature peak, and then around 5.77 K another rf vortex semi-loop nucleates in the bottom grain boundary and results in the higher temperature peak. That is, rf vortex semi-loops nucleate in both grain boundaries and thus result in the two-peak feature of $P_{3\mathrm{f}}(T)$. The nucleation of the two rf vortex semi-loops is verified by monitoring $\Delta\theta/2\pi$ (the same analysis as shown in Fig. 4.4).

Chapter 5: Experimental Investigation of rf Vortex Nucleation in Nb/Cu Films

The studies presented in this chapter are published in Ref. [6].

5.1 Introduction to Superconducting Radio-Frequency Material Science

5.1.1 Introduction to Superconducting Radio-Frequency Cavities

In high-energy physics, there is continued interest in building next-generation particle accelerators (for example, the International Linear Collider, ILC) using bulk Nb superconducting radio-frequency (SRF) cavities [5, 99]. For the ILC, around 10000 SRF cavities will be built.

The quality of an SRF cavity is typically quantified by its quality factor (Q-factor) as a function of the accelerating gradient for the particle beam. Real-world materials are not perfect. The Q-factors of SRF cavities are usually below their theoretical predictions. In particular, as the accelerating gradient, and hence the rf magnetic field on the Nb surfaces, becomes strong, the Q-factor drops significantly (this is called the Q-slope) [100–103]. Such a Q-slope phenomenon limits the rf field supported by the SRF cavities, which then limits the performance of the particle accelerator. Besides the Q-slope phenomenon, quenches are also frequently observed in many SRF cavities [104–106]. One reason for a quench is that a superconductor is locally heated up to exceed its critical temperature and loses superconductivity. Both the Q-slope and defect-nucleated

quenches indicate that the performance of SRF cavities is limited by breakdown events below the theoretically predicted intrinsic critical field of the superconductor [5,101,102]. These breakdowns are sometimes caused by uncontrolled local defects [95, 107, 108]. Candidates of defects in SRF cavities include oxides [87–91], impurities [109,110], grain boundaries [81,96,111–115], dislocations [96,116,117], surface roughness [82,118], etc. To make high Q-factor SRF cavities that operate to high accelerating gradients, it is necessary to understand these defects, in particular their influence on the rf properties of SRF cavities. Therefore, there is a need to understand in detail the rf properties of these local defects.

5.1.2 Characterization Techniques for SRF Materials

In SRF material science, various kinds of techniques have been developed to characterize SRF cavities and SRF materials. For example, researchers routinely measure the Q-factor [119] and residual resistance [120] of SRF cavities. However, it is costly and time-consuming to fabricate and measure an entire cavity. As a result, many measurements are performed on coupon samples of SRF materials, including measurements of rf quench field [106,121,122] and surface resistance [121–124].

Another quantity of interest is the vortex penetration field because SRF cavities are expected to operate best in the Meissner state (vortex-free) to avoid dissipation due to vortex motion [81,106,118,125,126]. Superconductors show strong nonlinearity in the presence of vortices and show relatively weak nonlinearity in the vortex-free Meissner state. The nonlinear electrodynamic response arises when properties of the superconductor (such as the superfluid density) become time-dependent during the rf cycle. One manifestation of nonlinearity is that the superconductor creates

response currents to the stimulation at frequencies other than the driving frequency. Utilizing the connection between vortices and nonlinearity, the vortex penetration field can be determined by measuring the third-harmonic response of a superconductor subjected to a time-harmonic magnetic field [127]. In particular, the vortex penetration field of thin films and multilayer structures have been studied with such alternating current (AC) (kHz regime) third-harmonic response magnetometry [126, 128–134].

5.1.3 Near-Field Magnetic Microwave Microscopy for Local rf Characterization

The techniques described above (Q-factor, residual resistance, rf quench field, surface resistance, vortex penetration field, etc.) help physicists to characterize the global properties of SRF materials. However, none of them can directly study the local rf properties of SRF materials.

Motivated by the need to study rf properties of local defects, members of the Anlage lab successfully built and operated near-field magnetic microwave microscopes using a scanned loop (the original version) [8, 9, 23–25] as well as a magnetic writer from a magnetic recording hard-disk drive (the microwave microscope adopted in this work) [10, 11, 27–30] to measure locally-generated third-harmonic response (see Chapter 2). The spatial resolution of the local probe of the microwave microscope ranges from sub-micron to micron scale, and the excitation frequency is in the range of several GHz. The near-field magnetic microwave microscope used in this study is detailed in Chapter 2.

Our microwave microscope offers a complementary view of the material properties that limit SRF cavity performance. The quantities of interest in a finished SRF accelerator cavity are the quality factor Q, the surface resistance of the material making up the walls of the cavity, and

the changes in Q as the accelerating gradient of the cavity is increased. It is desirable to maintain a high Q-factor up to the point where the superconductor reaches its critical surface magnetic field. Our microscope measures local electrodynamic properties of small samples of materials that make up SRF cavities. It utilizes nonlinear response that results from strong and inhomogeneously imposed rf magnetic fields as a surrogate for the high-gradient conditions experienced by the materials inside an SRF cavity. The microscope applies surface magnetic fields quite different from those in an SRF cavity, and imposes unique electromagnetic stresses to the material under study. Note that the ohmic losses of superconducting materials in the microwave range at temperatures substantially below T_c are well below the sensitivity limit of any existing microwave microscope, hence these properties are not studied.

5.1.4 Nb/Cu Films as an Alternative to Bulk Nb for SRF Applications

Bulk Nb is the standard choice for fabricating SRF cavities. The main reason is that Nb has the highest critical temperature ($T_c = 9.3$ K) and the highest first critical field ($B_{c1} = 180$ mT) of all the elemental metals at ambient pressure. Besides bulk Nb, there are some candidate alternative materials for SRF applications [85], including Nb film on Cu [109, 118, 123, 125, 135–139], Nb_3Sn on bulk Nb substrate [81, 106, 115, 140–143], multilayer structure (superconductor-insulator-superconductor structures, for instance) [82, 103, 126, 128, 144–146], etc. The potential benefits of using materials other than bulk Nb would be a higher T_c and a potentially higher critical field B_c. In this work, we focus on Nb films on Cu.

The development of the deposition of Nb films onto Cu cavities has a long history [147]. In particular, the first Nb/Cu cavities were produced at CERN in the early 1980s [148]. Motivations

for Nb thin film technology for SRF applications include reducing material cost (high purity Nb costs around 40 times more than Cu) and better thermal stability. In particular, at frequencies around 300 to 400 MHz, Nb/Cu cavities allow operation at 4 K instead of 2 K, due to the superior thermal conductivity of Cu. The performance of bulk Nb cavities is approaching the intrinsic limit of the material. On the contrary, Nb/Cu cavities typically suffer from serious Q-slope problems [149,150], which limits their use in high accelerating fields. Solving the Q-slope problem in Nb/Cu cavities is essential for making them competitive for use in high-field accelerators.

5.2 Overview of the Chapter

In this work, we use our near-field magnetic microwave microscope (see Chapter 2) to study the local third-harmonic response P_{3f} of SRF-quality Nb/Cu films produced at CERN. These Nb/Cu films are provided by our collaborators at CERN: Carlota Pereira, Stewart Leith, and Guillaume Rosaz. Our objective is not to provide a comprehensive characterization of all types of surface defects present in these Nb/Cu films. Surface defects that do not nucleate rf vortices fall outside the scope of this study. Instead, our focus is on locally measuring the third-harmonic response to explore the surface defects that do nucleate rf vortices. Specifically, we aim to extract the properties of rf vortices linked to surface defects through experiments and simulations investigating the third-harmonic response and its dependence on temperature and rf field amplitude. Subsequently, we conduct a qualitative comparison of these Nb/Cu films based on our findings. This allows us to identify the Nb/Cu film that is most effective at reducing the nucleation of rf vortices associated with surface defects.

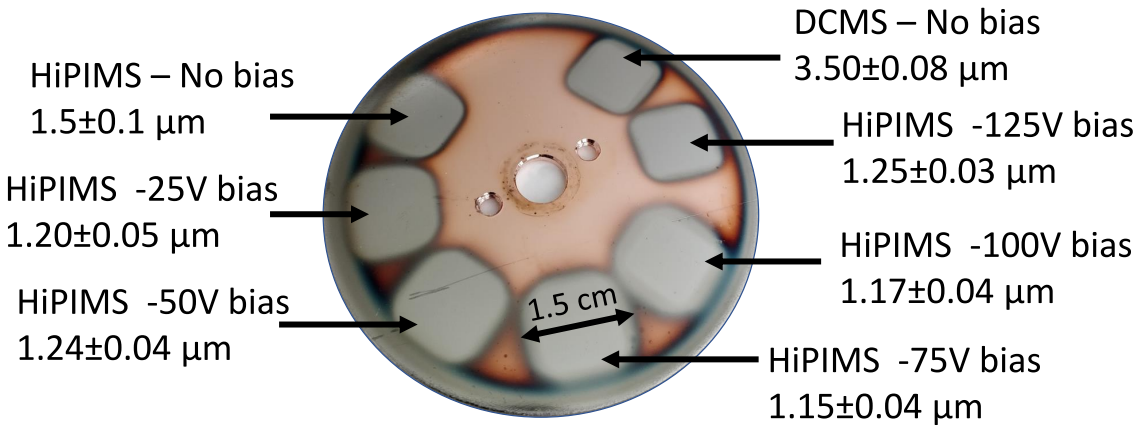

Figure 5.1: Photo of the seven Nb films on one common Cu substrate. The samples are prepared at CERN.

5.3 Outline of the Chapter

The outline of this chapter is as follows: In Sec. 5.4, we present how the seven Nb/Cu films studied in this work are prepared. In Sec. 5.5, we present the experimental results for the Nb/Cu films, focusing on surface defect signals, and interpret the results with the insights from TDGL simulations discussed in Chapter 4. In Sec. 5.6, we summarize the experimental results for the Nb/Cu films. In Sec. 5.7, leveraging the insights from TDGL simulations discussed in Chapter 4, we compare the Nb/Cu films to determine which deposition conditions most effectively suppress rf vortex nucleation at surface defects. In Sec. 5.8, we compare the key differences between a previous research conducted in the Anlage lab and the present study. In Sec. 5.9, we summarize our findings on the Nb/Cu films and discuss their implications for SRF applications.

Parameter	HiPIMS	DCMS
Average power (kW)	1.3	1.3
Discharge voltage (V)	-600	-377
Current (A)	160 (Peak current)	3.4
Working gas	Kr	Kr
Pressure (mbar)	$2.3 \cdot 10^{-3}$	$2.3 \cdot 10^{-3}$
Temperature (^{0}C)	150	150
Coating duration (min)	60	60

Table 5.1: Sample preparation parameters of the seven Nb/Cu films studied in this work.

5.4 Sample Information

In this work, we study seven Nb films deposited on one common Cu substrate [138, 139], as shown in Fig. 5.1. One of the samples is prepared by Direct Current Magnetron Sputtering (DCMS) with zero bias, and the sample thickness is around 3.5 μm. The other six samples are prepared by High Power Impulse Magnetron Sputtering (HiPIMS) [151], with bias from 0 V to 125 V, and the sample thickness ranges from 1.15 μm to 1.5 μm.

In these six HiPIMS samples, the primary variable under investigation is the applied bias voltage during deposition (described later in this section). While the film thicknesses vary slightly, they are not systematically controlled or varied. Therefore, the analysis in this work focuses on the influence of bias voltage, rather than film thickness [151], on the properties of the deposited Nb/Cu films.

The HiPIMS Nb/Cu films studied in this thesis were fabricated using the same deposition methods as the HiPIMS + BS films described in Ref. [123], which provides a detailed analysis of the resulting microstructures. Figure 3(a) of Ref. [123] presents a scanning electron microscopy (SEM) image of the surface of a HiPIMS Nb/Cu film, while Figure 4(a) shows an SEM image of a focused ion-beam (FIB) prepared cross-section of the same film. The average grain size at

the top layer surface is approximately 390 nm. According to Table 2 in Ref. [123], the crystallite size—estimated from x-ray diffraction (XRD) analysis—is about 91 nm, and the dislocation density is approximately 2.7×10^{14} m^{-2}.

The preparation of the seven Nb/Cu films studied in this thesis is discussed in the following. The substrate used for the Nb coatings is a 2 mm thick, oxygen-free electronic (OFE) copper disk measuring 75 mm in diameter. Prior to coating, the substrate disk is degreased using commercial detergent. The sample is then chemically polished using a mixture of sulfamic acid (H_3NSO_3, 5 g/L), hydrogen peroxide (H_2O_2, 5% vol.), n-butanol (5% vol.) and ammonium citrate (1 g/L) heated up at 72^0C for 20 minutes. After polishing, the disk is rinsed with sulfamic acid to remove the build-up of native oxide and cleaned with de-ionized water and ultra-pure ethanol.

The Cu substrate is mounted on an ultra-high vacuum (UHV) stainless steel chamber equipped with a rotatable shutter to expose in turn the areas to be coated, and the chamber is then connected to a sputtering system. Both assemblies are performed inside an ISO5 cleanroom, and the sputtering apparatus is described in detail in Ref. [138]. The entire system is transported to the coating bench where it is coupled to the pumping group and gas injection lines, and pumped down to about 1×10^{-7} mbar. The pumping group and the sputtering system undergo a 48-hour bakeout at 200^0C, during which a 4-hour activation of the Non-Evaporable Getter (NEG) pump is performed. The temperature of the UHV chamber is maintained at 150^0C until the start of the coating. After cooling down, the system reaches a base pressure around 9.3×10^{-10} mbar. Ultra-pure krypton (99.998%) is injected into the system until a process pressure of 2.3×10^{-3} mbar is reached. The seven coatings are then performed according to the deposition parameters outlined in Table 5.1. One of the samples is prepared by Direct Current Magnetron Sputtering (DCMS) with zero bias, and the coating thickness is around 3.5 μm. The other six samples are

prepared by High Power Impulse Magnetron Sputtering (HiPIMS), with bias voltages ranging from 0 V to -125 V, with coating thicknesses ranging from 1.15 μm to 1.5 μm.

During the coating process, the sample temperature was monitored with an infrared thermal sensor (OMEGA OS100-SOFT) and kept constant at 150^0C. The HiPIMS plasma discharge was maintained using a pulsed power supply (Huettinger TruPlasma HighPulse 4006) and the negative bias voltage was applied to the samples using a DC power supply (TruPlasma Bias 3018). The DCMS discharge was maintained using a Huettinger Truplasma 3005 power supply. The discharge and bias voltages and currents were monitored throughout the entire coating process using voltage (Tektronix P6015A) and current (Pearson current monitor 301×) probes whose signals are recorded by a digital oscilloscope (Picoscope 2000). After the coating, the samples were cooled down to room temperature, after which the chamber was vented with dry air. The Nb layer thickness is measured by X-ray fluorescence via the attenuation method.

5.5 Experimental Results with Insights from TDGL Simulations

Previous research conducted in the Anlage lab [11] investigated the third-harmonic response of several bulk Nb samples and Nb/Cu films using the same experimental setup as in this study. However, maintaining a consistent probe-sample separation proved challenging due to the non-flat surfaces of the samples, which provided motivation for the samples created for the present work. In contrast, the Nb/Cu films examined in this study exhibit remarkable flatness, ensuring consistent probe-sample separation. Furthermore, HiPIMS Nb/Cu cavities fabricated at CERN show high repeatability [152], and the HiPIMS Nb/Cu films examined in this study adopt the same fabrication recipe. These two features enable us to conduct more meaningful comparisons between these

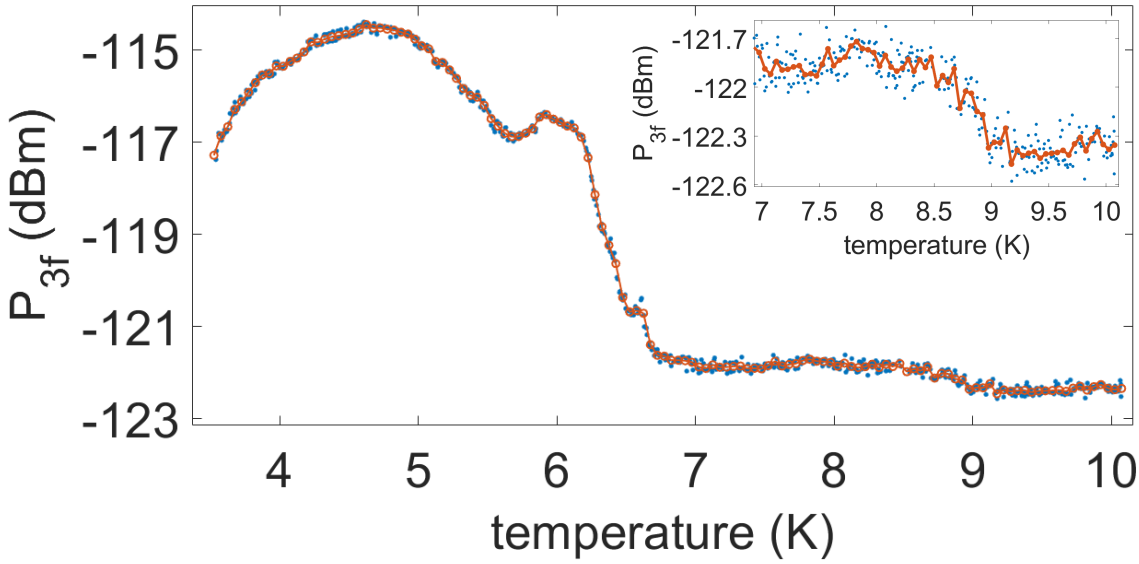

Figure 5.2: Representative data for P_{3f} as a function of temperature for the HiPIMS 25 V bias Nb/Cu sample. The input frequency is 1.86 GHz and the input power is 2 dBm. The blue dots are the raw data, and the red curve is the P_{3f} averaged over 0.05 K range bins. Inset: enlargement of the figure above 7 K.

samples.

In the following, we present a detailed discussion of the HiPIMS 25 V bias Nb/Cu sample in Sec. 5.5.1 as a representative example of the typical measured P_{3f} response, while the results for the other six Nb/Cu samples are provided in Sec. 5.5.2.

5.5.1 Measurement Results for the HiPIMS 25 V Bias Nb/Cu Sample

5.5.1.1 Fixed Location Measurements

Figure 5.2 shows the representative data for the third-harmonic response power P_{3f} as a function of temperature at a fixed location on the HiPIMS 25 V bias Nb/Cu sample. A representative measurement protocol is as follows. The sample is warmed up to 10 K (above T_c), and then the microwave source is turned on with fixed input frequency ($f = \omega/2\pi$=1.86 GHz)

and input power ($P_{\rm rf}$=+2 dBm), and then $P_{3\rm f}$ is measured as the sample is gradually cooled down to 3.5 K. In other words, the surface of the sample experiences a fixed rf field $B_{\rm rf}\sin(\omega t)$ in a sub-micron scale area during the cooldown process from 10 K to 3.5 K.

The measured $P_{3\rm f}(T)$ in Fig. 5.2 can be decomposed into three segments: the region above 9.1 K, the region below 6.7 K, and the region in between. The magnetic writer head (the probe of our microwave microscope) itself has temperature-independent nonlinearity. The signal above 9.1 K comes from this probe background and is indeed temperature-independent. A transition around 9.1 K can be seen in the inset of Fig. 5.2. This transition comes from the intrinsic nonlinear response of the Nb film. The strongest $P_{3\rm f}$ signal here shows up below 6.7 K. In the following, such a $P_{3\rm f}$ onset temperature is called the $P_{3\rm f}$ transition temperature and is denoted as $T_{\rm c}^{\rm P_{3f}}$. Compared to the signal around 9.1 K, the onset around 6.7 K is dramatic. Such a signal suggests that some mechanism shows up at and below 6.7 K that produces strong nonlinearity. The mechanisms leading to strong $P_{3\rm f}$ below 6.7 K are extrinsic and are likely due to surface defects. Note that $P_{3\rm f}$ below 6.7 K is much stronger than the intrinsic Nb signal around 9.1 K, suggesting that our local $P_{3\rm f}$ measurement is sensitive to surface defects.

Since the main objective of this work is investigating rf properties of surface defects, the strong $P_{3\rm f}$ below 6.7 K is the main focus in the following.

To further study the nature of $P_{3\rm f}$ below 6.7 K, $P_{3\rm f}(T)$ for various input powers $P_{\rm rf}$ (and hence various applied rf field amplitudes $B_{\rm rf}$) are measured. For each measurement, the sample is warmed up to 10 K and then cooled down to 3.5 K while experiencing an applied rf field with fixed input frequency and input power. Since the measured $P_{3\rm f}$ is the combination of probe background and sample contribution, the probe background (probe background is obtained by averaging the magnitude of $P_{3\rm f}(T)$ between 9.5 K and 10 K) is subtracted from the total signal to isolate the

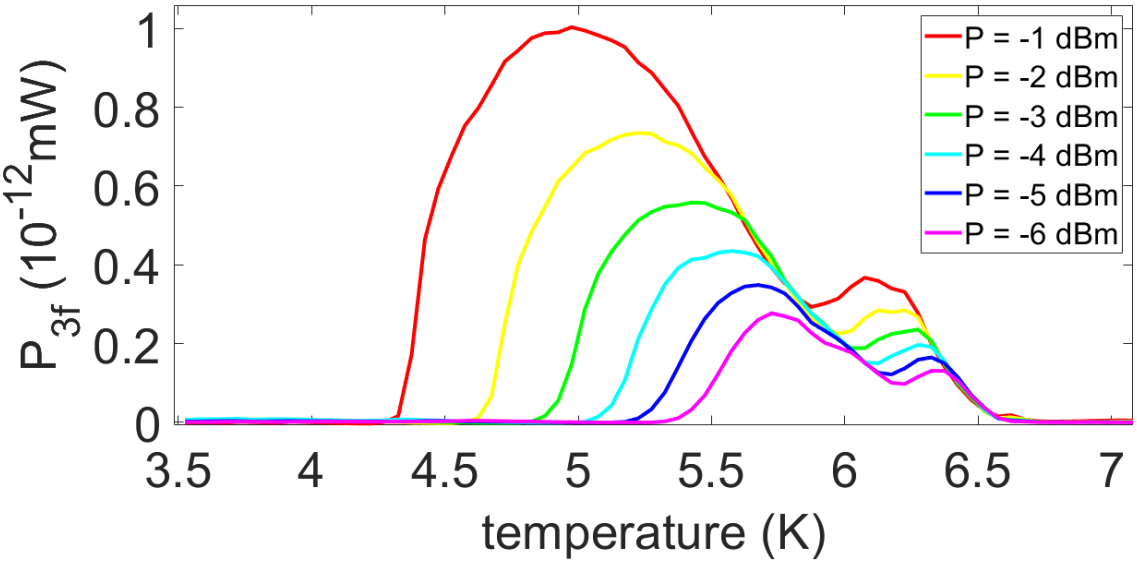

Figure 5.3: Measured linear power scale $P_{3f}(T)$ from strong (red) to weak (purple) input power for the HiPIMS 25 V bias Nb/Cu sample. The input frequency is 1.86 GHz. Compared to the raw data shown in Fig. 5.2, here the probe background is subtracted. Note that input power (in dBm scale) is proportional to B_{rf}^2, and hence $B_{rf}^{red} = 1.78\ B_{rf}^{purple}$.

sample signal. The process is repeated six times, each time with a different input power. The results of the six $P_{3f}(T)$ of different input powers (and hence different B_{rf}) are shown in the linear format in Fig. 5.3.

In Fig. 5.3, all the six $P_{3f}(T)$ exhibit a two-peak feature, and their $T_c^{P_{3f}}$ are consistently around 6.7 K. For both peaks, as the rf field amplitude increases (purple to red in Fig. 5.3), the $P_{3f}(T)$ maximum increases; in addition, the $P_{3f}(T)$ maximum and the $P_{3f}(T)$ low-temperature onset both show up at a lower temperature.

5.5.1.2 Consistent Features in Experiment and TDGL Simulations

The characteristic feature that "P_{3f} at low temperatures is significantly stronger than the intrinsic Nb signal around T_c^{Nb}" appears in both Fig. 5.2 (measurement) and Fig. 4.9 (TDGL

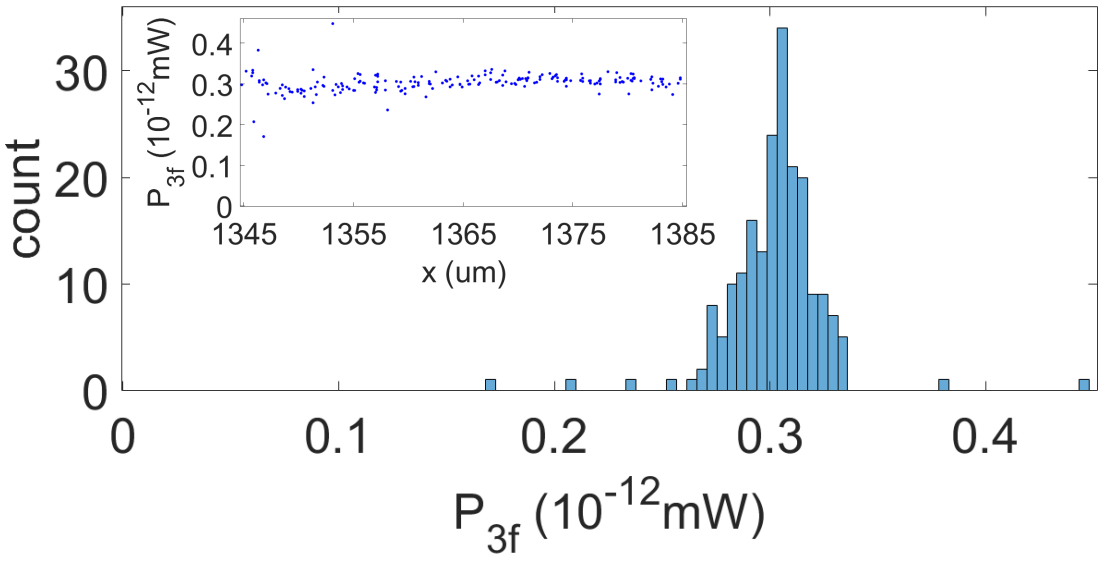

Figure 5.4: Statistics of one-dimensional scan for $P_{3f}(T = 5.7 \quad \text{K}, \quad P = -5 \quad \text{dBm}, \quad f = 1.86 \quad \text{GHz})$ for the HiPIMS 25 V bias Nb/Cu sample. The coefficient of variation (the ratio of the standard deviation to the mean) is 0.08. Inset: spatial distribution of this one-dimensional scan.

simulation). The two-peak feature of the $P_{3f}(T)$ in Fig. 5.3 (measurement) is also observed in Fig. 4.13 (b) (TDGL simulation). Furthermore, both peaks of $P_{3f}(T)$ in Fig. 5.3 (measurement) exhibit all four key features identified in Sec. 4.4 (TDGL simulation), which are intrinsic signatures of rf vortex nucleation by surface defects. The consistency between experimental observations and TDGL simulations strongly suggests that the strong P_{3f} signals observed in Fig. 5.2 and Fig. 5.3 may be attributed to rf vortex semi-loops nucleated by surface defects.

5.5.1.3 Scanning Measurements

So far the measurements are taken at one single location on the surface of the sample. How about the situation at other locations? In particular, does the defect signal (the strong P_{3f} below 6.7 K) show up at other locations as well? To answer this question, we measure $P_{3f}(T)$ with P = -2 dBm at four distinct locations on the sample surface and obtain consistent results. The

separation between any two of these locations exceeds 10 μm. In addition, a one-dimensional (1D) scan is performed for a 40 μm range with a step size of 0.2 μm. Temperature and input power are chosen to be T = 5.7 K and P = -5 dBm, and our goal is to determine the homogeneity of the signal from the lower temperature peak of the blue curve in Fig. 5.3. The 1D scan result is shown in Fig. 5.4. According to this scanning result, the P_{3f} signal from the defect is quite consistent and uniform at the μm-scale (coefficient of variation = 0.08). One possible explanation of such uniformity is that the size of one single defect is at the nm-scale and the defect spacing is smaller than the resolution of the microscope (sub-micron scale), and hence the P_{3f} signal of our sub-micron scale measurements comes from the contributions of multiple defects. As an example, the average grain size is around 390 nm for the HiPIMS Nb/Cu films studied in Ref. [123] (page 3 of Ref. [123]). Suppose the HiPIMS Nb/Cu films studied in this work have a similar structure to those in Ref. [123], and suppose the surface defects responsible for the P_{3f} signal in Fig. 5.4 are grain boundaries. In that case, a microwave microscope with a resolution significantly better than 400 nm is required to resolve P_{3f} signals from two distinct grain boundaries.

5.5.2 Measurement Results for Six Nb/Cu Samples

So far, only the HiPIMS 25 V bias Nb/Cu sample has been discussed. Temperature dependence and input power dependence of P_{3f} are studied for the other six Nb/Cu samples in the same manner as the HiPIMS 25 V bias Nb/Cu sample.

Figure 5.5 shows the representative $P_{3f}(T)$ for the 75 V bias sample (Fig. 5.5 (a)) and the 125 V bias sample (Fig. 5.5 (b)). For both Fig. 5.5 (a) and (b), $P_{3f}(T)$ exhibits the first three of the four key features identified in Sec. 4.4 (TDGL simulation), suggesting that these features are quite

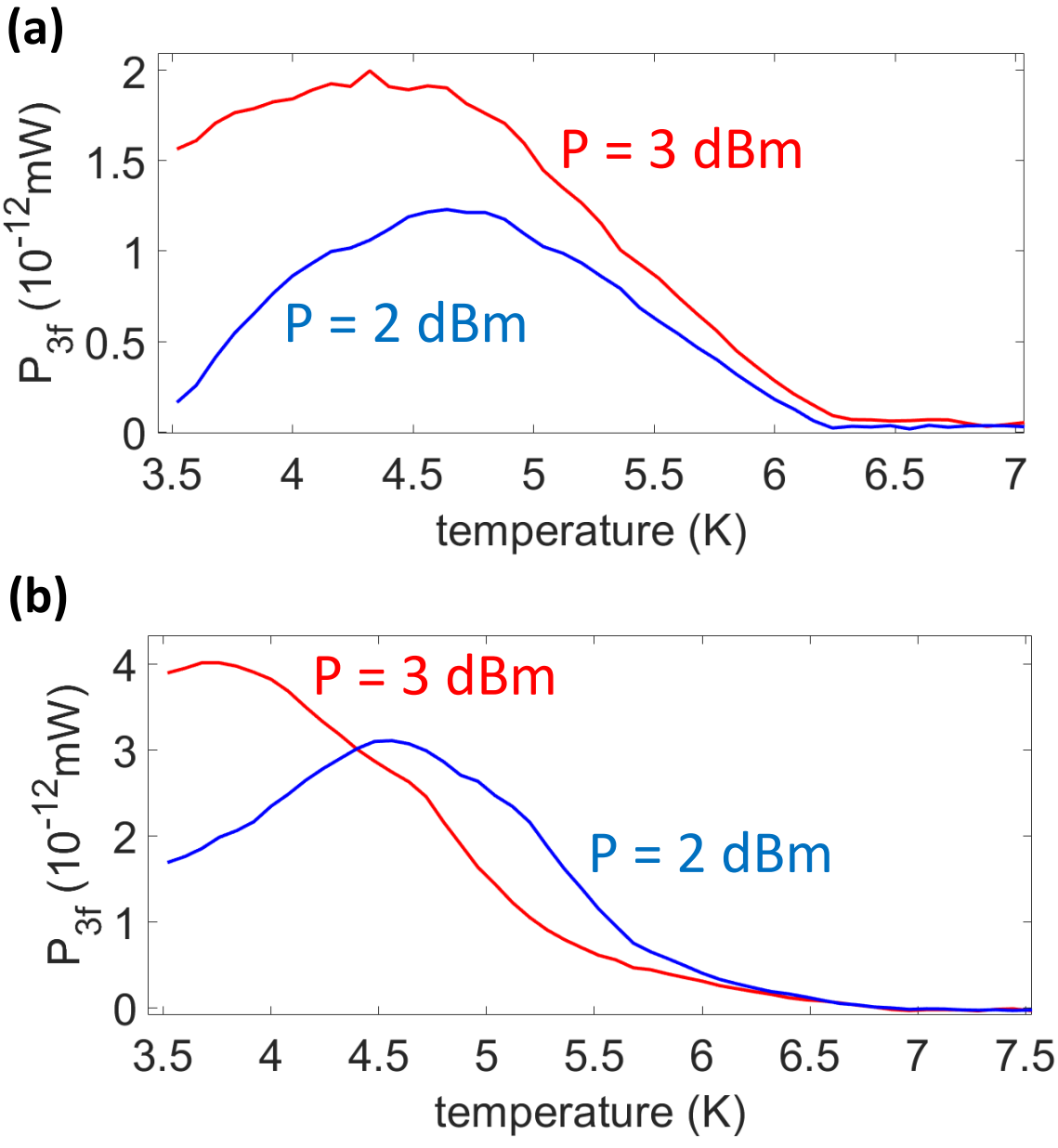

Figure 5.5: Measured $P_{3f}(T)$ for two input powers for (a) the HiPIMS 75 V bias Nb/Cu sample with an input frequency of 1.98 GHz and for (b) the HiPIMS 125 V bias Nb/Cu sample with an input frequency of 1.66 GHz.

universal. Although the temperature regime below 3.5 K is inaccessible in our measurements, the fourth key feature from Sec. 4.4 (TDGL simulation) is likely present for the HiPIMS 75 V bias Nb/Cu sample and the HiPIMS 125 V bias Nb/Cu sample, as inferred from the behavior of $P_{3f}(T)$ above 3.5 K in Fig. 5.5.

The fact that experimental data (Fig. 5.3 and Fig. 5.5) and TDGL simulation of the grain boundary model (Fig. 4.10) both exhibit the four key features (Sec. 4.4) and a $T_c^{P_{3f}}$ below 9.3 K suggests that "rf vortex semi-loops nucleate in grain boundaries hosting low-T_c impurity phases" is indeed one of the possible mechanisms of the observed P_{3f} signals for the HiPIMS Nb/Cu samples.

Figure 5.6 shows the representative data for $P_{3f}(T)$ generated by surface defects for the HiPIMS 50 V bias sample, the HiPIMS 100 V bias sample, and the DCMS sample. For the HiPIMS 50 V bias sample, $P_{3f}(T)$ with $T_c^{P_{3f}}$ around 6.4 K is observed in a strong input power regime (Fig. 5.6 (a)), and $P_{3f}(T)$ with $T_c^{P_{3f}}$ around 6.8 K is observed in a weak input power regime (Fig. 5.6 (b)). For the HiPIMS 100 V bias sample, $P_{3f}(T)$ with $T_c^{P_{3f}}$ around 6.5 K is observed (Fig. 5.6 (c)). For the DCMS sample, $P_{3f}(T)$ with $T_c^{P_{3f}}$ around 6.5 K is observed (Fig. 5.6 (d)). The negative value for $T < 6.5$ K in Fig. 5.6 (d) is due to the naive background subtraction, as discussed in Sec. 2.4.7.

Figure 5.7 shows the representative data for $P_{3f}(T)$ of the HiPIMS 0 V bias Nb/Cu sample. For this sample, $P_{3f}(T)$ shows a clear transition around 9 K. In addition to the intrinsic Nb response, $P_{3f}(T)$ demonstrates a non-trivial temperature dependence around 7.6 K and 6.5 K, indicating the presence of surface defects.

The surface defect signal of the HiPIMS 0 V bias Nb/Cu sample differs qualitatively from all other samples examined in this work in two key aspects. First, while $P_{3f}(T)$ exhibits a bell-shaped

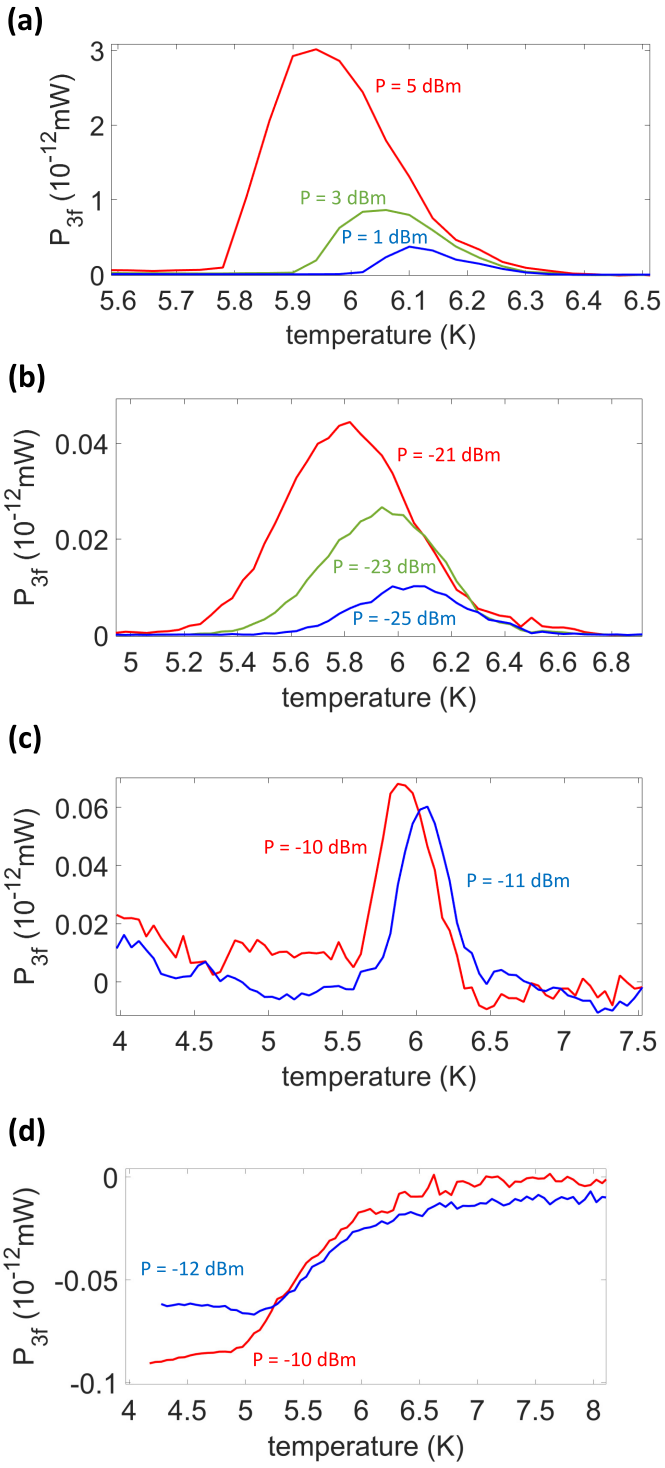

Figure 5.6: (a) and (b) show $P_{3f}(T)$ for the HiPIMS 50 V bias Nb/Cu sample with an input frequency of 2.16 GHz in a strong input power regime and in a weak input power regime, respectively. (c) shows $P_{3f}(T)$ for the HiPIMS 100 V bias Nb/Cu sample with an input frequency of 1.18 GHz. (d) shows $P_{3f}(T)$ for the DCMS Nb/Cu sample with an input frequency of 1.22 GHz.

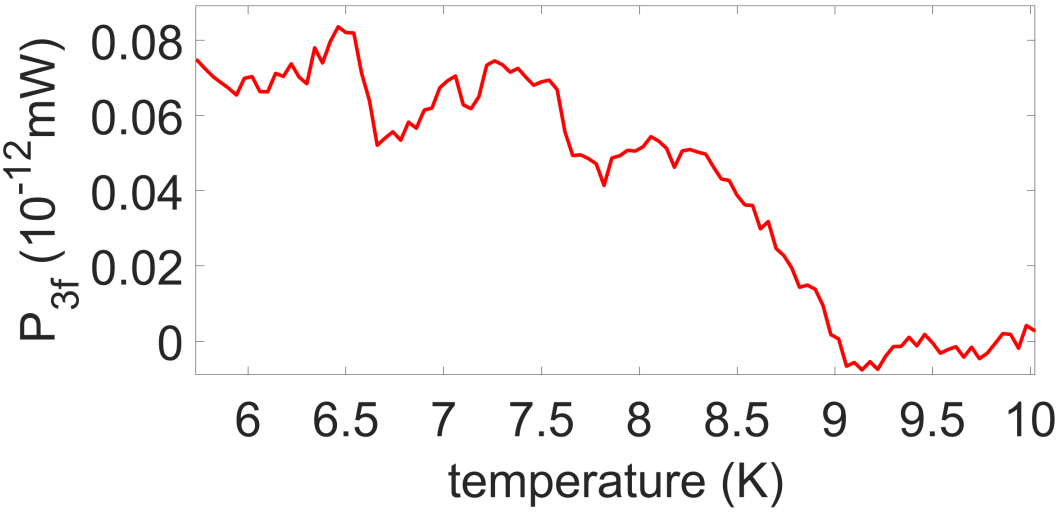

Figure 5.7: Measured $P_{3f}(T)$ for the HiPIMS 0 V bias Nb/Cu sample. The input frequency is 1.98 GHz and the input power is 3 dBm.

structure in all other samples (see Fig. 5.3, Fig. 5.5, and Fig. 5.6), this characteristic behavior is absent in the HiPIMS 0 V bias sample. Second, in all other samples that display both intrinsic and defect-related responses, the surface defect signal is significantly stronger than the intrinsic Nb response (see Fig. 5.2).

These observations suggest that the HiPIMS 0 V bias Nb/Cu sample likely exhibits a distinct mechanism for generating nonlinearity, differing from those observed in the other six samples. Notably, when deposited on complex-shaped substrates, the HiPIMS 0 V samples show significant porosity inside the film, which is quite different from all other HiPIMS films at non-zero bias [138]. This porosity may give rise to a qualitatively different type of nonlinear response, which is beyond the scope of the present work.

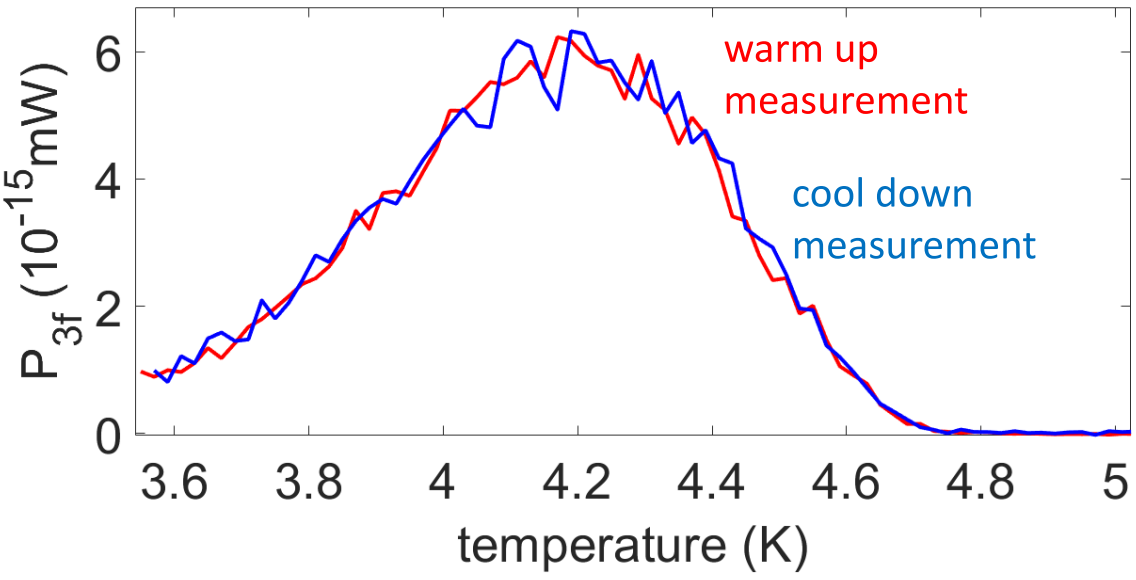

Figure 5.8: Check for hysteresis in $P_{3f}(T)$ measurement for the HiPIMS 125 V bias Nb/Cu sample. The input frequency is 1.88 GHz and the input power is -25 dBm.

5.5.3 No Evidence of Trapped Vortices Affecting Measurements

For all the $P_{3f}(T)$ measurements discussed in this chapter, $P_{3f}(T)$ is measured as a function of decreasing temperature starting above T_c (from 10 K to 3.5 K). One may wonder whether this procedure produces trapped vortices when a Nb film cools down through its T_c. To address this issue, we consider the effects of the two magnetic fields involved: the residual DC field and the applied rf field. The average flux quanta separation ($\sqrt{\Phi_0/B}$) corresponding to the residual DC field near the sample (around 35 μT) is around 7.7 μm, which is much larger than the spatial resolution of the microscope (sub-micron scale). Therefore, with high probability, there is no DC flux beneath the microscope probe, even if the 35 μT residual DC field is completely trapped. Regarding the rf field, the rf vortices are transient, appearing and disappearing twice per rf cycle. Compared to the dynamics of an rf vortex (on the order of nanoseconds), the temperature change

during a typical cool-down is in the extreme adiabatic limit. To the best of our knowledge, there is no unambiguous evidence suggesting that an rf vortex can be converted to a DC vortex and trapped as a Nb film cools down through T_{c}.

One way to verify whether rf vortices are trapped in our setup is to compare $P_{3\mathrm{f}}(T)$ measured during a warm-up process to $P_{3\mathrm{f}}(T)$ measured during a cool-down process for a sample exhibiting a defect signal, and check for the presence of hysteresis. Here, we examine the HiPIMS 125 V bias Nb/Cu sample.

The sample is first cooled from 10 K to 3.6 K in the absence of an rf field. The microwave signal is then turned on after the temperature stabilizes at 3.6 K. Subsequently, the sample undergoes a gradual warm-up from 3.6 K to 10 K (warm-up $P_{3\mathrm{f}}(T)$), followed by a cool-down from 10 K to 3.6 K (cool-down $P_{3\mathrm{f}}(T)$), with the microwave signal applied throughout this process.

As shown in Fig. 5.8, the $P_{3\mathrm{f}}(T)$ measurements do not exhibit a clear hysteresis, supporting our interpretation that no trapped DC vortices are formed as the Nb film cools through T_{c} in the presence of an rf field.

The measurement of Fig. 5.8 is performed one year and a half after the measurement of Fig. 5.5 (b). It is quite likely that different regions of the sample surface are studied in these two measurements. This might explain why Fig. 5.8 ($T_{\mathrm{c}}^{\mathrm{P}_{3\mathrm{f}}}$=4.8 K) and Fig. 5.5 (b) ($T_{\mathrm{c}}^{\mathrm{P}_{3\mathrm{f}}}$=6.8 K) show different $P_{3\mathrm{f}}$ signals.

Sample	Fixed-point measurement	Scanning
HiPIMS, 125V bias	$T_c^{P_{3f}}$=6.8 K defect is everywhere	
HiPIMS, 100V bias	Nb signal around 8.8 K $T_c^{P_{3f}}$=6.5 K defect	N/A
HiPIMS, 75V bias	$T_c^{P_{3f}}$=6.3 K defect	N/A
HiPIMS, 50V bias	Nb signal around 8.9 K $T_c^{P_{3f}}$=6.4 K defect is everywhere $T_c^{P_{3f}}$=6.8 K defect is everywhere	
HiPIMS, 25V bias	Nb signal around 9.1 K two of $T_c^{P_{3f}}$=6.7 K defects are everywhere	
HiPIMS, no bias	Nb signal around 9 K defect signal	N/A
DCMS, no bias	$T_c^{P_{3f}}$=6.5 K defect	N/A

Table 5.2: Summary of the defect signal (red) and the Nb signal (blue) of the seven Nb/Cu samples.

5.6 Summary of the Seven Nb/Cu Samples

The results of the defect signal and the Nb signal of all seven Nb/Cu samples are summarized in Table 5.2. For the six HiPIMS Nb/Cu samples, it is quite universal that P_{3f} measurements reveal the intrinsic Nb signal around 9 K and the extrinsic defect signal at low temperatures. Specifically, the defect signal with $T_c^{P_{3f}}$ between 6.3 K and 6.8 K is observed for five out of the six HiPIMS Nb/Cu samples, suggesting that such a defect is a generic feature for these HiPIMS Nb/Cu samples. (Here, we exclude the HiPIMS 0 V bias Nb/Cu sample, since it exhibits a distinct mechanism for generating nonlinearity.) Moreover, the defect signals are always much stronger than the intrinsic Nb signal around 9 K, like the situation shown in Fig. 5.2. Scanning measurements are performed for three HiPIMS samples (25 V bias sample, 50 V bias sample, and 125 V bias sample), and the results show that the defect signals are quite uniform at the μm-scale for all three samples. It is worth noting that the third-harmonic response of a Nb/Cu film in a previous research of the Anlage lab [11] also revealed surface defects, with $T_c^{P_{3f}}$ around 6.76 K (see TABLE I of [11]).

Sample	ρ^{defect}	$h^{\text{defect}}_{\text{penetration}}$
HiPIMS, 125V bias	low	deep
HiPIMS, 100V bias	low	deep
HiPIMS, 75V bias	low	shallow
HiPIMS, 50V bias	high	shallow
HiPIMS, 25V bias	high	shallow
HiPIMS, no bias	N/A	
DCMS, no bias	N/A	

Table 5.3: Comparison of the seven Nb/Cu samples. The second column shows qualitative assignments of the density of surface defects that nucleate rf vortex semi-loops (ρ^{defect}) and the third column shows qualitative assignments of how deep an rf vortex semi-loop penetrates into a sample through a surface defect ($h^{\text{defect}}_{\text{penetration}}$).

5.7 Comparison of the Seven Nb/Cu Samples: Suppression of rf Vortex Nucleation

Larger values of $P_{3\text{f}}$ are closely related to the presence of rf vortex semi-loops. By studying $P_{3\text{f}}$, we investigate surface defects that nucleate rf vortex semi-loops, which are the kinds of surface defects that are directly relevant to the rf performance of SRF cavities. Throughout the following discussion, surface defects specifically refer to those capable of nucleating rf vortex semi-loops.

Equipped with the insights from TDGL simulations discussed in Chapter 4, the measured $P_{3\text{f}}$ can be analyzed further.

First, the number of peaks in $P_{3\text{f}}(T)$ can be correlated with the density of surface defects (ρ^{defect}), as demonstrated by the comparison between Sec. 4.3.4 and Sec. 4.6. A single-peak structure in $P_{3\text{f}}(T)$ corresponds to a low density of surface defects (see Sec. 4.3.4), whereas a two-peak structure indicates a higher defect density (see Sec. 4.6). In some Nb/Cu samples (75 V bias, 100 V bias, and 125 V bias), the $P_{3\text{f}}(T)$ defect signal exhibits a single-peak structure (see Fig. 5.5 and Fig. 5.6 (c)), suggesting that only one dominant defect signal is captured. In contrast,

$P_{3f}(T)$ of the HiPIMS 25 V bias Nb/Cu sample shows a two-peak feature (see Fig. 5.3), indicating that the measured $P_{3f}(T)$ results from the superposition of two defect signals.

Second, the "crossing" in $P_{3f}(T)$ can be linked to the depth of rf vortex semi-loop penetration into the sample through a surface defect ($h^{\text{defect}}_{\text{penetration}}$), as discussed in Sec. 4.5. The absence of the crossing effect corresponds to a small $h^{\text{defect}}_{\text{penetration}}$ (shallow), and the presence of the crossing effect corresponds to a large $h^{\text{defect}}_{\text{penetration}}$ (deep).

The data in Fig. 5.5 (a) closely resembles the simulation result in Fig. 4.11 (a), where a stronger rf field amplitude consistently enhances P_{3f} across all temperatures, showing no crossing effect. Conversely, the data in Fig. 5.5 (b) aligns with the simulation result in Fig. 4.10, exhibiting a "crossing effect": at temperatures near $T_c^{P_{3f}}$, a stronger rf field amplitude leads to a weaker P_{3f} (the red curve falls below the blue curve).

The assignment of qualitative surface defect properties of all seven Nb/Cu samples is summarized in Table 5.3. The second column shows an estimate for the density of surface defects that nucleate rf vortex semi-loops (ρ^{defect}) and the third column shows how deep an rf vortex semi-loop penetrates into a sample through a surface defect ($h^{\text{defect}}_{\text{penetration}}$). rf vortex penetration through surface defects is one of the main enemies of SRF applications. To achieve good SRF performance, the surface defect density should be low and the defect should be shallow. From the perspective of these two properties, among the five HiPIMS Nb/Cu samples with non-zero voltage bias, the HiPIMS 75 V bias Nb/Cu sample is the most effective in reducing the nucleation of rf vortices associated with surface defects.

In the numerical simulations in Chapter 4, surface defects that nucleate rf vortex semi-loops are modeled as grain boundaries. Since P_{3f} is associated with the behavior of rf vortex semi-loops, it is likely that the ideas of ρ^{defect} and $h^{\text{defect}}_{\text{penetration}}$ could apply to surface defects other than grain

boundaries (dislocations, for example).

For the DCMS sample, the actual P_{3f} value of the sample response remains unknown due to interference with the background signal and the lack of relative phase information (see Fig. 5.6 (d)). Consequently, the TDGL simulation results cannot be directly applied to the experimental data of the DCMS sample.

5.8 Comparison with Previous Research

Previous research conducted in the Anlage lab [11] investigated the third-harmonic response of several bulk Nb samples and Nb/Cu films using the same experimental setup as in this study. Here, we briefly compare the key differences between Ref. [11] and the present study.

In terms of simulations, Ref. [11] employs a hybrid approach: the third-harmonic response from surface defects is analyzed using the Josephson junction model, a circuit-based framework, while the response from rf vortex semi-loop nucleation in defect-free Nb is studied using TDGL simulations. In contrast, the present work applies the TDGL framework to analyze *both* surface defects and Nb (see Chapter 4), providing a unified theoretical approach.

On the experimental side, the periodic feature observed in Ref. [11]—explained by the Josephson junction model—is absent in the Nb/Cu films studied in this work. This suggests that the surface defects in the older-generation samples might differ from those in the new-generation samples. Consequently, rather than employing the Josephson junction model, we explore a different surface defect model in this work, namely the grain boundary model (see Sec. 4.3).

5.9 Conclusion

In this work, we study seven Nb/Cu films that are candidates for SRF applications. Local P_{3f} measurements reveal surface defects with P_{3f} onset temperatures between 6.3 K and 6.8 K for five out of the six HiPIMS Nb/Cu samples, indicating that such defects are a generic feature of these air-exposed HiPIMS Nb/Cu films. The signal from the low-T_c surface defect is much stronger than the intrinsic Nb response around 9 K, suggesting that our local P_{3f} measurement is sensitive to surface defects. With the capability of μm-scale scanning, it is found that such a defect is quite uniform in space on the μm-scale.

TDGL simulations are performed (in Chapter 4) to further analyze the experimental results. In particular, the simulations indicate that two key properties—the density of surface defects that nucleate rf vortices and the depth to which rf vortices penetrate through these defects—can be qualitatively extracted from our local P_{3f} measurements. We find that these two phenomenological parameters vary systematically with film deposition conditions. From the point of view of these two properties, the HiPIMS 75 V bias Nb/Cu sample stands out as the most effective in reducing the nucleation of rf vortices associated with surface defects.

Chapter 6: TDGL Modeling of Trapped Vortex Dynamics and Second-Harmonic Response

The studies presented in this chapter are covered in Ref. [7].

6.1 Introduction

The dynamics of trapped DC vortices under stimulation by a localized rf magnetic field is a complex and rich topic. A comprehensive numerical investigation of this problem is beyond the scope of this work. Instead, this chapter focuses on illustrating key features of the second-harmonic response (P_{2f}) associated with trapped vortex dynamics using numerical simulations of simplified toy models (Niobium superconductor hosting vortex pinning sites). These simulations provide key insights into the underlying mechanisms of P_{2f}, which will later be used to interpret the experimental results presented in Chapter 7. The general framework for the TDGL simulations used in this study is described in Chapter 3.

Throughout this chapter, the term *trapped vortices* refers to trapped DC vortices.

To investigate the dynamics of trapped vortices, we first describe the incorporation of trapped vortices into our TDGL simulations (Sec. 6.2). We then discuss the fundamental mechanism responsible for the observed second-harmonic response (Sec. 6.3). Finally, we present three core features of P_{2f} using various toy models (Sec. 6.4, Sec. 6.5, and Sec. 6.6).

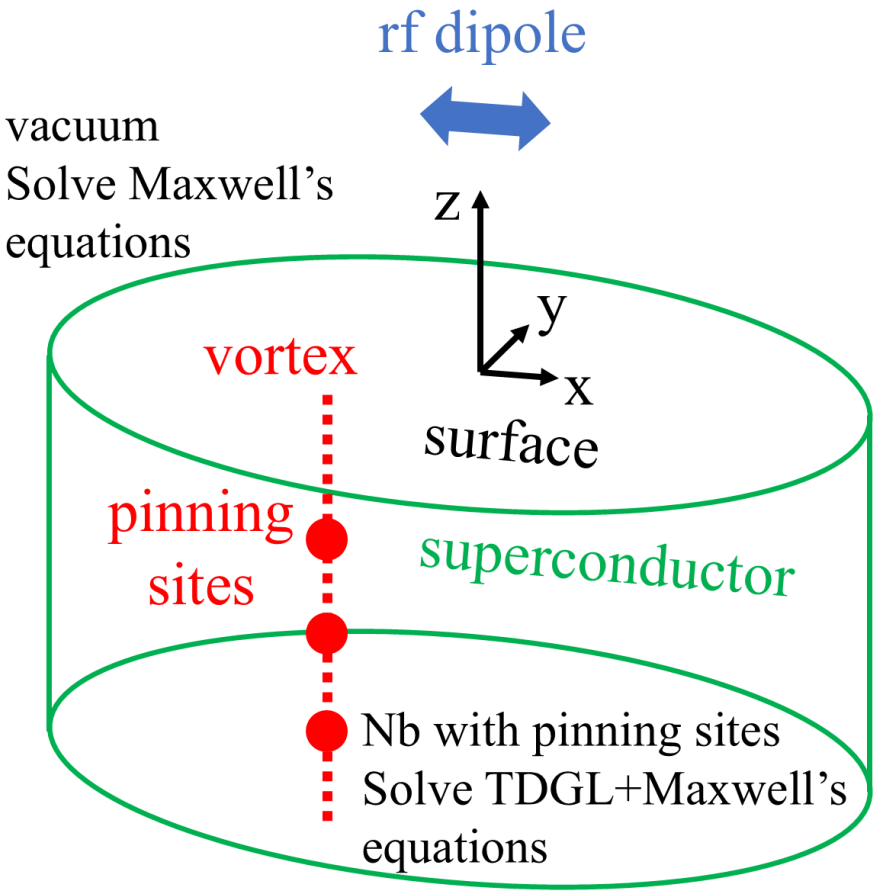

Figure 6.1: A schematic representation of the TDGL simulations and toy models. The blue double arrow represents the rf dipole, the red dots represent the pinning sites, and the red dashed line represents a trapped vortex.

6.2 Modeling Trapped DC Vortices in TDGL Simulations

The primary addition to the TDGL framework described in Chapter 3 is the inclusion of single-flux-quantum trapped magnetic vortices. Figure 6.1 provides a schematic representation of the TDGL simulations and toy models (Niobium superconductor hosting vortex pinning sites). In this schematic, there is one set of pinning sites and one trapped vortex pinned by the pinning sites.

In the toy models studied in this chapter, a pinning site is modeled as a spherical region of

toy model	x_{pin} (nm)	y_{pin} (nm)	r_{pin} (nm)
1	0	0	40
2	120	80	40
3	80 -80	80 -80	40 40
4	80 80	80 -80	40 40
5	120 40	80 -120	40 16
6	120 120	80 -80	40 18

Table 6.1: Summary of the pinning site configurations for toy models 1 to 6. Each toy model includes either one or two sets of pinning sites, with each set consisting of three identical pinning sites sharing the same $(x_{\text{pin}}, y_{\text{pin}})$ coordinates. The z_{pin} values for the three sites are -200 nm, -360 nm, and -520 nm.

radius r_{pin} composed of a low-T_{c} impurity phase. Pinning sites are incorporated by introducing spatial variations in five material-specific parameters, as discussed in Sec. 3.6.

The location of a pinning site is represented by $(x_{\text{pin}}, y_{\text{pin}}, z_{\text{pin}})$, where $z_{\text{pin}} < 0$ since the sample occupies the $z < 0$ region. Each toy model includes either one or two sets of pinning sites, with each set consisting of three identical pinning sites sharing the same $(x_{\text{pin}}, y_{\text{pin}})$ coordinates. The z_{pin} values for the three sites are -200 nm, -360 nm, and -520 nm. Each set of pinning sites can then be labeled by its x_{pin}, y_{pin}, and r_{pin}.

The specific pinning site configurations for the toy models studied in this chapter are summarized in Table 6.1.

To generate trapped vortices, a uniform DC magnetic field is applied along the z-direction. DC vortices aligned in the z-direction then nucleate at the boundary of the superconducting domain and propagate inward, spreading throughout the superconducting region. While most of these vortices remain unpinned and free to move, some become pinned at the pinning sites. Once these vortices are pinned, the external DC magnetic field is subsequently *removed*. The

unpinned vortices repel each other and eventually exit the simulation domain, leaving only the pinned vortices localized at the pinning sites (as illustrated in Fig. 6.1).

After the unpinned vortices have left the simulation domain, the rf magnetic field is applied for five rf cycles, and P_{2f} at the location of the dipole is calculated based on the vortex dynamics observed during the fifth rf cycle.

6.3 Origin of Second-Harmonic Response

6.3.1 Asymmetry in Vortex Dynamics and Second-Harmonic Response

As discussed in Sec. 1.4.4, when a system is driven by a sinusoidal driving force, the second-harmonic response quantitatively characterizes the *asymmetry* in the system dynamics between successive half-cycles.

In the context of this work, the system consists of trapped vortices in a superconductor, and the driving force is an oscillating magnetic field created by a scanned dipole over the surface of the superconductor. When trapped vortices are stimulated by this oscillating magnetic field, they wiggle in response, and the *asymmetry* component of this motion generates second-harmonic response.

6.3.2 Mechanism of Asymmetry in Trapped Vortex Dynamics

The asymmetry in time of trapped vortex dynamics can arise from various mechanisms. One such mechanism involves an asymmetric potential experienced by vortices, which may originate intrinsically in noncentrosymmetric superconductors [153, 154], be introduced through artificially engineered asymmetric potentials [155–158], or be created by the combination of a symmetric

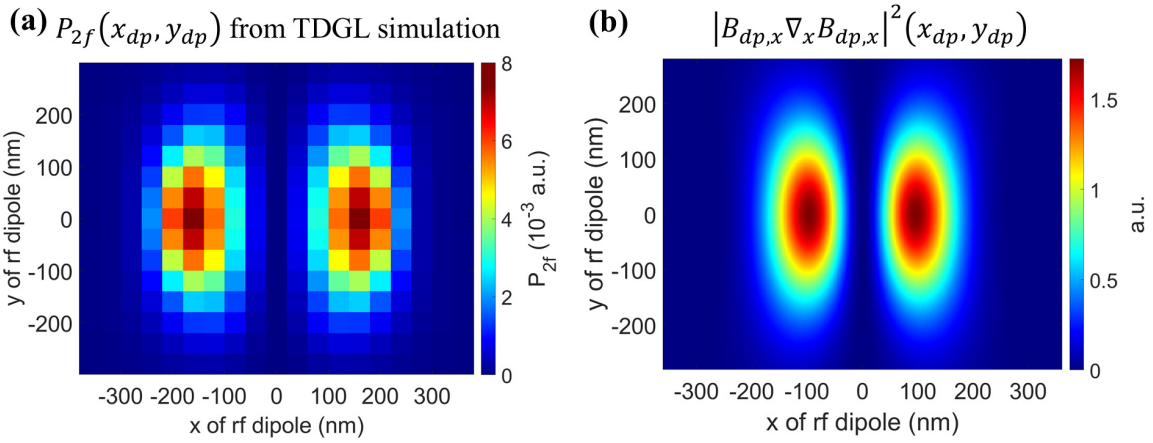

Figure 6.2: Asymmetry in time of the dynamics of a trapped vortex (at $(x, y) = (0, 0)$) as a function of dipole location $(x_{\mathrm{dp}}, y_{\mathrm{dp}})$, for $h_{\mathrm{dp}} = 400\,\mathrm{nm}$. (a) TDGL simulation results of $P_{2\mathrm{f}}$ as a function of dipole location $(x_{\mathrm{dp}}, y_{\mathrm{dp}})$ for toy model 1 (a vortex pinned at $(x, y) = (0, 0)$), at $T = 7.44$ K and $B_{\mathrm{pk}} = 28.3$ mT. (b) The plot of $|B_{\mathrm{dp,x}}\nabla_x B_{\mathrm{dp,x}}|^2$ at $(x, y) = (0, 0)$ as a function of dipole location $(x_{\mathrm{dp}}, y_{\mathrm{dp}})$, where $B_{\mathrm{dp,x}}$ is the x-component of the magnetic field at the surface of a superconductor created by a magnetic dipole.

pinning potential and a DC current acting as a bias [33, 156].

In our case, the asymmetry originates from the *localized* and *inhomogeneous* nature of the rf magnetic field, which is generated by the rf dipole in simulations and by the microscope probe in experiments. This rf magnetic field induces a screening current, which in turn generates a Lorentz force acting on trapped vortices [37, 38, 159, 160]. Due to the strong spatial gradient of the rf magnetic field, both the screening current and the resulting Lorentz force exhibit significant spatial gradients. During an rf cycle, a trapped vortex experiences a stronger Lorentz force when moving toward regions of higher magnetic field strength and a weaker force when moving away, resulting in asymmetric vortex dynamics between the two half-cycles.

6.3.3 Spatially Inhomogeneous rf Field and Asymmetric Vortex Dynamics

To further investigate the mechanism underlying the second-harmonic response in our system, it is insightful to consider the following question: For a vortex pinned at $(x, y) = (0, 0)$, how does its dynamics vary as a function of the dipole location $(x_{\mathrm{dp}}, y_{\mathrm{dp}})$, while keeping the dipole height h_{dp} fixed?

Figure 6.2 (a) presents TDGL simulation results for $P_{2\mathrm{f}}$ (recovered at the dipole location) as a function of $(x_{\mathrm{dp}}, y_{\mathrm{dp}})$, for a vortex pinned at $(x, y) = (0, 0)$ (toy model 1). This essentially represents the second-harmonic point-spread function of a single trapped DC vortex, as imaged by our near-field magnetic microwave microscope. The spatial pattern of $P_{2\mathrm{f}}(x, y)$ observed in Fig. 6.2 (a) can be understood as follows.

The Lorentz force F_{Lorentz} acting on a trapped vortex is proportional to the local current density J, which, to first-order approximation, is proportional to the magnitude of the magnetic field B_{total}. At the superconductor surface ($z = 0$), $B_{\mathrm{total}} = 2B_{\mathrm{external}}$ by considering the image method and the boundary condition that the perpendicular component of the magnetic field must vanish at $z = 0$. In other words, at $z = 0$, we have

$$F_{\mathrm{Lorentz}} \propto J \propto B_{\mathrm{total}} = 2B_{\mathrm{external}}. \tag{6.1}$$

In our case, B_{external} is the external magnetic field at $z = 0$ created by the rf dipole.

Since the rf dipole is oriented in the x-direction, the induced current is primarily in the y-direction, creating a Lorentz force on the vortex in the x-direction, and the motion of the trapped vortex is predominantly along the x-axis. Roughly speaking, the asymmetry in the vortex motion

is proportional to both the strength of the Lorentz force exerted on the vortex by J_{y} and its spatial gradient at $z = 0$. Consequently, an estimate of $P_{2\mathrm{f}}$ at the surface of the superconductor is given by

$$P_{2\mathrm{f}}(x_{\mathrm{dp}}, y_{\mathrm{dp}}) \propto \left| J_{\mathrm{y}} \nabla_x J_{\mathrm{y}} \right|^2 \propto \left| B_{\mathrm{dp,x}} \nabla_x B_{\mathrm{dp,x}} \right|^2, \tag{6.2}$$

where $B_{\mathrm{dp,x}}$ is the x-component of the dipole magnetic field (B_{external} in this case) at $z = 0$.

The analytic expressions for $B_{\mathrm{dp,x}}$ is given by

$$B_{\mathrm{dp,x}}(x, y) = \frac{\mu_0 M}{4\pi} \frac{3(x - x_{\mathrm{dp}})^2 - r^2}{r^5}, \tag{6.3}$$

where M is the magnetic moment, and $r = \sqrt{(x - x_{\mathrm{dp}})^2 + (y - y_{\mathrm{dp}})^2 + h_{\mathrm{dp}}^2}$. For $B_{\mathrm{dp,x}} \nabla_x B_{\mathrm{dp,x}}$, we have

$$\begin{aligned} B_{\mathrm{dp,x}} \nabla_x B_{\mathrm{dp,x}} = &\left(\frac{\mu_0 M}{4\pi} \right)^2 \frac{3(x - x_{\mathrm{dp}})^2 - r^2}{r^{12}} \\ &\times 3(x - x_{\mathrm{dp}}) \left[3r^2 - 5(x - x_{\mathrm{dp}})^2 \right]. \end{aligned} \tag{6.4}$$

Figure 6.2 (b) presents $\left| B_{\mathrm{dp,x}} \nabla_x B_{\mathrm{dp,x}} \right|^2$ experienced at $(x, y) = (0, 0)$ as a function of scanned dipole location $(x_{\mathrm{dp}}, y_{\mathrm{dp}})$. The strong similarity between Fig. 6.2 (a) and Fig. 6.2 (b) supports the qualitative validity of Eq. 6.2. A key feature shared by both figures is that the asymmetry vanishes along the entire y-axis ($x_{\mathrm{dp}} = 0$). In Fig. 6.2 (b), this occurs because $\nabla_x B_{\mathrm{dp,x}} = 0$. In Fig. 6.2 (a), the system exhibits symmetry between the $-x$ and $+x$ directions, leading to symmetric vortex dynamics between the two half-cycles, which results in $P_{2\mathrm{f}} = 0$. Note that $P_{2\mathrm{f}} = 0$ when the dipole is positioned directly above the trapped vortex ($(x_{\mathrm{dp}}, y_{\mathrm{dp}}) = (0, 0)$) even though there is a significant Lorentz force acting on the vortex. Figure 6.2 (a) clearly

demonstrates that P_{2f} reflects the asymmetry of the vortex dynamics rather than simply indicating the presence of a trapped vortex right beneath the dipole. In the case of multiple trapped vortices, P_{2f} remains a measure of the asymmetry in their collective dynamics rather than being proportional to their number.

It is worth pointing out that the pinning potential in toy model 1 enjoys rotational symmetry about the z-axis. The asymmetry in the wiggling motion of the trapped vortex (except along the y-axis) originates from the strong gradient of the localized rf magnetic field itself at the vortex location rather than from any intrinsic asymmetry in the pinning potential. Consequently, this technique, measuring P_{2f} with our microwave microscope, remains effective even for trapped vortices in symmetric pinning potentials.

For the rest of the simulations in this chapter (toy models 2 to 6), the dipole is fixed at $(x_{dp}, y_{dp}, h_{dp}) = (0, 0, 400\,\mathrm{nm})$.

6.4 Trapped Vortices and P_{2f}

Core Feature 1: P_{2f} arises exclusively in the presence of trapped vortices and is absent when no trapped vortices are present.

Figure 6.3 shows $P_{2f}(T)$ for toy model 2 under two scenarios. In Case 1 (red curve), a single pinned vortex is present, while in Case 2 (blue curve), no pinned vortex is present. Both cases use identical conditions and pinning potentials, with the only difference being the presence or absence of a trapped vortex at the pinning sites. In Case 1, the wiggling of the trapped vortex generates P_{2f}. In Case 2, there is no trapped vortex, and hence $P_{2f} = 0$. The slight bump observed in the blue curve around 8.8 K is attributed to numerical errors (slight asymmetries in the computed response

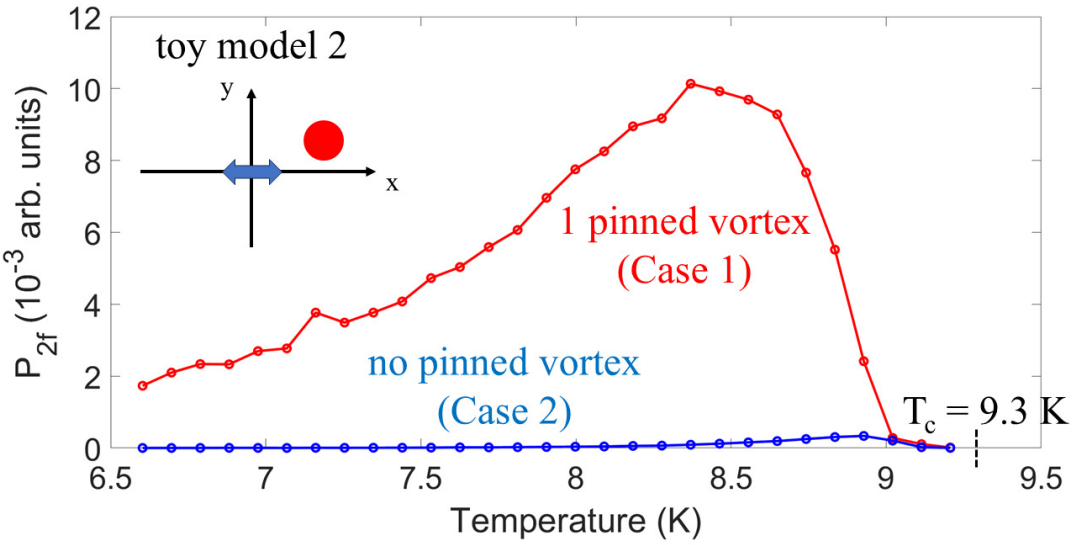

Figure 6.3: TDGL simulation results of $P_{2f}(T)$ ($B_{pk} = 28.3$ mT) for toy model 2 under two scenarios. There is one pinned vortex for the red curve (Case 1) and there is no pinned vortex for the blue curve (Case 2). The inset shows the top-view setup of toy model 2: The blue double arrows represent the rf dipole, and the red dot represents the vortex (Case 1) pinned by pinning sites.

between the two half-cycles).

6.5 Trapped Vortex Configuration and P_{2f}

Core Feature 2: P_{2f} is highly sensitive to the specific configuration of trapped vortices.

Figure 6.4 shows P_{2f} for toy models 3 and 4, both of which contain two trapped vortices. Despite this similarity, the values of P_{2f} differ dramatically. In fact, P_{2f} is expected to be zero for toy model 3, as the vortex dynamics is perfectly symmetric by design; the small nonzero value observed in simulations (noted on the Figure) arises from numerical errors. This comparison between toy models 3 and 4 highlights that P_{2f} can vary significantly with changes in the trapped vortex configuration. Since P_{2f} reflects the time-asymmetry in vortex dynamics, it is inherently

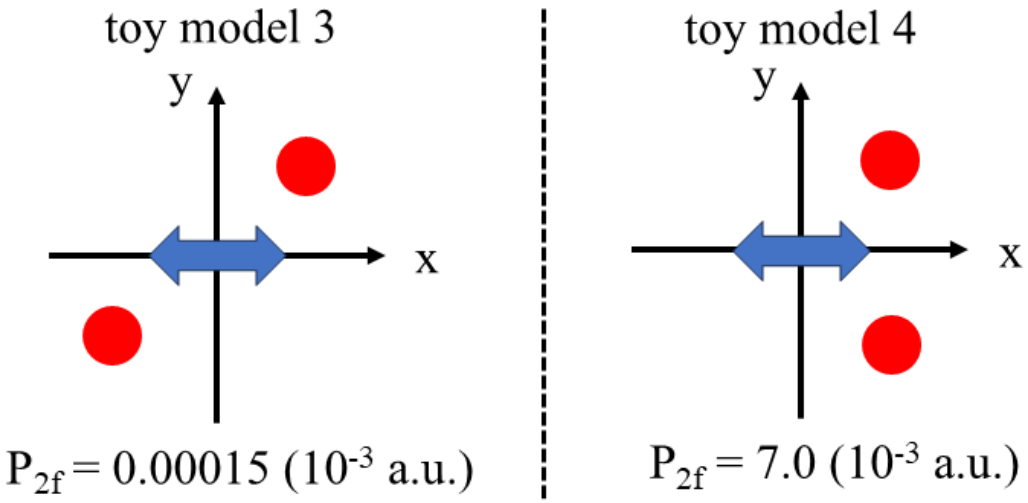

Figure 6.4: TDGL simulation results of P_{2f} for toy models 3 and 4, at $T = 7.44$ K and $B_{pk} = 28.3$ mT. The top-view shows a projection of the rf dipole (blue arrows) and the red dots represent vortices pinned by pinning sites.

sensitive to the detailed arrangement of trapped vortices.

6.6 Changes in Trapped Vortex Configuration

Core Feature 3: Changes in the trapped vortex configuration can cause abrupt jumps in $P_{2f}(T)$.

One manifestation of **Core Feature 2** is that vortex configuration changes as the temperature increases, which can result in a jump (up or down) in $P_{2f}(T)$. Figure 6.5 shows $P_{2f}(T)$ for toy model 5. At low temperatures (T<8.6 K), two vortices remain pinned. As the temperature increases beyond 8.6 K, one of the pinned vortices becomes depinned and escapes from the simulation due to the vortex-vortex repulsive force exceeding the pinning force provided by the pinning sites. This depinning event causes a dramatic jump in $P_{2f}(T)$ around 8.6 K, as shown in Fig. 6.5.

Since P_{2f} reflects the time-asymmetry in vortex dynamics rather than being proportional to the number of trapped vortices, its value can either increase or decrease when a pinned vortex is

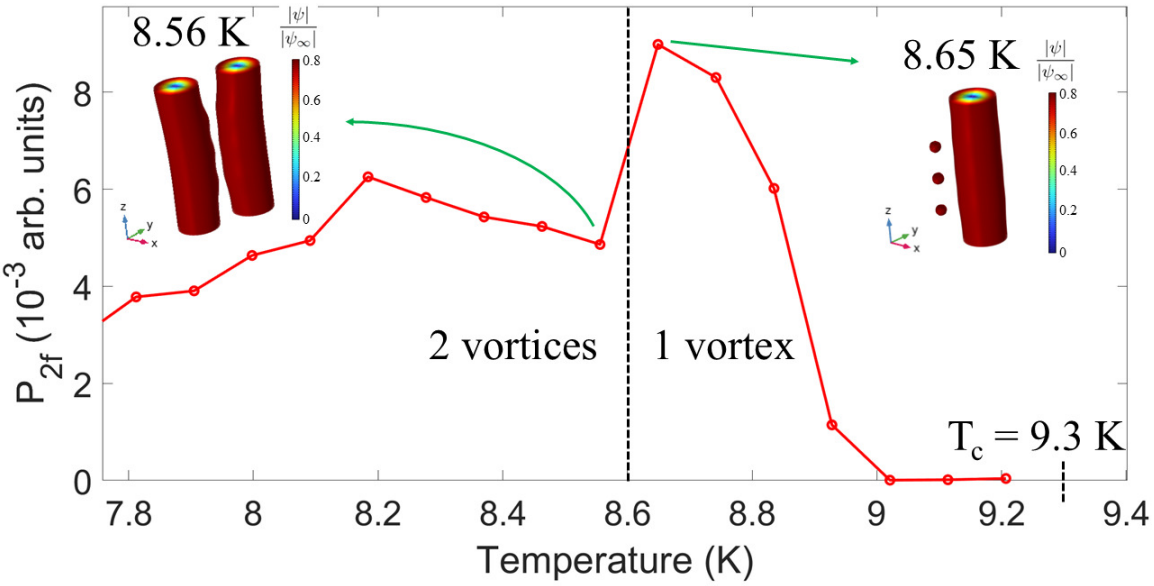

Figure 6.5: TDGL simulation results for $P_{2f}(T)$ for toy model 5 at $B_{pk} = 28.3$ mT. The two insets display the normalized order parameter (ψ/ψ_∞) at T=8.56 K and T=8.65 K, providing a visualization of the trapped vortices and pinning sites (red spheres).

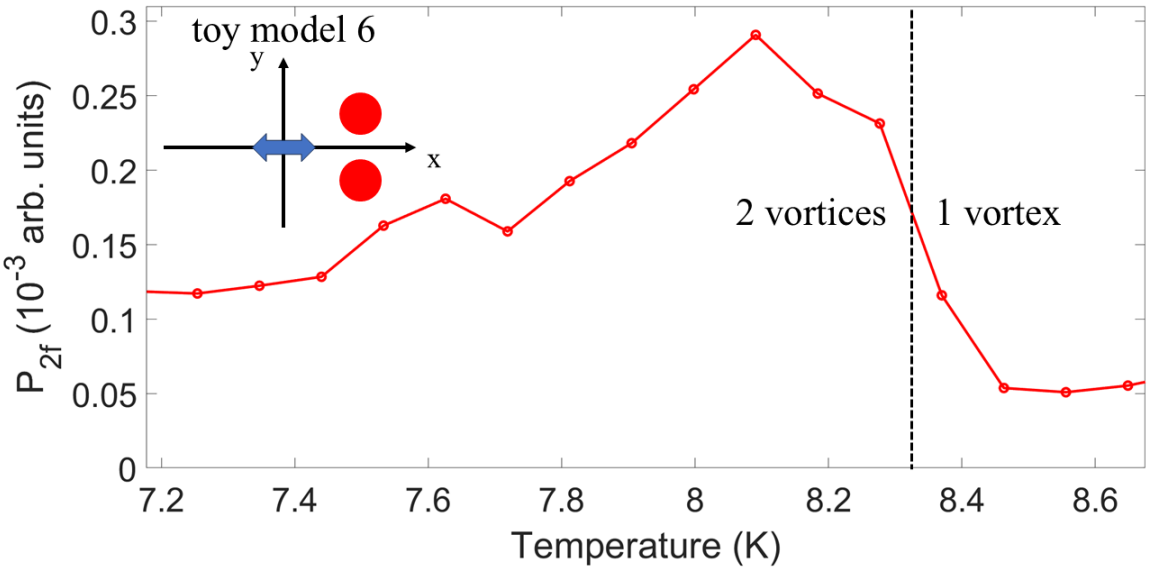

Figure 6.6: TDGL simulation results for $P_{2f}(T)$ for toy model 6 at $B_{pk} = 5.7$ mT. The blue double arrow represents the rf dipole, and the red dots represent vortices pinned by pinning sites.

removed. An example of $P_{2\mathrm{f}}(T)$ exhibiting a downward jump upon vortex depinning is provided in Fig. 6.6.

Figure 6.6 shows $P_{2\mathrm{f}}(T)$ for toy model 6. At low temperatures (T<8.32 K), two vortices remain pinned. As the temperature increases beyond 8.32 K, one of the pinned vortices becomes depinned and escapes from the simulation due to the vortex-vortex repulsive force exceeding the pinning force provided by the pinning sites. This depinning event causes a noticeable downward jump in $P_{2\mathrm{f}}(T)$ around 8.32 K, as shown in Fig. 6.6.

Chapter 7: Experimental Investigation of Trapped Vortex Dynamics in a Nb Film

The studies presented in this chapter are covered in Ref. [7].

7.1 Introduction to Trapped Vortices in Superconductors

7.1.1 Impact of Trapped Vortices in Superconducting Systems

Stray magnetic vortices that become pinned in superconductors contribute to enhanced losses in superconducting radio-frequency (SRF) cavities and corrupt the operation of superconducting electronics. In SRF cavities, trapped vortices introduce residual resistance, limiting the achievable quality factor [5, 81, 86, 161–172]. For superconducting quantum circuits, trapped vortices add loss [173–175], which serve to limit the coherence time of superconducting qubits operating at microwave frequencies. On the other hand, trapped vortices at current-nodes of a superconducting resonator can also be used to capture non-equilibrium quasiparticles and relax them [176]. For superconducting digital circuits, pinned vortices not only degrade performance but, in extreme cases, can compromise circuit functionality entirely [177–186].

The effects of trapped vortices in superconducting digital circuits are usually thought of in terms of DC bias currents that the vortices add to the circuits. However, in this work we investigate

an effect that has largely been overlooked in the context of superconducting digital circuits, namely the microwave frequency response of trapped vortices in superconductors.

7.1.2 Techniques for Studying Trapped Vortices

The behavior of trapped vortices under stimulation by an oscillating magnetic field [187] is often studied using macroscopic approaches that focus on the collective response of many trapped vortices. These studies typically measure average properties such as loss, critical current density, and pinning energy [33, 79, 188–193]. The results are generally interpreted in terms of collective single-coordinate models (e.g., Gittleman-Rosenblum type models) [37, 38, 159, 160, 194, 195], which describe the bulk response of vortices to rf currents rather than capturing the behavior of individual vortices. While these macroscopic techniques provide valuable insights into the average properties of all trapped vortices in a sample, they do not resolve the microscopic behavior of individual trapped vortices.

To gain a detailed understanding of vortex behavior, microscopic imaging techniques have been employed to directly study individual vortices in superconductors. Methods such as magnetic force microscopy (MFM) [196], scanning superconducting quantum interference device (SQUID) [197, 198], single-vortex confinement structures [199], scanning Hall probe microscopy [200], and scanning tunneling microscopy (STM) [201] have provided invaluable insights into vortex behavior. However, these techniques do not directly probe the high-frequency response of trapped vortices under an rf magnetic field, leaving a gap in our understanding of their microwave dynamics.

To address this gap, we employ a near-field magnetic microwave microscope to investigate

the high-frequency response of individual trapped vortices, as discussed in the next section.

7.2 Near-Field Magnetic Microwave Microscopy for Trapped Vortices

In this study, we introduce a near-field magnetic microwave microscope approach [6, 8–11, 23–25, 27–30, 67, 69] to study the dynamics of a limited number of trapped vortices under the probe (at micron length scales) by stimulating them with a localized and intense rf magnetic field and analyzing the second-harmonic response (P_{2f}) generated by their resulting motion. The near-field magnetic microwave microscope used in this study is detailed in Chapter 2.

The second-harmonic response has some subtleties associated with its interpretation. In Chapter 6, we show that the magnitude of the second-harmonic response is *not* directly proportional to the density of trapped vortices. Note that it is not our goal to measure the critical current density or the vortex depinning frequency (which is an effective macroscopic property of many vortices) associated with trapped vortices. Instead, P_{2f} is sensitive to a limited number of vortices and their detailed configuration and dynamics beneath the probe of our microwave microscope, and hence can be used to detect *changes in* trapped vortex configuration.

7.3 Overview of the Chapter

In this study, we experimentally investigate a Nb film with an antidot flux pinning array using our near-field magnetic microwave microscope. By measuring the local second-harmonic response (P_{2f}) at sub-femto-Watt levels, we isolate signals originating exclusively from trapped vortices, excluding contributions from surface defects and Meissner screening currents.

In Chapter 6, toy models of a Nb superconductor with trapped vortices are introduced and

studied using TDGL simulations of probe-sample interactions. As demonstrated in this chapter, the experimental results exhibit key features that align with the simulations.

This measurement technique provides access to vortex dynamics at the micron scale, such as depinning events of trapped vortices and spatially-resolved pinning properties, as demonstrated in measurements on the antidot Nb film.

7.4 Outline of the Chapter

The outline of this chapter is as follows: In Sec. 7.5, we present the Nb film with an antidot flux pinning array studied in this work. In Sec. 7.6, we present the experimental results for the antidot Nb film, and interpret the results with the insights from TDGL simulations discussed in Chapter 6. In Sec. 7.7, we extract vortex pinning properties from the experimental results. In Sec. 7.8, we summarize our findings on the antidot Nb film and discuss the capabilities of this measurement technique.

7.5 Sample Information

Antidot arrays in superconducting films serve as engineered traps for vortices [156–158, 189–192, 200, 202, 203]. In this work, we study a 170-nm-thick Nb film with an antidot flux pinning array on a SiOx substrate. The antidot array has a period of $1.6\,\mu$m and an antidot diameter of $1.2\,\mu$m. Figure 7.1 shows an atomic force microscopy (AFM) image of a $5 \times 5\,\mu\mathrm{m}^2$ surface area of the sample. Note that the substrate is exposed in the antidot regions of the film.

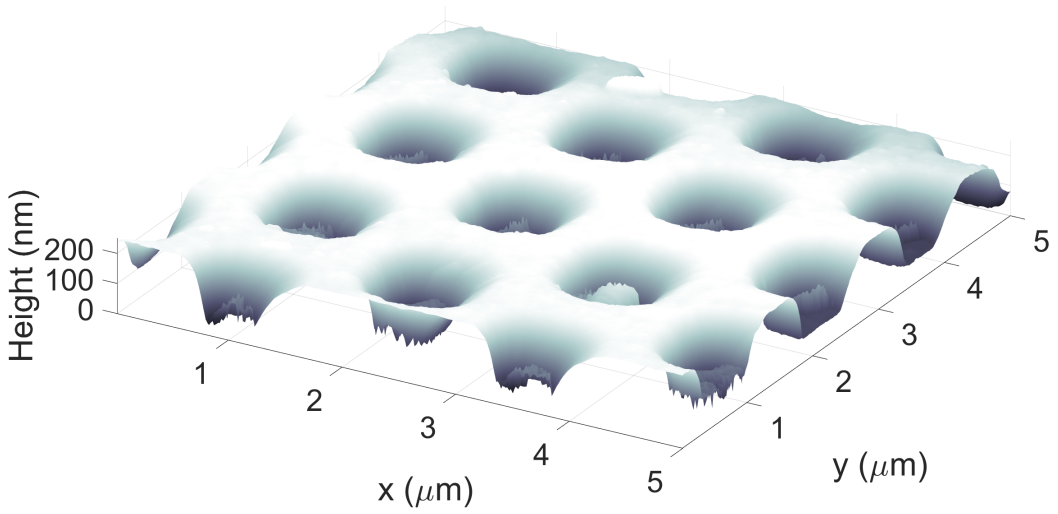

Figure 7.1: An atomic force microscopy (AFM) image of a $5 \times 5\,\mu\mathrm{m}^2$ surface area of the Nb antidot film sample.

7.6 Experimental Results with Insights from TDGL Simulations

7.6.1 Measurement Protocol

A representative measurement protocol is as follows. Initially, the probe (magnetic writer head) is positioned away from the sample. To create trapped vortices, the sample is first warmed to 10 K, well above the transition temperature. A DC magnetic field (B_{cooldown}) is then applied, and then the sample is gradually cooled from 10 K (above T_{c}) to 6.5 K (below T_{c}) at a rate of 0.55 mK/s. The sample is subsequently cooled rapidly from 6.5 K to 3.8 K (base temperature). Once the temperature stabilizes at 3.8 K, the DC magnetic field is *removed.* The probe is then brought into contact with the sample by adjusting the piezo stages. The microwave source is then activated with a fixed input frequency f and power, and $P_{2\mathrm{f}}$ is measured as the sample is gradually warmed from 3.8 K to 10 K. During this warmup process, the surface of the sample is exposed to a fixed rf magnetic field, $B_{\mathrm{rf}}\sin(\omega t)$, over a micron-scale area. Notably, *no* DC magnetic field

is applied during the microwave measurements, ensuring that the measured $P_{2\mathrm{f}}$ originates solely from trapped vortices in the sample.

The magnetic writer head itself exhibits temperature-independent nonlinearity. Since the measured $P_{2\mathrm{f}}$ is a combination of the probe background and the sample contribution, the probe background, determined by averaging the magnitude of $P_{2\mathrm{f}}(T)$ between 9.5 K and 10 K, is subtracted from the total signal to isolate the sample response.

With magnetic shielding in place, the residual DC magnetic field near the sample at low temperatures is found to be approximately 2.1 μT, as measured with an in-situ cryogenic 3-axis magnetometer (Bartington Cryomag-100).

7.6.2 Field of View of the Microscope Probe

The spatial resolution of the microscope ranges from sub-micron to micron scale, depending on the probe-sample separation, and the signal being analyzed. For measurements of the second-harmonic response, the spatial resolution is estimated to be approximately $1.1\,\mu$m for this specific setup, as discussed below.

The field of view of the probe can be estimated using a Monte Carlo approach. For instance, if the average number of trapped vortices within the field of view of the probe for a given B_{cooldown} value is 0.4, the probability of the probe interacting with a trapped vortex and detecting the $P_{2\mathrm{f}}$ signal is 40%. In practice, we perform six repeated measurements of $P_{2\mathrm{f}}(T)$ (with an input frequency of 1.824 GHz and input power of 6 dBm) and record how many trials exhibit a transition near the T_{c} of the sample in the low trapped vortex density regime (small B_{cooldown} values).

For $B_{\mathrm{cooldown}} = 0.061$ mT, 0.124 mT, and 0.188 mT, the number of trials showing a sample

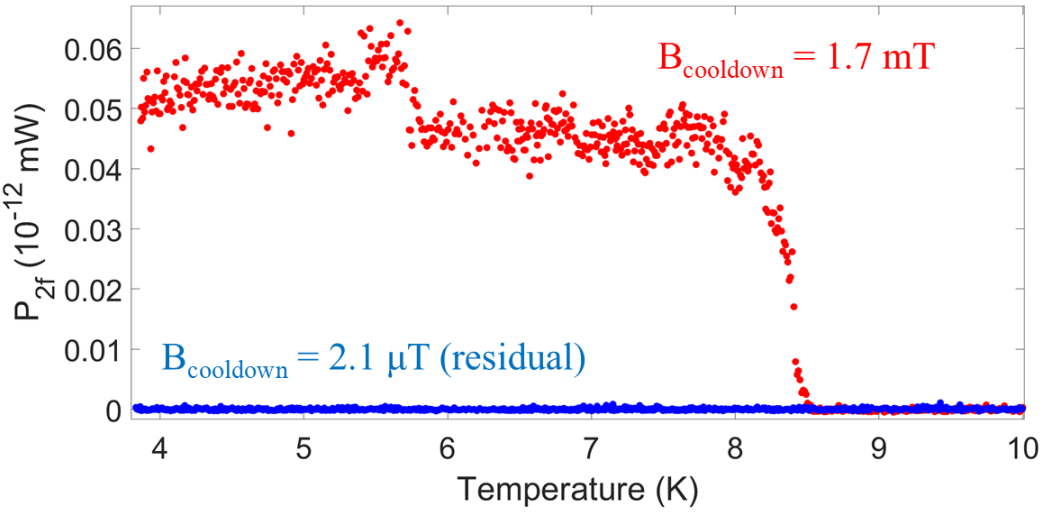

Figure 7.2: Representative data for P_{2f} as a function of temperature during a warmup measurement for two different cooldown fields. The red dots are the data for $B_{\text{cooldown}} = 1.7$ mT and the blue dots are the data for $B_{\text{cooldown}} = 2.1\,\mu$T. The input frequency is 1.81 GHz, and the input power is 6.8 dBm.

signal out of six measurements are 2, 4, and 5, respectively. Based on these results, the interaction range between the probe and trapped vortices is estimated to be approximately $1.1\,\mu$m.

7.6.3 Representative Data of $P_{2f}(T)$

Figure 7.2 shows the representative data for the linear power scale $P_{2f}(T)$ during a warmup measurement at a fixed location on the sample, for two different cooldown fields. The input frequency is $f = \omega/2\pi = 1.81$ GHz, and the input power is +6.8 dBm (at the room temperature microwave source).

The red dots are the data for $B_{\text{cooldown}} = 1.7$ mT. This cooldown magnetic field corresponds to an average flux quanta separation ($\sqrt{\Phi_0/B_{\text{cooldown}}}$) of $1.11\,\mu$m, a filling fraction of the antidot lattice of 1.70, and an average of 8.3 flux quanta in the field of view of the microwave microscope

probe (see Sec. 7.6.2). The $P_{2f}(T)$ shows a clear transition around 8.6 K, which is the T_c of the sample. For T<8.6 K, vortices are trapped in the sample, and their wiggling under stimulation by the rf magnetic field generates P_{2f}. For T>8.6 K, the sample loses superconductivity and the trapped vortices are released, and hence P_{2f} vanishes.

The blue dots are the data for $B_{\text{cooldown}} = 2.1\,\mu$T, which is the measured residual DC magnetic field when no external field is applied. This cooldown magnetic field corresponds to an average flux quanta separation of $31.40\,\mu$m, a filling fraction of the antidot lattice of 0.0021, and an average of 0.01 flux quanta in the field of view of the microwave microscope probe. Because the density of trapped vortices is very low, with high probability, there are no trapped vortices in the field of view of the probe, and thus there is no P_{2f}.

The contrast between the two data sets (red and blue) in Fig. 7.2 clearly demonstrates that P_{2f} originates from vortices trapped in the sample that are in the field of view of the probe, which agrees with **Core Feature 1** (see Sec. 6.4).

For simplicity, in the following text, the term "trapped vortices" will refer specifically to those within the field of view of the microwave microscope probe.

7.6.4 Vortex Configuration Change and $P_{2f}(T)$ Jump

A distinct discrete jump in $P_{2f}(T)$ is observed around 5.75 K for $B_{\text{cooldown}} = 1.7$ mT in Fig. 7.2. In the following, the temperature of such a discrete jump is denoted as $T_{P_{2f}(T)\text{jump}}$. One possible explanation for this $P_{2f}(T)$ jump is as follows: For temperatures slightly below 5.75 K, the trapped vortices are arranged in a specific configuration. As the temperature increases to approximately 5.75 K, the configuration of the trapped vortices changes. This change in

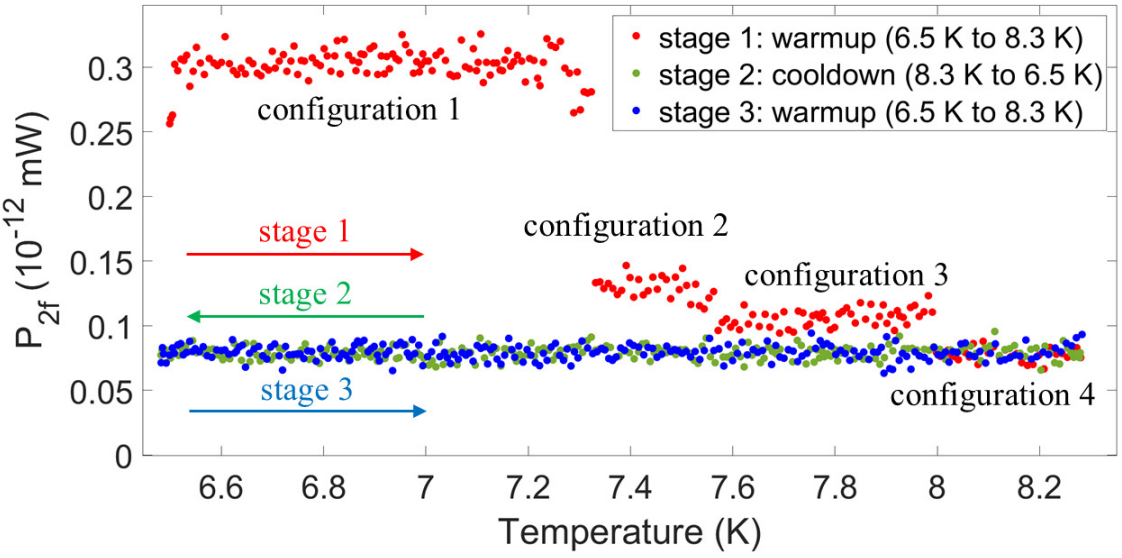

Figure 7.3: A 3-stage zigzag temperature sweep measurement of P_{2f} at a fixed location on the sample surface. The input frequency is 1.818 GHz, and the input power is 2 dBm.

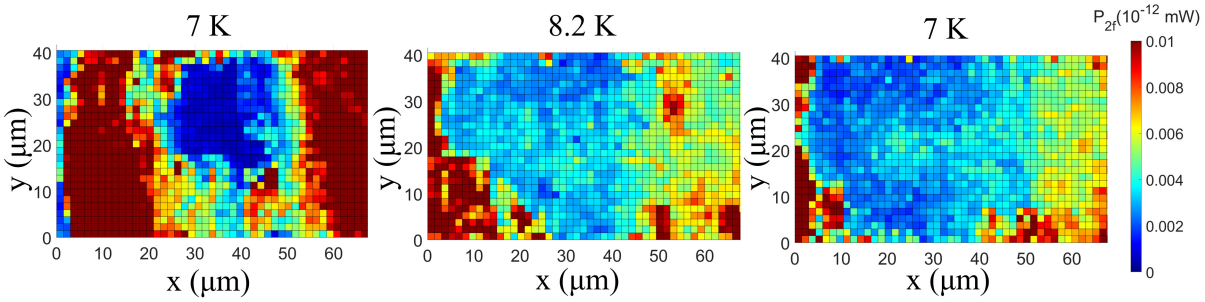

Figure 7.4: Three two-dimensional images of $P_{2f}(x, y)$ measured on the Nb film, plotted with a common color-bar (right). The step size is $1.5\,\mu$m. From left to right, the images are obtained successively at 7 K, 8.2 K, and then back to 7 K. The input frequency is 1.81 GHz, and the input power is 6.8 dBm.

configuration leads to the discrete jump in $P_{2f}(T)$ (see Sec. 6.6), since the measured P_{2f} comes from the superposition of the contributions of all the trapped vortices under the probe. The interpretation of $P_{2f}(T)$ jumps as indicators of vortex configuration changes is supported by the observation of P_{2f} hysteresis in temperature sweeps, as discussed below.

Figure 7.3 shows a 3-stage zigzag temperature sweep measurement of P_{2f}. The sample is first cooled from 10 K to 6.5 K with $B_{\text{cooldown}} = 1.7$ mT. The DC magnetic field is then removed, and three successive microwave measurements are performed: stage 1 involves warming from 6.5 K to 8.3 K (red), stage 2 involves cooling back from 8.3 K to 6.5 K (green), and stage 3 involves a second warming from 6.5 K to 8.3 K (blue). Note that the sample remains below T_c in this entire P_{2f} measurement process. In stage 1, three discrete jumps in $P_{2f}(T)$ are observed, whereas $P_{2f}(T)$ remains nearly temperature-independent during stages 2 and 3. This 3-stage zigzag temperature sweep clearly demonstrates the hysteresis of P_{2f} when $P_{2f}(T)$ jumps are present.

One possible interpretation is as follows: At the beginning of stage 1, the vortex configuration is metastable. As the temperature increases, the trapped vortices rearrange themselves into progressively more stable configurations (from configuration 1 to configuration 4), which is reflected in the $P_{2f}(T)$ jumps. Configuration 4 is the most stable among the four configurations, and thus the vortices tend to remain in this configuration during stages 2 and 3. This hysteresis behavior of $P_{2f}(T)$ jumps aligns with the hypothesis that these jumps correspond to transitions of trapped vortices from less stable to more stable configurations.

As additional evidence of the hysteresis behavior of P_{2f}, Fig. 7.4 presents spatially-scanned images of P_{2f} at multiple temperatures. The sample is first cooled from 10 K to 7 K with $B_{\text{cooldown}} = 1.7$ mT. The DC magnetic field is then removed, and three successive microwave measurements are performed: the first image at 7 K (left), the second image after warming from 7

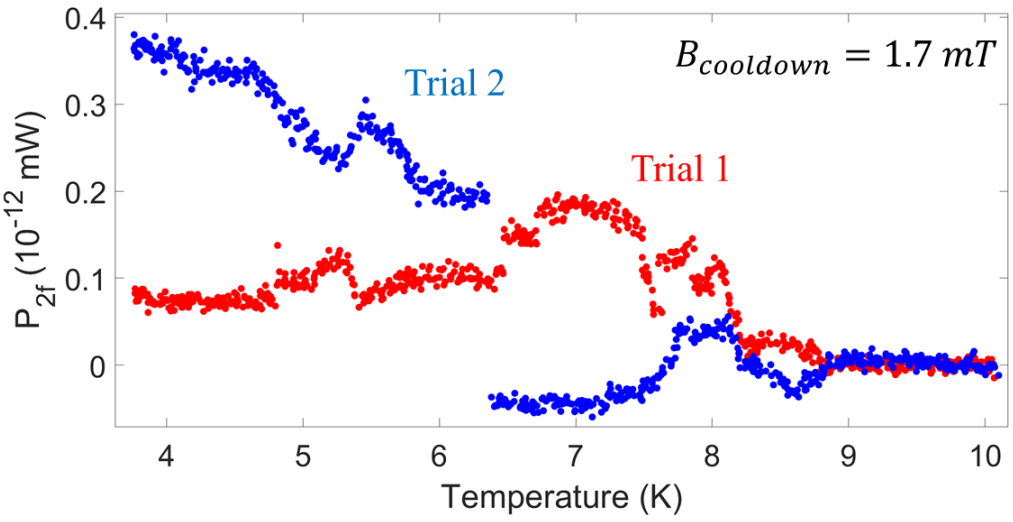

Figure 7.5: Two repeated measurements of $P_{2f}(T)$ at nominally the same location of the Nb film sample for $B_{\text{cooldown}} = 1.7$ mT. The input frequency is 1.819 GHz, and the input power is -5 dBm.

K to 8.2 K$< T_c$ (center), and the third image after cooling back from 8.2 K to 7 K (right). The contrast between the left and right images clearly demonstrates the hysteresis behavior of P_{2f}.

The measured value of P_{2f} is highly sensitive to the details of trapped vortex configurations (see Sec. 6.5), which are complex and inherently stochastic. For example, Fig. 7.5 presents two repeated measurements of $P_{2f}(T)$ performed at the same location under nominally identical conditions, where the contrast between Trial 1 (red) and Trial 2 (blue) highlights this stochastic behavior. (The negative $P_{2f}(T)$ observed in Trial 2 is due to the naive background subtraction, as discussed in Sec. 2.4.7.) Given this sensitivity, rather than focusing on the absolute value of P_{2f}, we analyze $P_{2f}(T)$ jumps, which serve as indicators of changes in trapped vortex configurations and are therefore closely related to pinning properties.

7.7 Vortex Pinning Properties and Statistics of $P_{2f}(T)$ Jumps

7.7.1 Temperature Dependence of $P_{2f}(T)$ Jumps

To further investigate $P_{2f}(T)$ jumps, we perform repeated measurements of $P_{2f}(T)$ from 3.8 K to above T_c at nominally the same location of the Nb film sample and analyze the statistical properties of $T_{P_{2f}(T)\text{jump}}$.

Figure 7.6(a) presents the statistical distribution of $T_{P_{2f}(T)\text{jump}}$ as a function of temperature. The data is obtained from 10 repeated measurements of $P_{2f}(T)$ during a temperature sweep from 3.8 K to above T_c, conducted nominally at the same location on the sample surface, with $B_{\text{cooldown}} = 0.64$ mT. This cooldown magnetic field corresponds to an average flux quanta separation of $1.80\,\mu$m, a filling fraction of the antidot lattice of 0.65, and an average of 3.2 flux quanta in the field of view of the microwave microscope probe.

The distribution in Fig. 7.6(a) reveals three distinct clusters: one above $T_{P_{2f}(T)\text{jump}}/T_c = 0.8$, another peaked around $T_{P_{2f}(T)\text{jump}}/T_c = 0.72$, and a third below $T_{P_{2f}(T)\text{jump}}/T_c = 0.6$.

The rearrangement of trapped vortices as the temperature increases is inherently complex, potentially resulting in a multi-component $T_{P_{2f}(T)\text{jump}}$ distribution. For example, an Abrikosov vortex might jump from one pinning site to a nearby pinning site [201, 204], be attracted to and captured by an antidot, or flux trapped by antidots could rearrange into other antidots near T_c.

The three distinct clusters in Fig. 7.6(a) suggest the presence of three different types of trapped vortex rearrangement events in the sample. The profiles and temperatures of these clusters provide insight into the pinning properties of the sample. Notably, the cluster above $T_{P_{2f}(T)\text{jump}}/T_c = 0.8$ accounts for more than half of the total $P_{2f}(T)$ jumps. Specifically, the

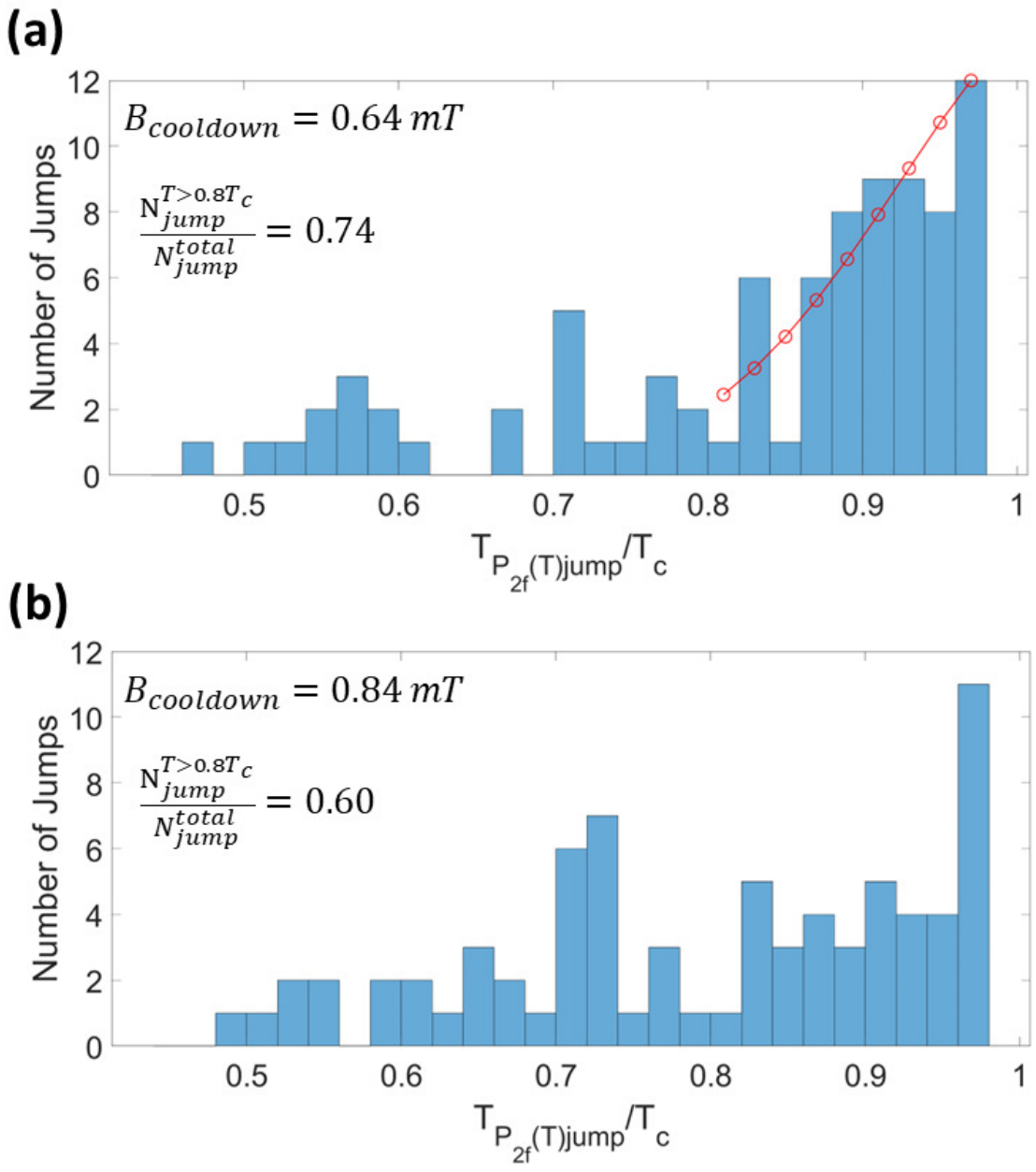

Figure 7.6: Histogram of the temperatures at which $P_{2f}(T)$ jumps occur ($T_{P_{2f}(T)\text{jump}}$). The data is obtained from 10 repeated measurements of $P_{2f}(T)$ from 3.8 K to above T_c at Location 1. Panels (a) and (b) correspond to cooldown fields of $B_{\text{cooldown}} = 0.64$ mT and $B_{\text{cooldown}} = 0.84$ mT, respectively. The input frequency is 1.708 GHz, and the input power is -3 dBm. The red curve in panel (a) is the fitting result using Eqs. 7.1 and 7.2.

high-temperature jump ratio, defined as $N_{\text{jump}}^{T>0.8T_c}/N_{\text{jump}}^{\text{total}}$, is 0.74 for Fig. 7.6(a).

7.7.2 Extracting Vortex Pinning Parameters

One possible mechanism for trapped vortex rearrangement events is thermal activation [37, 38, 160, 204–207]. Under this mechanism, trapped vortices are expected to rearrange more frequently at higher temperatures, consistent with the trend observed in the cluster above $T_{P_{2f}(T)\text{jump}}/T_c = 0.8$ in Fig. 7.6(a). To analyze the data further, assume a temperature-dependent activation energy $U(T)$ as [207–214]

$$U(T) = U_0 \left(1 - \frac{T}{T_c}\right)^{\gamma} \tag{7.1}$$

where γ is a scaling exponent. Assume the likelihood of trapped vortex rearrangement events $P(T)$ due to thermal activation at temperature T is given by

$$P(T) \propto e^{-\frac{U(T)}{k_B T}}. \tag{7.2}$$

Assuming that trapped vortex rearrangement events for $T > 0.8\ T_c$ in Fig. 7.6(a) are primarily driven by thermal activation, with vortex-vortex interactions playing a minor role, we fit the probability distribution above $T = 0.8\ T_c$ using Eqs. 7.1 and 7.2. The resulting fit yields a pinning potential of $U_0 = 14.8\ k_B T_c = 127.3\ \text{K} = 10.97\ \text{meV}$ and a scaling exponent of $\gamma = 1.43$.

Building on this analysis, we investigate the spatially-resolved vortex pinning properties (U_0 and γ) of the sample. We perform measurements following the same procedure as described in Fig. 7.6(a) (Location 1) but at a different location on the sample surface (Location 2). Locations

Location	U_0 (meV)	γ	$U(T)$ (meV) for $0.30 < T/T_c < 0.48$
1	10.97	1.43	between 4.26 and 6.57
2	9.86	1.76	between 3.08 and 5.25

Table 7.1: Summary of the vortex pinning parameters (U_0 and γ) extracted from $P_{2f}(T)$ measurements using Eqs. 7.1 and 7.2. Data are presented for two distinct locations on the sample surface (Location 1 and Location 2), separated by 50 μm.

1 and 2 are separated by 50 μm. The extracted pinning parameters for these two locations are summarized in Table 7.1.

Several previous studies have described the temperature dependence of the activation energy $U(T)$ using the form given by Eq. 7.1. Typically, the exponent γ falls within the range $0.5 < \gamma < 2$ [211–213]. In our analysis, we obtained $\gamma = 1.43$ and 1.76 at Locations 1 and 2, respectively, which are consistent with values commonly reported in the literature.

Vortex pinning properties in Nb films have previously been studied in Ref. [207], where a temperature-independent activation energy of 1.9 meV was obtained by fitting experimental data in the temperature range $0.3 < T/T_c < 0.48$. In contrast, we use a temperature-dependent activation energy $U(T)$ described by Eq. 7.1; our fitted values in the same temperature range, summarized in the last column of Table 7.1, are comparable to that reported in Ref. [207]. Furthermore, our results also agree in magnitude with the activation energies of Pb-Tl alloy, reported to be between 3 meV and 14 meV in Ref. [205].

Taken together, these comparisons confirm that the pinning parameters (U_0 and γ) obtained from our analysis are consistent with values reported in the literature, thus validating the physical reasonability of our results.

Cooldown from room temperature to 3.8 K	Location	input frequency (GHz)	input power (dBm)
First	1 2	1.708	-3
Second	3 4	1.819	-5

Table 7.2: Summary of the measurement details at four distinct locations on the sample surface. Locations 1 and 2 are separated by 50 μm, as are Locations 3 and 4. Measurements at Locations 1 and 2 were performed during the same cooldown from room temperature to 3.8 K, while measurements at Locations 3 and 4 were obtained in a separate cooldown from room temperature to 3.8 K.

7.7.3 Trapped Vortex Density and Its Role in Vortex Dynamics

Figure 7.6(b) shows the statistical distribution of $T_{P_{2f}(T)\text{jump}}$ as a function of temperature for $B_{\text{cooldown}} = 0.84$ mT. The measurement procedure is identical to that of Fig. 7.6(a), except with a higher B_{cooldown}, resulting in an increased trapped vortex density. Compared to Fig. 7.6(a) ($N_{\text{jump}}^{T>0.8T_c}/N_{\text{jump}}^{\text{total}} = 0.74$), the distribution of $T_{P_{2f}(T)\text{jump}}$ in Fig. 7.6(b) is more spread out, with a lower high-temperature jump ratio of $N_{\text{jump}}^{T>0.8T_c}/N_{\text{jump}}^{\text{total}} = 0.60$.

Building on the results from Fig. 7.6, we extend the measurements to multiple B_{cooldown} values, corresponding to different trapped vortex densities, at four distinct locations on the sample surface (Locations 1 to 4). The measurement details at the four locations are summarized in Table 7.2. Figure 7.7 presents the high-temperature jump ratio $N_{\text{jump}}^{T>0.8T_c}/N_{\text{jump}}^{\text{total}}$ as a function of B_{cooldown}.

As shown in Fig. 7.7, $N_{\text{jump}}^{T>0.8T_c}/N_{\text{jump}}^{\text{total}}$ decreases with increasing B_{cooldown} across all four measurement locations. One possible explanation for this trend is as follows. In the low trapped vortex density regime (small B_{cooldown}), vortex-vortex interactions are weak, and trapped vortex rearrangement events are primarily driven by thermal activation, which is most significant near

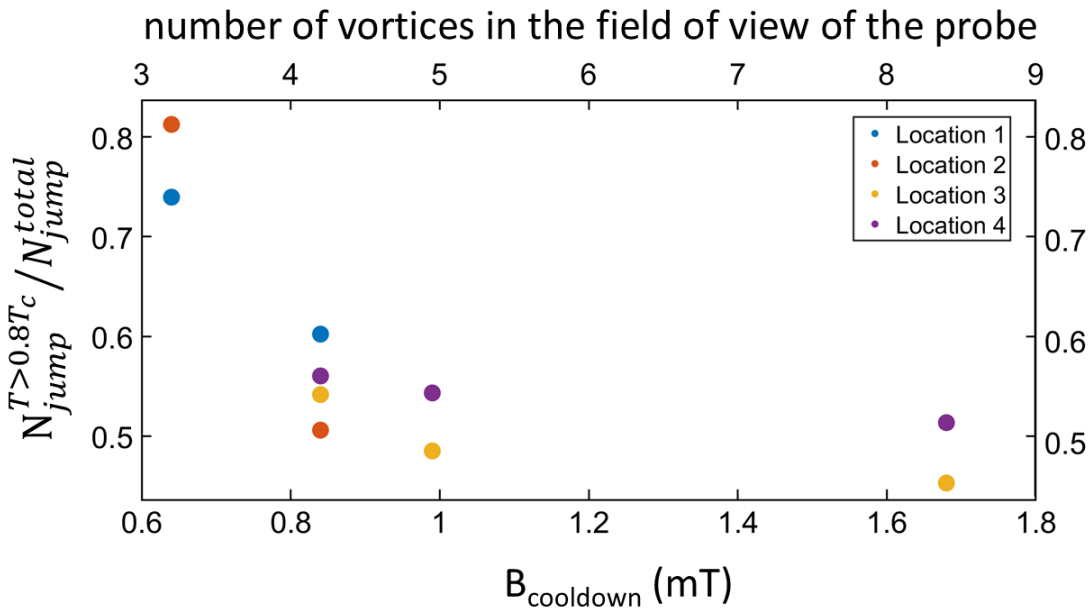

Figure 7.7: High-temperature jump ratio $N_{\text{jump}}^{T>0.8T_c}/N_{\text{jump}}^{\text{total}}$ for different B_{cooldown} values, measured at four distinct locations on the sample surface. The measurement details at the four locations are summarized in Table 7.2. The data in Fig. 7.6 is obtained at Location 1.

T_c. In contrast, in the high trapped vortex density regime (large B_{cooldown}), the trapped vortex configuration becomes more complex, as both the pinning potential of the antidot array and vortex-vortex interactions play a significant role. In this regime, trapped vortices can rearrange even at lower temperatures.

Understanding trapped vortex rearrangement mechanisms beyond thermal activation near T_c requires more sophisticated theoretical analysis and numerical simulations, which are beyond the scope of this work.

7.8 Conclusion

In this work, we present a proof-of-principle study demonstrating the use of local P_{2f} measurements with our near-field magnetic microwave microscope to investigate the dynamics of

trapped vortices at the micron scale. This microscopic approach complements traditional methods that average the behavior of many vortices. Specifically, we show that this technique can reveal depinning events of trapped vortices and provide insights into spatially-resolved pinning properties. Furthermore, our results highlight how vortex pinning behavior varies across different trapped vortex density regimes, offering a new perspective on the interplay between pinning potentials and vortex-vortex interactions. It is particularly relevant for applications such as SRF cavities, superconducting quantum circuits, and superconducting digital electronics. Future work includes developing more sophisticated models beyond the thermal activation mechanism to further extract quantitative information about pinning properties from $P_{2\mathrm{f}}$ measurements.

Chapter 8: Conclusion and Future Directions

In this thesis, we have investigated two distinct vortex-related phenomena in superconductors: rf vortex nucleation and trapped vortex dynamics. The experimental setup for these studies is described in Chapter 2, while the TDGL simulation framework is detailed in Chapter 3. Chapters 4 (simulations) and 5 (measurements) explore rf vortex nucleation induced by surface defects and its associated third-harmonic response. Chapters 6 (simulations) and 7 (measurements) examine the dynamics of trapped vortices and the resulting second-harmonic response.

Our findings provide new insights into the nonlinear microwave response of superconductors, demonstrating how local defects and vortex pinning sites influence rf vortex nucleation and trapped vortex motion. The combination of experimental measurements and TDGL simulations has allowed us to extract meaningful physical parameters related to vortex dynamics at microwave frequencies, contributing to a deeper understanding of vortex-induced nonlinearities in superconducting materials.

The future directions of this research can be categorized into three main areas: experimental measurements, theoretical simulations, and hardware development.

In this thesis, we have measured seven Nb/Cu films intended for SRF accelerator cavity applications and one Nb film with an antidot flux pinning array. Since different superconducting samples possess different types of surface defects, their behavior under intense rf magnetic fields

varies, leading to distinct signatures in their third-harmonic response. Likewise, variations in vortex pinning—whether from natural or engineered pinning sites—affect trapped vortex dynamics, influencing the second-harmonic response.

A natural extension of this work is to expand the scope of measurements by investigating a broader range of superconducting materials, including alternative Nb/Cu deposition techniques and artificially engineered pinning landscapes. Systematic analysis of the nonlinear microwave response in these samples will provide deeper insights into rf vortex nucleation mechanisms and the role of vortex pinning in harmonic generation.

Beyond nonlinear responses associated with surface defects and vortex pinning, the microwave microscope also holds promise for probing fundamental phenomena in superconductors. For instance, second-harmonic response measurements could potentially serve as a sensitive probe of time-reversal invariance breaking in unconventional superconductors such as UTe_2.

The ability to extract meaningful physical insights from experimental measurements depends critically on the theoretical framework used to interpret them. In the case of trapped vortex dynamics studied in this thesis, thermal activation is considered when fitting the data and extracting pinning parameters. However, vortex pinning is a complex phenomenon with multiple competing mechanisms, and thermal activation is only one aspect of the broader picture.

Future research could explore more sophisticated models that go beyond thermal activation. Further improvements in TDGL simulations, such as incorporating more realistic defect geometries, could enhance our ability to quantitatively predict nonlinear response signatures. These refinements would provide deeper insight into the microscopic physics underlying vortex-induced nonlinearities.

For over two decades, members of the Anlage Lab have advanced the field of superconducting microwave response through the continuous development of near-field magnetic microwave

microscopes. Each iteration of the microscope has enabled new types of measurements, allowing us to extract increasingly detailed information about superconducting materials. A promising future direction is the development of a next-generation microwave microscope based on atomic force microscopy (AFM) architecture, as discussed in Appendix B.

Appendix A: Operating Procedures for the Cryostat and Microwave Microscope

A.1 Step-by-Step Operation of the Entropy Cryostat and Near-Field Magnetic Microwave Microscope

The following steps outline the procedure for preparing and operating the Entropy cryostat and the near-field magnetic microwave microscope:

1. Prepare the microscope head:
    - First, solder a new magnetic writer to a connector using lead-free solder (see Sec. 2.3 for further discussion).
    - Second, measure the resistance between the inner and outer conductors of the connector. It should be approximately $6\ \Omega$.
    - Third, wear gloves, mount the magnetic writer on a metal support, and securely attach it to the XYZ piezo stages
2. Wear gloves if you are going to touch anything in the cryostat, or anything that will be inserted into the cryostat later.
3. Mount the sample beneath the 4 K cold plate. Apply vacuum grease if necessary to ensure good thermal contact.

4. Attach the microscope head beneath the 4 K cold plate, ensuring proper alignment with the sample.

5. Connect the wires for the piezo stages (see Fig. A.1). Test piezo motion and verify the safe movement range of the x, y, and z piezo stages.

6. Attach thermal strips between the piezo stages and the 4 K cold plate to optimize thermal transport.

7. Mount the thermometer near the sample.

8. Connect the coaxial cable for microwave signal transmission.

9. Ensure all components are well thermally anchored to both the 70 K plate and the 4 K plate.

10. Verify the functionality of the thermometers, P_{3f} probe background, and the magnetic coil (above the 4 K cold plate) under ambient conditions:

    - For thermometers: There are 3 thermometers: thermometers A and B are typically mounted beneath the 4 K cold plate, while thermometer C is typically mounted beneath the 70 K plate. Make sure the readings of these 3 thermometers are around 297 K.
    - For P_{3f} probe background: Apply three input power levels (-10 dBm, -5 dBm, and 0 dBm) and confirm that P_{3f} of the probe exhibits a clear dependence on input power.
    - For the magnetic coil: Apply three DC current levels (0 A, 0.05 A, and 0 A) and confirm that the cryogenic 3-axis magnetometer detects the expected magnetic field values.

11. Close the golden can.

12. Recheck the thermometers, $P_{3\mathrm{f}}$ probe background, and the magnetic coil again to verify proper connections.

13. Close the remaining two shielding cans.

14. Recheck the thermometers, $P_{3\mathrm{f}}$ probe background, and the magnetic coil again to verify proper connections before proceeding.

15. Set up the magnetic shielding.

16. Perform a final check of the thermometers, $P_{3\mathrm{f}}$ probe background, and the magnetic coil.

17. Pump down the chamber to achieve a vacuum pressure below 10 milli-Torr (estimated duration: 2–3 hours).

18. Once the desired low pressure is reached, begin cooling down the system (estimated duration: 10–12 hours):

    - First, turn on the cooling water.
    - Then, turn on the compressor.

19. After reaching the target low temperature (approximately 3.8 K), turn off the pump in the following sequence:

    - Close the valve first.
    - Then, turn off the vacuum pump.

20. Determine the safe range of piezo motion. If the piezo is stuck, manually increase the voltage to release it from confinement.

21. Calibrate the heater power using the current heater-thermometer setup.

22. Begin the measurement of interest.

23. Complete the measurement of interest.

24. Turn off both the heater and the microwave signal.

25. Retract the piezo to detach it from the sample surface. Set the position to $(x, y, z) = (2500, 2500, 0)$.

26. Shut down the cooling system to allow the cryostat to warm up to room temperature (estimated duration: 12–24 hours):

    - First, turn off the compressor.
    - Then, turn off the cooling water.

27. Once the system has returned to room temperature and the pressure is higher than the vacuum level, gently break the vacuum:

    - First, detach the tube connected to the pump.
    - Then, slowly loosen the valve. Use a piece of metal to cover the hole of the vacuum pump.

28. Remove the magnetic shielding.

29. Wear gloves.

30. Remove the three shielding cans one by one.

31. Disconnect all wires and cables, then carefully detach the microscope head.

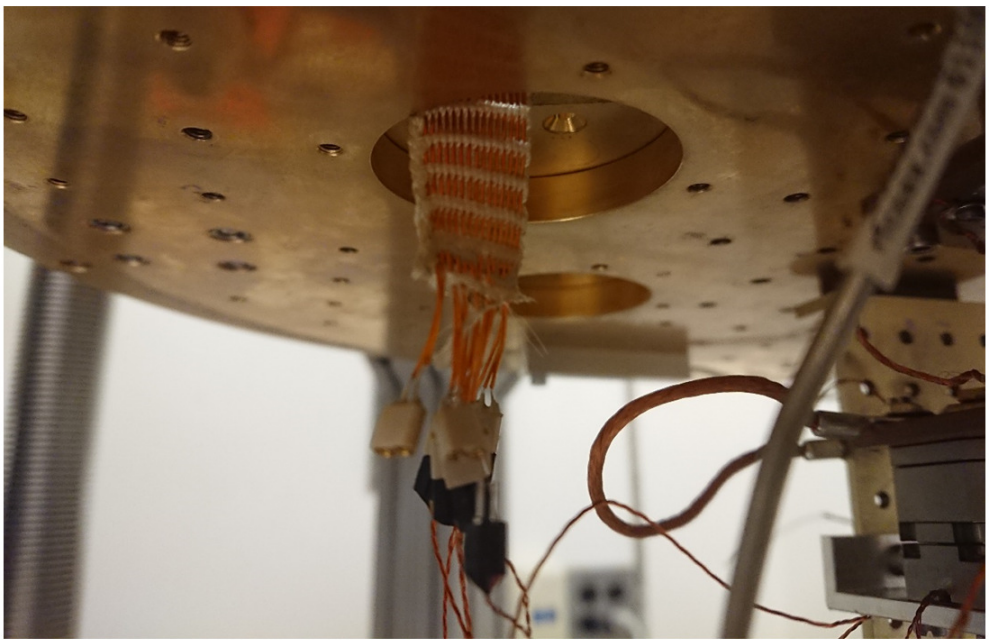

Figure A.1: Image of the six connectors used for wiring the three piezo stages. The connection order from outside to inside is as follows: (1) two pins for the x piezo, (2) two pins for the z piezo, (3) two pins for the y piezo, (4) three pins for the x piezo, (5) three pins for the z piezo, (6) three pins for the y piezo. When connecting the controller side to the piezo side, the black side (piezo) should be connected to the flat side (controller), and the red side (piezo) should be connected to the curved side (controller).

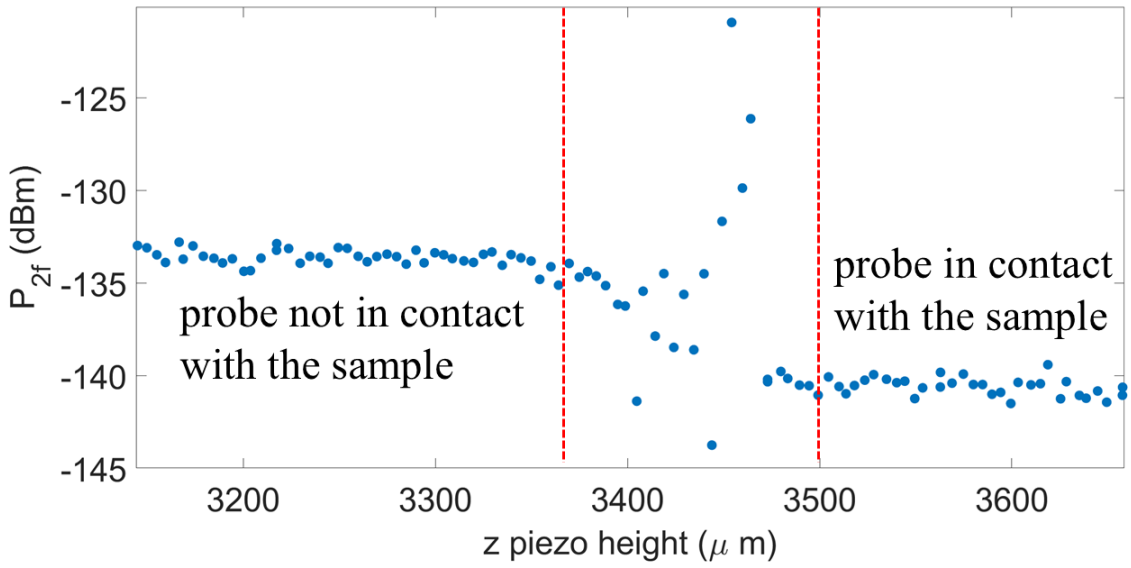

Figure A.2: A typical $P_{2f}(z)$ measurement, where z represents the height of the z piezo. The variation of P_{2f} with z provides a means to verify the probe-sample separation. The sample used is the antidot Nb film studied in Chapter 7. The measurement is performed at a temperature of 3.8 K with an input frequency of 1.824 GHz and an input power of 0 dBm.

A.2 Probe-Sample Contact Verification

The probe-sample separation can be verified by monitoring the nonlinear response as a function of the z piezo height. This method is used to verify probe-sample contact at both room temperature and base temperature. An example is presented in Fig. A.2.

Figure A.2 presents a typical $P_{2f}(z)$ measurement, where z represents the height of the z piezo. The sample used is the antidot Nb film studied in Chapter 7. The measurement is performed at a temperature of 3.8 K with an input frequency of 1.824 GHz and an input power of 0 dBm.

The $P_{2f}(z)$ curve exhibits three distinct regions:

1. Probe not in contact with the sample ($z < 3360$ μm): In this region, $P_{2f}(z)$ originates from the probe background and remains independent of z since no interaction occurs between the

probe and the sample.

2. Probe engaging with the sample (3360 μm $< z <$ 3500 μm): As the probe begins to make contact with the sample, the probe-sample contact is typically unstable. Consequently, $P_{2\mathrm{f}}(z)$ exhibits significant fluctuations and a strong dependence on z.

3. Stable probe-sample contact ($z >$ 3500 μm): When the probe is further pressed against the sample, the probe-sample contact stabilizes. In this region, $P_{2\mathrm{f}}(z)$ becomes nearly independent of z, indicating a stable contact configuration. A z-independent $P_{2\mathrm{f}}(z)$ is desirable, as it suggests that the probe-sample contact has a high tolerance to small z variations.

A.3 Thermal Anomaly Observed in Entropy Cryostat and Its Mitigation

The Entropy cryostat exhibits an abnormal exothermic reaction during warmup. Throughout this discussion, the temperature refers to the reading recorded by the thermometer mounted beneath the 4 K cold plate. If the cryostat is cooled rapidly from 10 K to 4 K and subsequently warmed up gradually, an exothermic event occurs around 6.9 K during the warmup process. Specifically, the temperature rises by more than 0.5 K (from 6.9 K to above 7.4 K) within a few minutes, even when the heater power remains unchanged.

A systematic investigation of different cooldown procedures reveals that this abnormal exothermic reaction can be mitigated by slowing the cooldown rate. Specifically, the reaction is significantly suppressed by the following cooldown procedure: first, gradually cooling the cryostat from 10 K to 8 K at a rate of 1.67 mK/s, and then cooling rapidly from 8 K to the base temperature by setting the heater power to zero.

Appendix B: Early Development of a Next-Generation Microwave Microscope

Figure B.1 presents a schematic of the next-generation microwave microscope setup. The system consists of a microwave source and spectrum analyzer for excitation and detection, a Bruker DAFMCH holder combined with the PrimeNano SMIM-300 probe for near-field microwave measurements, and a set of cryogenic piezo scanners (ANSxy100, ANSz100) controlled via ANM200, ANC300, and ASC500 controllers for precise sample scanning. An interferometric displacement module (LDM1300) monitors probe position in the cryogenic environment. The piezo scanners, their respective controllers, and the LDM1300 module are all purchased from Attocube. The temperature regulation is handled by a Lakeshore 340 unit. Data acquisition (DAQ) is performed via a National Instruments computer interface.

The nanometer-scale cryogenic scanning module consists of two Attocube scanners: ANSxy100 and ANSz100. The ANSxy100 scanner is an open-loop xy scanner with a $9 \times 9\,\mu\mathrm{m}^2$ positioning range at $T = 4\ \mathrm{K}$, offering sub-nanometer resolution. The ANSz100 scanner is an open-loop z scanner with a $15\ \mu\mathrm{m}$ positioning range at $T = 4\ \mathrm{K}$, also providing sub-nanometer resolution.

The SMIM-300 probe, developed by PrimeNano, is a cantilever-based microwave microscope probe featuring a coaxially shielded structure with a solid metal probe tip.

The optical system for monitoring the position of the SMIM-300 probe consists of a cryogenic optical fiber, a room-temperature optical fiber, and an LDM1300 module. The LDM1300

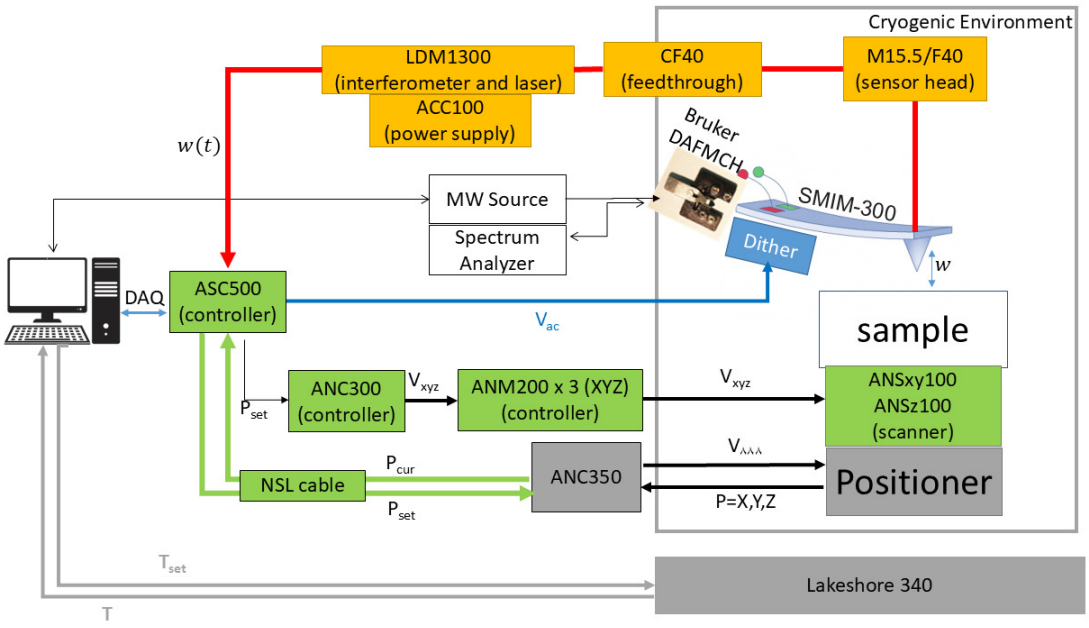

Figure B.1: Schematic of the next-generation microwave microscope setup. Components highlighted in green correspond to spatial control, while components in yellow are used for probe displacement monitoring.

module integrates an infrared laser operating at a wavelength of 1310 nm with an interferometer for precise displacement measurements.

To verify the functionality of the scanners, laser, and interferometer, we perform the following tests. The optical fiber is positioned vertically above the ANSz100 scanner, brought into close proximity for accurate displacement monitoring. The output signal of the LDM1300 module is monitored using an oscilloscope. As the ANSz100 expands, the interference signal from LDM1300 exhibits periodic variations, with the expected number of interference periods observed over the full expansion range of the ANSz100. This confirms the proper operation of the laser source, the interferometer, and the ANSz100 scanner. The same test is applied to the ANSxy100 scanner to ensure its functionality.

Figure B.2 presents optical images of a PrimeNano SMIM-300 probe. The probe consists of

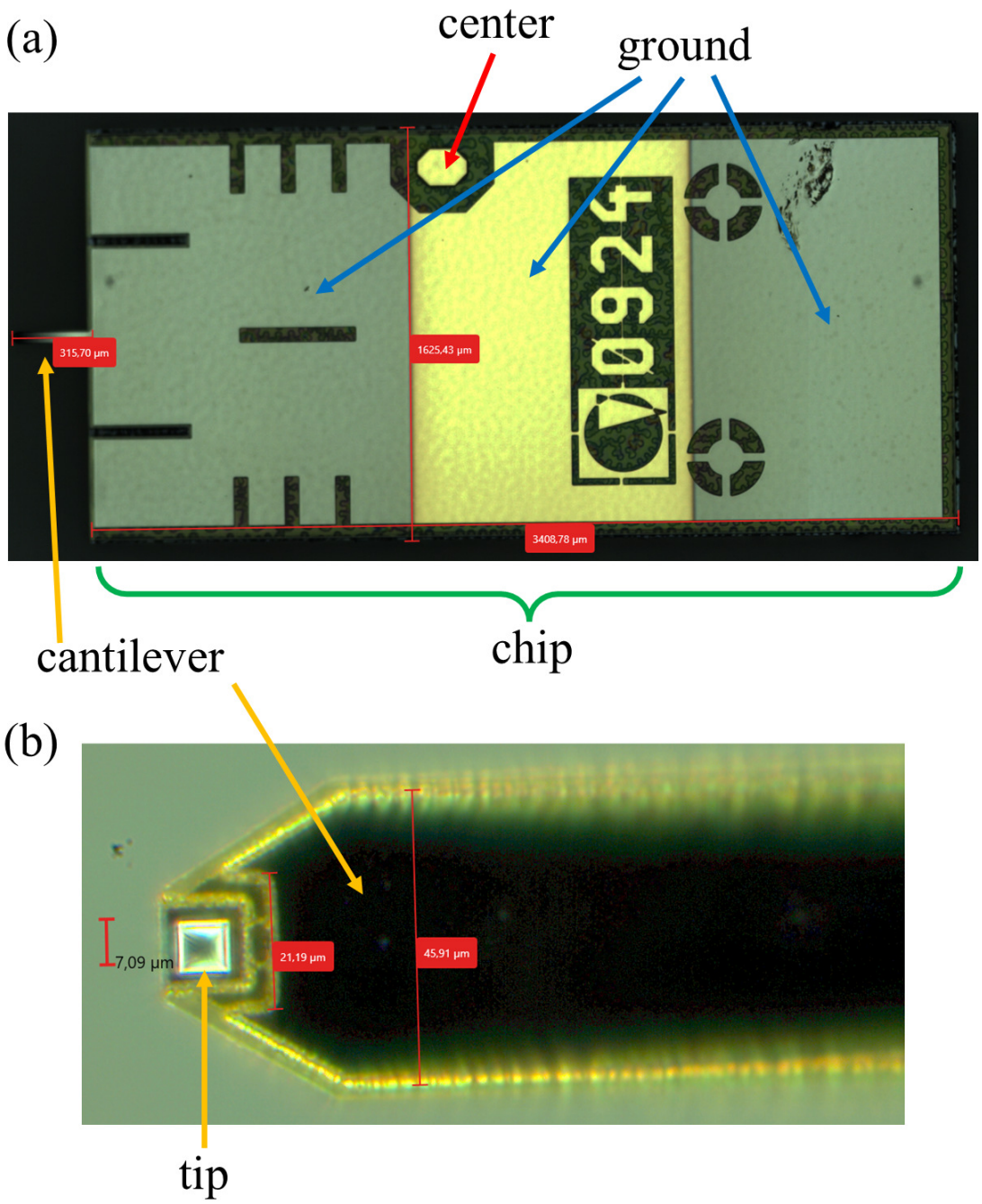

Figure B.2: Optical images of a PrimeNano SMIM-300 probe. (a) Overview of the entire probe, showing the chip and the cantilever. The center conductor and ground pads for electrical connection are labeled. (b) Close-up view of the cantilever and the metal tip at its end.

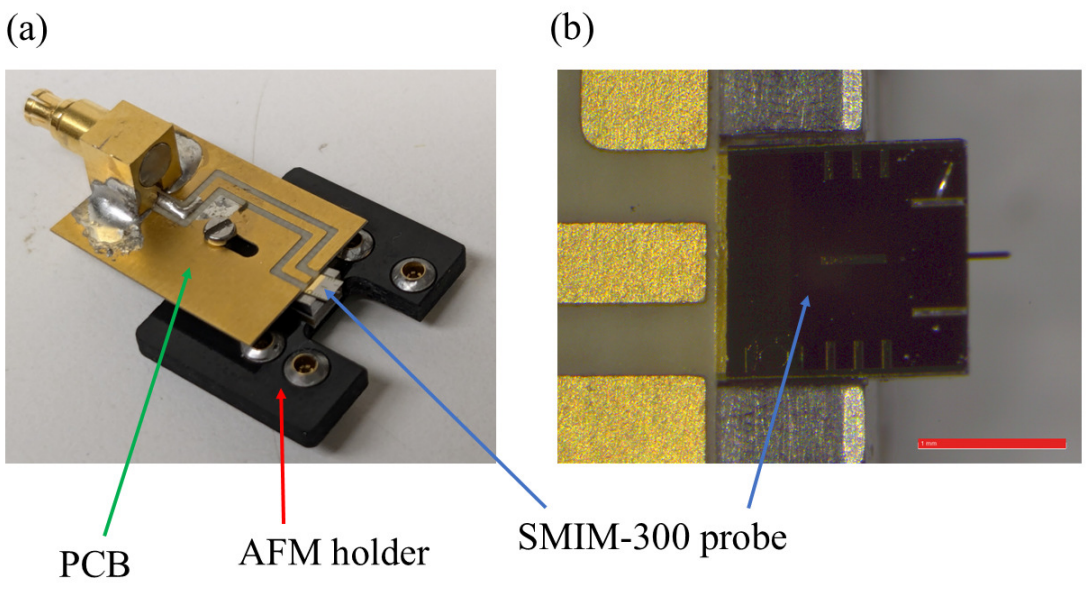

Figure B.3: Optical images of a PrimeNano SMIM-300 probe integrated into a probe holder assembly. (a) Photograph of the assembled setup, including the printed circuit board (PCB), atomic force microscope (AFM) holder, and the SMIM-300 probe. (b) Close-up view of the probe region.

a chip, a cantilever, and a solid metal tip located at the end of the cantilever. Panel (a) shows an overview of the entire probe, including the chip and cantilever. The center conductor and ground pads used for electrical connection are labeled. Panel (b) provides a close-up view of the cantilever and the metal tip, which is used for near-field microwave measurements.

To transmit microwave signals to the SMIM-300 probe, a custom printed circuit board (PCB) is fabricated. Figure B.3 shows optical images of a PrimeNano SMIM-300 probe integrated into a probe holder assembly, which consists of the PCB, an atomic force microscope (AFM) holder, and the SMIM-300 probe. The probe is seated in the slot of the AFM holder. An SMPM connector is soldered to the PCB to enable the delivery of microwave signals. These signals can then be transmitted to the probe via wire bonding between the PCB and the probe pads (not shown in Fig. B.3).

Appendix C: Dimensionless Forms of the TDGL Equations

C.1 Dimensionless TDGL Equations: Form I

To facilitate numerical simulations, it is useful to express the TDGL equations in a dimensionless form. We introduce the following dimensionless variables (the ˜ transformation):

$$x = \lambda \tilde{x} \tag{C.1}$$

$$t = \tau_{GL} \tilde{t} \tag{C.2}$$

$$\psi = \psi_\infty \tilde{\psi} \tag{C.3}$$

$$A = (\sqrt{2} B_{\mathrm{c}} \lambda) \tilde{A} = \left(\frac{\hbar}{e_* \xi} \right) \tilde{A} \tag{C.4}$$

$$\sigma = \frac{1}{\mu_0 \kappa^2 D} \tilde{\sigma} \tag{C.5}$$

That is, length is in the unit of penetration depth λ; time is in the unit of Ginzburg-Landau order parameter relaxation time τ_{GL}; the order parameter is in the unit of its value deep in the bulk ψ_∞; vector potential is in the unit of thermodynamic critical field times penetration depth $\sqrt{2} B_{\mathrm{c}} \lambda$; normal state conductivity is in the unit of $\frac{1}{\mu_0 \kappa^2 D}$.

Under these transformations, the current density and magnetic field scale as:

$$J = \frac{\sqrt{2}B_{\mathrm{c}}}{\mu_0 \lambda}\tilde{J} \tag{C.6}$$

$$B = (\sqrt{2}B_{\mathrm{c}})\tilde{B} \tag{C.7}$$

Substituting these changes of variables into the TDGL equations (Eqs. 3.21 and 3.22), we obtain their dimensionless form:

$$\frac{\partial \tilde{\psi}}{\partial \tilde{t}} = -\left(\frac{i}{\kappa}\tilde{\nabla} + \tilde{A}\right)^2 \tilde{\psi} + \tilde{\psi} - |\tilde{\psi}|^2\tilde{\psi} \tag{C.8}$$

$$\tilde{\sigma}\frac{\partial \tilde{A}}{\partial \tilde{t}} = -\frac{i}{2\kappa}\left(\tilde{\psi}^*\tilde{\nabla}\tilde{\psi} - \tilde{\psi}\tilde{\nabla}\tilde{\psi}^*\right) - |\tilde{\psi}|^2\tilde{A} - \tilde{\nabla}\times\tilde{\nabla}\times\tilde{A} \tag{C.9}$$

Since length is expressed in units of the finite-temperature penetration depth $\lambda(T)$, the vortex core size in dimensionless units is given by

$$\tilde{r}_{\mathrm{vortex}} \approx \tilde{\xi} = \frac{\tilde{\lambda}}{\kappa} = \frac{1}{\kappa}. \tag{C.10}$$

As a result, the vortex size remains constant in this dimensionless formulation, independent of temperature, which simplifies visualization across different temperatures.

C.2 Dimensionless TDGL Equations: Form II

Here, we introduce an alternative set of dimensionless variables (the $\hat{}$ transformation) based on temperature-independent dimensional factors (scaled by their values at $T = 0$):

$$x = \lambda(T = 0)\hat{x} \tag{C.11}$$

$$t = \tau_{GL}(T = 0)\hat{t} \tag{C.12}$$

$$\psi = \psi_{\infty}(T = 0)\hat{\psi} \tag{C.13}$$

$$A = \left(\sqrt{2}B_{\mathrm{c}}(T = 0)\lambda(T = 0)\right)\hat{A} \tag{C.14}$$

$$\sigma = \frac{\tau_{GL}(T = 0)}{\mu_0(\lambda(T = 0))^2}\hat{\sigma} \tag{C.15}$$

Under these transformations, the current density and magnetic field scale as:

$$J = \frac{\sqrt{2}B_{\mathrm{c}}(T = 0)}{\mu_0\lambda(T = 0)}\hat{J} \tag{C.16}$$

$$B = \left(\sqrt{2}B_{\mathrm{c}}(T = 0)\right)\hat{B} \tag{C.17}$$

Substituting these changes of variables into the TDGL equations (Eqs. 3.21 and 3.22), we obtain their dimensionless form:

$$\left(1 + \frac{T}{T_c}\right)\left(1 + \left(\frac{T}{T_{\mathrm{c}}}\right)^2\right)\frac{\partial\hat{\psi}}{\partial\hat{t}} = -\left(\frac{i}{\kappa}\hat{\nabla} + \left(1 + \left(\frac{T}{T_{\mathrm{c}}}\right)^2\right)\hat{A}\right)^2\hat{\psi} + \left(1 - \left(\frac{T}{T_{\mathrm{c}}}\right)^4\right)\hat{\psi} - |\hat{\psi}|^2\hat{\psi} \tag{C.18}$$

$$\hat{\sigma}\frac{\partial \hat{A}}{\partial \hat{t}} = -\frac{i}{2\kappa}\frac{1}{1+\left(\frac{T}{T_c}\right)^2}\left(\hat{\psi}^*\hat{\nabla}\hat{\psi} - \hat{\psi}\hat{\nabla}\hat{\psi}^*\right) - |\hat{\psi}|^2\hat{A} - \hat{\nabla}\times\hat{\nabla}\times\hat{A} \tag{C.19}$$

Note that the dimensional factor for length is temperature-dependent in the ˜ transformation, where $x = \lambda(T)\tilde{x}$, and temperature-independent in the ˆ transformation, where $x = \lambda(T=0)\hat{x}$.

The superconducting domain in toy models contains local defects, such as pinning sites. Consider a pinning site with a radius of 20 nm. Under the ˜ transformation, its dimensionless radius is given by

$$\tilde{r}_{\text{defect}} = \frac{20\text{ nm}}{\lambda(T)}, \tag{C.20}$$

which depends on temperature. In contrast, under the ˆ transformation, the defect size is expressed as

$$\hat{r}_{\text{defect}} = \frac{20\text{ nm}}{\lambda(T=0)}, \tag{C.21}$$

which remains temperature-independent.

In Chapter 6, we investigate trapped vortices in superconductors. In these simulations, vortices are introduced at a low temperature, and the temperature is gradually increased during the TDGL simulation to determine whether a vortex depins at higher temperatures. Since temperature evolves over time, $\tilde{r}_{\text{defect}}$ varies throughout the simulation, which complicates interpretation. In contrast, the ˆ transformation ensures that the defect size, $\hat{r}_{\text{defect}}$, remains constant, making it a more convenient choice for this scenario.

Beyond the two transformations used in this work, other conventions for dimensionless TDGL equations exist. In particular, some formulations define length in units of the finite-temperature coherence length $\xi(T)$ [75, 83], while others use the zero-temperature coherence length $\xi(T=0)$ [77, 79, 82].

Appendix D: Implementation of TDGL Simulations in COMSOL Multiphysics

In this Appendix, we present the implementation of TDGL simulations in COMSOL Multiphysics. Here, we adopt the ˜ transformation as presented in Sec. C.1.

In COMSOL, we express the order parameter and electromagnetic field as

$$\tilde{\psi} \equiv v_1 + iv_2, \tag{D.1}$$

$$\tilde{A} = \tilde{A}_{\mathrm{SC}} + \tilde{A}_{\mathrm{dp}} = (u_1\hat{x} + u_2\hat{y} + u_3\hat{z}) + (A_{\mathrm{dp},1}\hat{x} + A_{\mathrm{dp},2}\hat{y} + A_{\mathrm{dp},3}\hat{z}). \tag{D.2}$$

Since the electromagnetic field generated by the magnetic dipole ($\tilde{A}_{\mathrm{dp}}$) is known, the variables to be solved in COMSOL are v_1, v_2, u_1, u_2, u_3 (i.e., $\tilde{\psi}$ and $\tilde{A}_{\mathrm{SC}}$).

Rewriting the first TDGL equation (Eq. C.8) in terms of v_1 and v_2, we obtain:

$$\frac{\partial v_1}{\partial \tilde{t}} = \frac{1}{\kappa^2}\tilde{\nabla}^2 v_1 + \frac{2}{\kappa}\tilde{A}\cdot(\tilde{\nabla}v_2) + \frac{1}{\kappa}(\tilde{\nabla}\cdot\tilde{A})v_2 - \tilde{A}^2 v_1 + v_1 - (v_1^2 + v_2^2)v_1, \tag{D.3}$$

$$\frac{\partial v_2}{\partial \tilde{t}} = \frac{1}{\kappa^2}\tilde{\nabla}^2 v_2 - \frac{2}{\kappa}\tilde{A}\cdot(\tilde{\nabla}v_1) - \frac{1}{\kappa}(\tilde{\nabla}\cdot\tilde{A})v_1 - \tilde{A}^2 v_2 + v_2 - (v_1^2 + v_2^2)v_2. \tag{D.4}$$

The second TDGL equation (Eq. C.9) takes the form:

$$\tilde{\sigma}\frac{\partial \tilde{A}}{\partial \tilde{t}} = \frac{1}{\kappa}(v_1\tilde{\nabla}v_2 - v_2\tilde{\nabla}v_1) - (v_1^2 + v_2^2)\tilde{A} - \tilde{\nabla}\times\tilde{\nabla}\times\tilde{A}_{\mathrm{SC}}. \tag{D.5}$$

Recall that $\tilde{\nabla} \times \tilde{\nabla} \times \tilde{A}_{\mathrm{dp}} = \tilde{\nabla} \times \tilde{B}_{\mathrm{dp}} = 0$ inside the superconductor.

In COMSOL, we use the General Form PDE to implement the TDGL simulations, which is given by:

$$e_a \frac{\partial^2 u}{\partial \tilde{t}^2} + d_a \frac{\partial u}{\partial \tilde{t}} + \tilde{\nabla} \cdot \Gamma = f. \tag{D.6}$$

The first TDGL equation in the format of the General Form PDE (Eq. D.6) becomes:

$$u = \begin{pmatrix} v_1 \\ \\ v_2 \end{pmatrix}, \quad e_a = \begin{pmatrix} 0 & 0 \\ \\ 0 & 0 \end{pmatrix}, \quad d_a = \begin{pmatrix} 1 & 0 \\ \\ 0 & 1 \end{pmatrix}. \tag{D.7}$$

The flux term Γ is given by:

$$\Gamma = \begin{pmatrix} -\frac{1}{\kappa^2}\partial_x v_1 & -\frac{1}{\kappa^2}\partial_y v_1 & -\frac{1}{\kappa^2}\partial_z v_1 \\ \\ -\frac{1}{\kappa^2}\partial_x v_2 & -\frac{1}{\kappa^2}\partial_y v_2 & -\frac{1}{\kappa^2}\partial_z v_2 \end{pmatrix}. \tag{D.8}$$

The source term f consists of three components:

$$f = f_1 + f_2 + f_3, \tag{D.9}$$

where

$$f_1 = \begin{pmatrix} \frac{2}{\kappa}\left[(u_1 + A_{\mathrm{dp},1})\partial_x v_2 + (u_2 + A_{\mathrm{dp},2})\partial_y v_2 + (u_3 + A_{\mathrm{dp},3})\partial_z v_2\right] \\ \\ -\frac{2}{\kappa}\left[(u_1 + A_{\mathrm{dp},1})\partial_x v_1 + (u_2 + A_{\mathrm{dp},2})\partial_y v_1 + (u_3 + A_{\mathrm{dp},3})\partial_z v_1\right] \end{pmatrix}. \tag{D.10}$$

$$f_2 = \begin{pmatrix} \frac{1}{\kappa}\left[(\partial_x u_1 + \partial_y u_2 + \partial_z u_3) + (\partial_x A_{\mathrm{dp},1} + \partial_y A_{\mathrm{dp},2} + \partial_z A_{\mathrm{dp},3})\right] v_2 \\ \\ \frac{-1}{\kappa}\left[(\partial_x u_1 + \partial_y u_2 + \partial_z u_3) + (\partial_x A_{\mathrm{dp},1} + \partial_y A_{\mathrm{dp},2} + \partial_z A_{\mathrm{dp},3})\right] v_1 \end{pmatrix} \tag{D.11}$$

$$f_3 = \begin{pmatrix} -\left[(u_1 + A_{\mathrm{dp},1})^2 + (u_2 + A_{\mathrm{dp},2})^2 + (u_3 + A_{\mathrm{dp},3})^2\right] v_1 + v_1 - (v_1^2 + v_2^2) v_1 \\ -\left[(u_1 + A_{\mathrm{dp},1})^2 + (u_2 + A_{\mathrm{dp},2})^2 + (u_3 + A_{\mathrm{dp},3})^2\right] v_2 + v_2 - (v_1^2 + v_2^2) v_2 \end{pmatrix} \tag{D.12}$$

The second TDGL equation can be rewritten as

$$\tilde{\sigma} \frac{\partial \tilde{A}_{\mathrm{SC}}}{\partial \tilde{t}} + \tilde{\nabla} \times \tilde{\nabla} \times \tilde{A}_{\mathrm{SC}} = -\tilde{\sigma} \frac{\partial \tilde{A}_{\mathrm{dp}}}{\partial \tilde{t}} + \frac{1}{\kappa} (v_1 \tilde{\nabla} v_2 - v_2 \tilde{\nabla} v_1) - (v_1^2 + v_2^2) \tilde{A}. \tag{D.13}$$

The second TDGL equation in the format of the General Form PDE (Eq. D.6) becomes:

$$u = \begin{pmatrix} u_1 \\ u_2 \\ u_3 \end{pmatrix}, \tag{D.14}$$

$$e_a = \begin{pmatrix} 0 & 0 & 0 \\ 0 & 0 & 0 \\ 0 & 0 & 0 \end{pmatrix}, \tag{D.15}$$

$$d_a = (\text{SC domain}) * \begin{pmatrix} \tilde{\sigma} & 0 & 0 \\ 0 & \tilde{\sigma} & 0 \\ 0 & 0 & \tilde{\sigma} \end{pmatrix}. \tag{D.16}$$

Here, (SC domain) is an indicator function that takes the value 1 inside the superconducting

domain and 0 in the vacuum domain. The flux term Γ is given by

$$\Gamma = \begin{pmatrix} 0 & \partial_x u_2 - \partial_y u_1 & \partial_x u_3 - \partial_z u_1 \\ \partial_y u_1 - \partial_x u_2 & 0 & \partial_y u_3 - \partial_z u_2 \\ \partial_z u_1 - \partial_x u_3 & \partial_z u_2 - \partial_y u_3 & 0 \end{pmatrix}. \tag{D.17}$$

The source term f is

$$f = (\text{SC domain}) * \begin{pmatrix} -\tilde{\sigma}\frac{\partial A_{\mathrm{dp},1}}{\partial \tilde{t}} + \frac{1}{\kappa}(v_1\partial_x v_2 - v_2\partial_x v_1) - (v_1^2 + v_2^2)(u_1 + A_{\mathrm{dp},1}) \\ -\tilde{\sigma}\frac{\partial A_{\mathrm{dp},2}}{\partial \tilde{t}} + \frac{1}{\kappa}(v_1\partial_y v_2 - v_2\partial_y v_1) - (v_1^2 + v_2^2)(u_2 + A_{\mathrm{dp},2}) \\ -\tilde{\sigma}\frac{\partial A_{\mathrm{dp},3}}{\partial \tilde{t}} + \frac{1}{\kappa}(v_1\partial_z v_2 - v_2\partial_z v_1) - (v_1^2 + v_2^2)(u_3 + A_{\mathrm{dp},3}) \end{pmatrix}. \tag{D.18}$$

Appendix E: Third-Harmonic Response Measurements of Two Nb_3Sn Films

E.1 Introduction

Nb_3Sn is a promising alternative to bulk Nb for SRF cavity applications due to its higher superconducting transition temperature ($T_c \approx 18.3$ K) and lower BCS surface resistance at a given temperature, allowing operation at higher temperatures than Nb [81, 106, 115, 140–143, 215, 216]. Fabricated through the vapor diffusion process, Nb_3Sn films have demonstrated the ability to sustain high accelerating gradients without being limited by the lower critical field B_{c1}, addressing historical concerns of flux penetration. While challenges remain, such as mitigating the Q-slope and optimizing deposition methods, Nb_3Sn continues to be a leading candidate for next-generation SRF accelerator technology.

In this work, we investigate two Nb_3Sn films: one deposited using the traditional vapor diffusion process (vapor-diffused Nb_3Sn film) and the other synthesized through an electrochemical plating process followed by thermal annealing (Sn-plated Nb_3Sn film). Both films were fabricated by our collaborators at Cornell University, including Matthias Liepe, Zeming Sun, and Thomas Oseroff. Details on the deposition methods, surface roughness, local stoichiometry, and other characteristics of these films can be found in Refs. [217, 218].

Similar to the seven Nb/Cu films studied in Chapter 5, localized third-harmonic response measurements of both Nb_3Sn films reveal signals associated with surface defects below their

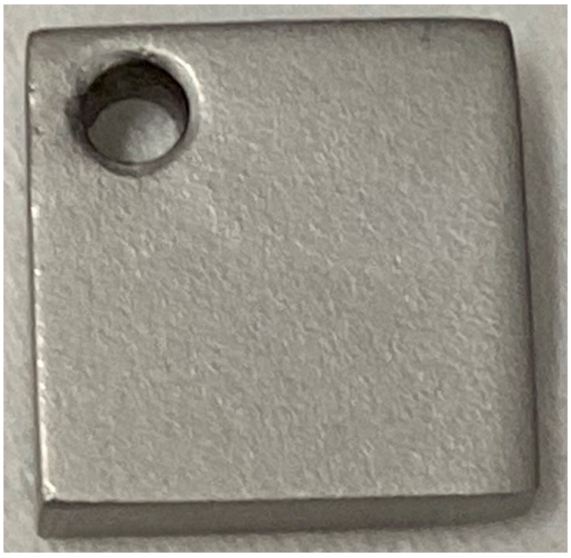

Figure E.1: Photo of the vapor-diffused Nb_3Sn film. The sample, prepared at Cornell University, has dimensions of 1 cm $\times$ 1 cm.

superconducting transition temperature, $T_c \approx 18.3$ K.

E.2 Sample Information for the Two Nb_3Sn Films

Figure E.1 shows a photograph of the vapor-diffused Nb_3Sn film used in this study. The film has a thickness of 2 μm and is grown on a 3 mm thick Nb substrate. The sample has dimensions of 1 cm $\times$ 1 cm.

Figure E.2 shows a photograph of the Sn-plated Nb_3Sn film used in this study. The film has a thickness of 2.4 μm and is grown on a 3 mm thick Nb substrate. The sample has dimensions of 1 cm $\times$ 1 cm.

Third-harmonic response measurements were performed on the Sn-plated Nb_3Sn film multiple times. The data presented in this appendix were obtained during the early-stage measurements. In a later measurement, the microscope probe was pressed too hard against

Figure E.2: Photo of the Sn-plated Nb_3Sn film. The sample, prepared at Cornell University, has dimensions of 1 cm $\times$ 1 cm. The red dashed circle highlights a scar on the surface caused by an aggressive probe contact during a later measurement.

the sample surface, leaving a visible scar, as indicated by the red dashed circle in Fig. E.2.

One of the primary motivations for developing the deposition recipe for the Sn-plated Nb_3Sn film is to achieve a smoother surface. The average surface roughness (R_a) of a typical vapor-diffused Nb_3Sn film is approximately 300 nm, whereas that of a typical Sn-plated Nb_3Sn film is significantly lower, around 60 nm [217, 218].

E.3 Experimental Results for the Vapor-Diffused Nb_3Sn Film

Figure E.3 shows the measured linear power scale third-harmonic response $P_{3f}(T)$ at a fixed location on the vapor-diffused Nb_3Sn film for six different input powers. The input frequency is 2.08 GHz, and the probe background has been subtracted. The input power levels shown in Fig. E.3 are not evenly spaced in power but rather in rf field amplitude. Note that the input power is proportional to the square of the rf field amplitude.

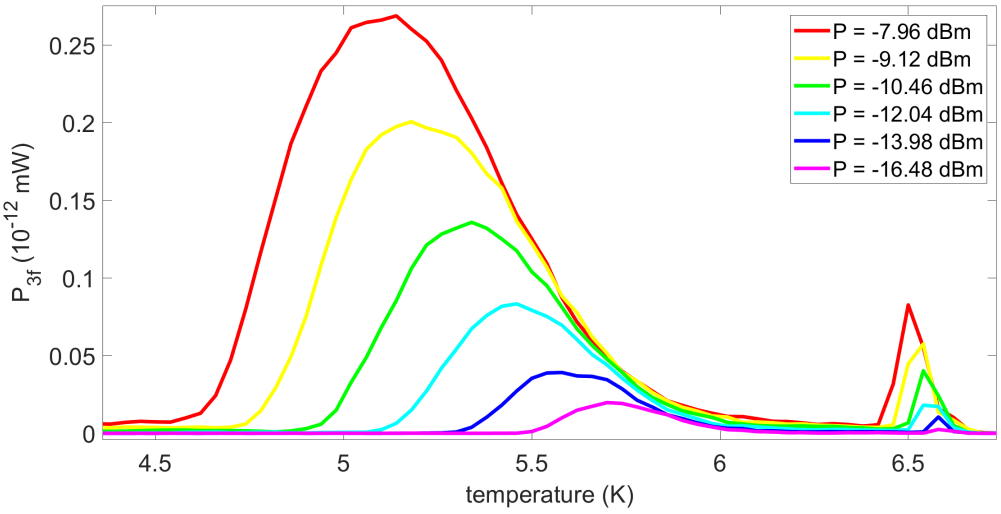

Figure E.3: Measured linear power scale $P_{3f}(T)$ from strong (red) to weak (purple) input power for the vapor-diffused Nb_3Sn film at an input frequency of 2.08 GHz. The probe background has been subtracted.

Two distinct nontrivial structures are observed in Fig. E.3: one shows $T_c^{P_{3f}} = 6.2$ K, and the other shows $T_c^{P_{3f}} = 6.7$ K. Both $P_{3f}(T)$ structures exhibit the four key features identified in Sec. 4.4 (TDGL simulation). Consequently, they are likely associated with rf vortex nucleation by surface defects.

In addition to measuring $P_{3f}(T)$ with a fine temperature step size over a limited temperature and input power range—focusing on the nontrivial P_{3f} structures below 7 K—we also perform measurements over a broader range of temperature and input power. The measurement spans temperatures from 3.5 K to 20 K, extending beyond T_c, and input powers from -40 dBm to +5 dBm. Within this broader range, no additional nontrivial $P_{3f}(T)$ structures are observed beyond the two identified in Fig. E.3.

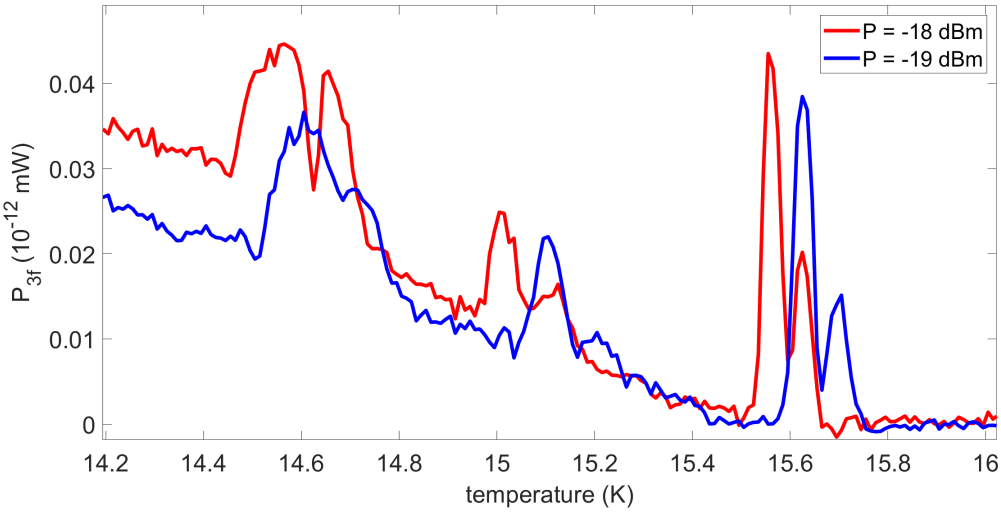

Figure E.4: Measured linear power scale $P_{3f}(T)$ for the Sn-plated Nb_3Sn film at an input frequency of 1.21 GHz. Data are shown for two different input powers: $P = -18$ dBm (red) and $P = -19$ dBm (blue). The probe background has been subtracted.

E.4 Experimental Results for the Sn-Plated Nb_3Sn Film

Figure E.4 shows the measured linear power scale third-harmonic response $P_{3f}(T)$ at a fixed location on the Sn-plated Nb_3Sn film for two different input powers. The input frequency is 1.21 GHz, and the probe background has been subtracted.

Three distinct nontrivial structures are observed in Fig. E.4: one around 15.6 K, another around 15.1 K, and a third around 14.6 K. All three $P_{3f}(T)$ structures exhibit the four key features identified in Sec. 4.4 (TDGL simulation). Consequently, they are likely associated with rf vortex nucleation by surface defects.

In addition to measuring $P_{3f}(T)$ with a fine temperature step size over a limited temperature and input power range—focusing on the nontrivial P_{3f} structures between 14 K and 16 K—we also perform measurements over a broader range of temperature and input power, as shown in Fig. E.5. Figure E.5 presents the measured log power scale (dBm) P_{3f} as a function of temperature

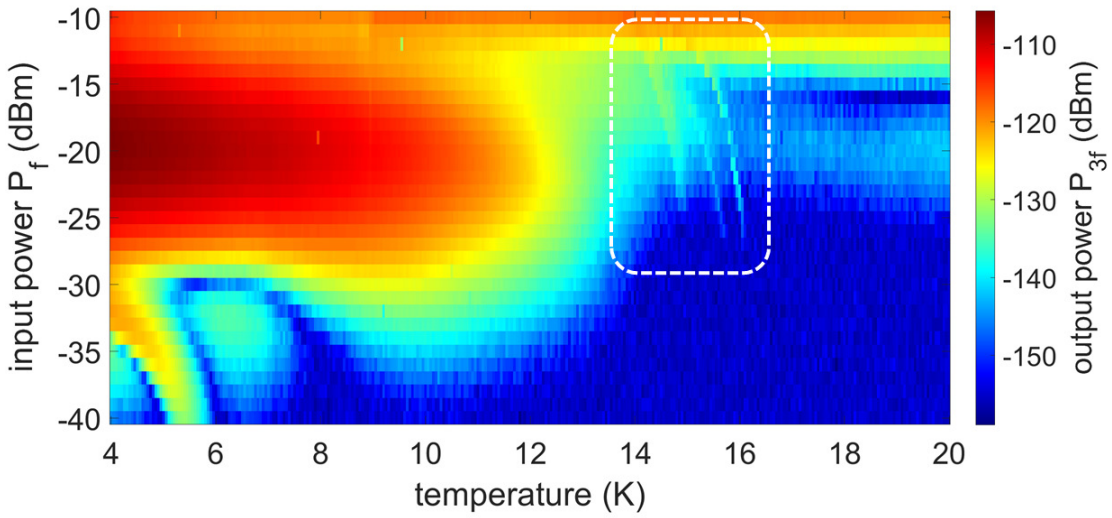

Figure E.5: Color map of the measured log power scale P_{3f} as a function of temperature T and input power P_f for the Sn-plated Nb_3Sn film. The input frequency is 1.21 GHz. The probe background is not subtracted. The dashed box highlights the region containing the three nontrivial $P_{3f}(T)$ structures, whose details are shown in Fig. E.4.

T and input power P_f for the Sn-plated Nb_3Sn film. The input frequency is 1.21 GHz. The probe background is not subtracted. The measurement spans temperatures from 4 K to 20 K, extending beyond T_c, and input powers from -40 dBm to -10 dBm.

As described in the four key features identified in Sec. 4.4 through TDGL simulations, the nontrivial $P_{3f}(T)$ structures associated with rf vortex nucleation by surface defects shift to lower temperatures as the rf field amplitude increases. In a P_{3f} color map such as Fig. E.5, where the horizontal axis represents temperature and the vertical axis represents input power, this trend appears as a structure with a negative slope.

The dashed box in Fig. E.5 highlights the region containing the three nontrivial $P_{3f}(T)$ structures observed between 14 K and 16 K, whose details are shown in Fig. E.4. In addition to these three structures, another distinct $P_{3f}(T)$ feature exhibiting a clear negative slope is visible in the lower left corner of Fig. E.5, with a $T_c^{P_{3f}}$ around 6 K. Given the observed negative slope trend,

all four $P_{3f}(T)$ structures are likely associated with rf vortex nucleation by surface defects.

The strongest P_{3f} signal in Fig. E.5, represented by the large red region below 12 K, does not exhibit a negative slope trend. This suggests that it may originate from a nonlinear mechanism distinct from rf vortex nucleation by surface defects.

E.5 Conclusion

Third-harmonic response measurements of both the vapor-diffused and Sn-plated Nb_3Sn films reveal the presence of surface defects that give rise to nontrivial $P_{3f}(T)$ structures. A key similarity between the two films is that these structures exhibit a $T_c^{P_{3f}}$ below the superconducting transition temperature ($T_c \approx 18.3$ K) and display the four key features identified in Sec. 4.4 through TDGL simulations. These characteristics are consistent with rf vortex nucleation by surface defects.

Despite differences in deposition methods and surface roughness, the observed nonlinear response in both films suggests that rf vortex nucleation by surface defects is a robust phenomenon across different Nb_3Sn growth techniques. This highlights the importance of defect engineering in optimizing Nb_3Sn films for SRF applications.

Bibliography

[1] Michael Tinkham. *Introduction to superconductivity*. Dover Publications, Mineola, NY, 2004.

[2] J. Bardeen, L. N. Cooper, and J. R. Schrieffer. Theory of superconductivity. *Phys. Rev.*, 108:1175–1204, Dec 1957.

[3] Vitaly L Ginzburg, Vitaly Lazarevich Ginzburg, and LD Landau. *On the theory of superconductivity*. Springer, 2009.

[4] Steven M. Anlage. Microwave superconductivity. *IEEE Journal of Microwaves*, 1(1):389–402, 2021.

[5] Hasan Padamsee. 50 years of success for SRF accelerators—a review. *Superconductor science and technology*, 30(5):053003, 2017.

[6] Chung-Yang Wang, Carlota Pereira, Stewart Leith, Guillaume Rosaz, and Steven M. Anlage. Microscopic examination of rf-cavity-quality niobium films through local nonlinear microwave response. *Physical Review Applied*, 22:054010, Nov 2024.

[7] Chung-Yang Wang and Steven M. Anlage. Microwave microscope studies of trapped vortex dynamics in superconductors. *arXiv preprint arXiv:2503.02811*, 2025.

[8] Sheng-Chiang Lee, Su-Young Lee, and Steven M. Anlage. Microwave nonlinearities of an isolated long YBa2Cu3O7$-\delta$ bicrystal grain boundary. *Physical Review B*, 72(2):024527, 2005.

[9] Dragos I. Mircea, Hua Xu, and Steven M. Anlage. Phase-sensitive harmonic measurements of microwave nonlinearities in cuprate thin films. *Physical Review B*, 80(14):144505, 2009.

[10] Tamin Tai, Behnood G. Ghamsari, Tom Bieler, and Steven M. Anlage. Nanoscale nonlinear radio frequency properties of bulk Nb: Origins of extrinsic nonlinear effects. *Physical Review B*, 92(13):134513, 2015.

[11] Bakhrom Oripov, Thomas Bieler, Gianluigi Ciovati, Sergio Calatroni, Pashupati Dhakal, Tobias Junginger, Oleg B. Malyshev, Giovanni Terenziani, Anne-Marie Valente-Feliciano, Reza Valizadeh, et al. High-frequency nonlinear response of superconducting cavity-grade Nb surfaces. *Physical Review Applied*, 11(6):064030, 2019.

[12] Bakhrom Oripov and Steven M. Anlage. Time-dependent Ginzburg-Landau treatment of rf magnetic vortices in superconductors: Vortex semiloops in a spatially nonuniform magnetic field. *Physical Review E*, 101(3):033306, 2020.

[13] Carson Jeffries, Q. Harry Lam, Youngtae Kim, L. C. Bourne, and A. Zettl. Symmetry breaking and nonlinear electrodynamics in the ceramic superconductor YBa2Cu3O7. *Phys. Rev. B*, 37:9840–9843, Jun 1988.

[14] L. Ji, R. H. Sohn, G. C. Spalding, C. J. Lobb, and M. Tinkham. Critical-state model for harmonic generation in high-temperature superconductors. *Phys. Rev. B*, 40:10936–10945, Dec 1989.

[15] K.-H. Müller, J.C. Macfarlane, and R. Driver. Nonlinear magnetic flux response in high temperature superconductors. *Physica C: Superconductivity and its Applications*, 158(3):366–370, 1989.

[16] C. D. Jeffries, Q. H. Lam, Y. Kim, C. M. Kim, A. Zettl, and M. P. Klein. Nonlinear electrodynamics in the granular superconductor YBa2Cu3O7: Experiments and interpretation. *Phys. Rev. B*, 39:11526–11537, Jun 1989.

[17] T. Ishida and R. B. Goldfarb. Fundamental and harmonic susceptibilities of YBa2Cu3O7$-\delta$. *Phys. Rev. B*, 41:8937–8948, May 1990.

[18] K. Yamamoto, H. Mazaki, H. Yasuoka, S. Katsuyama, and K. Kosuge. Harmonic susceptibilities of a sintered oxide superconductor. *Phys. Rev. B*, 46:1122–1129, Jul 1992.

[19] S. Shatz, A. Shaulov, and Y. Yeshurun. Universal behavior of harmonic susceptibilities in type-II superconductors. *Phys. Rev. B*, 48:13871–13880, Nov 1993.

[20] Alan M Portis. *Electrodynamics of high-temperature superconductors*, volume 48. World Scientific, 1993.

[21] T B Samoilova. Non-linear microwave effects in thin superconducting films. *Superconductor Science and Technology*, 8(5):259, may 1995.

[22] Daniel E. Oates. *Nonlinear Behavior of Superconducting Devices*, pages 117–148. Springer Netherlands, Dordrecht, 2001.

[23] Sheng-Chiang Lee, C.P. Vlahacos, B.J. Feenstra, Andrew Schwartz, D.E. Steinhauer, F.C. Wellstood, and Steven M. Anlage. Magnetic permeability imaging of metals with a scanning near-field microwave microscope. *Applied Physics Letters*, 77(26):4404–4406, 2000.

[24] Sheng-Chiang Lee and Steven M. Anlage. Spatially-resolved nonlinearity measurements of YBa2Cu3O7$-\delta$ bicrystal grain boundaries. *Applied physics letters*, 82(12):1893–1895, 2003.

[25] Sheng-Chiang Lee, Mathew Sullivan, Gregory R. Ruchti, Steven M. Anlage, Benjamin S. Palmer, B. Maiorov, and E. Osquiguil. Doping-dependent nonlinear Meissner effect and spontaneous currents in high-Tc superconductors. *Physical Review B*, 71(1):014507, 2005.

[26] A V Velichko, M J Lancaster, and A Porch. Nonlinear microwave properties of high Tc thin films. *Superconductor Science and Technology*, 18(3):R24, jan 2005.

[27] Tamin Tai, X. X. Xi, C.G. Zhuang, Dragos I. Mircea, and Steven M. Anlage. Nonlinear near-field microwave microscope for RF defect localization in superconductors. *IEEE transactions on applied superconductivity*, 21(3):2615–2618, 2011.

[28] Tamin Tai, Behnood G. Ghamsari, and Steven M. Anlage. Nanoscale electrodynamic response of Nb superconductors. *IEEE Transactions on Applied Superconductivity*, 23(3):7100104–7100104, 2012.

[29] Tamin Tai, Behnood G. Ghamsari, Thomas R. Bieler, Teng Tan, X. X. Xi, and Steven M. Anlage. Near-field microwave magnetic nanoscopy of superconducting radio frequency cavity materials. *Applied Physics Letters*, 104(23):232603, 2014.

[30] Tamin Tai, B.G. Ghamsari, and Steven M. Anlage. Modeling the nanoscale linear response of superconducting thin films measured by a scanning probe microwave microscope. *Journal of Applied Physics*, 115(20):203908, 2014.

[31] D. E. Oates, S.-H. Park, and G. Koren. Observation of the nonlinear meissner effect in YBCO thin films: Evidence for a d-wave order parameter in the bulk of the cuprate superconductors. *Phys. Rev. Lett.*, 93:197001, Nov 2004.

[32] Alexander P. Zhuravel, B. G. Ghamsari, C. Kurter, P. Jung, S. Remillard, J. Abrahams, A. V. Lukashenko, Alexey V. Ustinov, and Steven M. Anlage. Imaging the anisotropic nonlinear meissner effect in nodal YBa2Cu3O7$-\delta$ thin-film superconductors. *Phys. Rev. Lett.*, 110:087002, Feb 2013.

[33] Sachiko Nakamura, Kota Katsumi, Hirotaka Terai, and Ryo Shimano. Nonreciprocal terahertz second-harmonic generation in superconducting NbN under supercurrent injection. *Phys. Rev. Lett.*, 125:097004, Aug 2020.

[34] Yu He, Zifeng Wang, Jiaxu Li, Fenglin Zhong, Haozhe Yang, Kewen Shi, Le Wang, Guang Yang, and Weisheng Zhao. Geometric asymmetry-enhanced nonreciprocal supercurrent transport revealed by second-harmonic response. *arXiv preprint arXiv:2503.03441*, 2025.

[35] B.W. Langley, S. M. Anlage, R. F. W. Pease, and M. R. Beasley. Magnetic penetration depth measurements of superconducting thin films by a microstrip resonator technique. *Review of Scientific Instruments*, 62(7):1801–1812, 07 1991.

[36] Seokjin Bae, Seunghun Lee, Xiaohang Zhang, Ichiro Takeuchi, and Steven M. Anlage. Microwave Meissner screening properties of proximity-coupled topological-insulator / superconductor bilayers. *Phys. Rev. Mater.*, 3:124803, Dec 2019.

[37] M Golosovsky, M Tsindlekht, and D Davidov. High-frequency vortex dynamics in YBa2Cu3O7. *Superconductor Science and Technology*, 9(1):1, Jan 1996.

[38] Enrico Silva, Nicola Pompeo, and Oleksandr V. Dobrovolskiy. Vortices at microwave frequencies. *Physical Sciences Reviews*, 2(10):20178004, 2017.

[39] Steven M. Anlage, D. E. Steinhauer, B. J. Feenstra, C. P. Vlahacos, and F. C. Wellstood. *Near-Field Microwave Microscopy of Materials Properties*, pages 239–269. Springer Netherlands, Dordrecht, 2001.

[40] S. M. Anlage, V. V. Talanov, and A. R. Schwartz. *Principles of Near-Field Microwave Microscopy*, volume 1, pages 215–253. Springer-Verlag, New York, 2007.

[41] Werner A. Hofer, Adam S. Foster, and Alexander L. Shluger. Theories of scanning probe microscopes at the atomic scale. *Rev. Mod. Phys.*, 75:1287–1331, Oct 2003.

[42] Ke Bian, Christoph Gerber, Andreas J Heinrich, Daniel J Müller, Simon Scheuring, and Ying Jiang. Scanning probe microscopy. *Nature Reviews Methods Primers*, 1(1):36, 2021.

[43] Mark E Barber, Eric Yue Ma, and Zhi-Xun Shen. Microwave impedance microscopy and its application to quantum materials. *Nature Reviews Physics*, 4(1):61–74, 2022.

[44] Keji Lai, Worasom Kundhikanjana, Michael A. Kelly, Zhi-Xun Shen, Javad Shabani, and Mansour Shayegan. Imaging of Coulomb-driven quantum Hall edge states. *Phys. Rev. Lett.*, 107:176809, Oct 2011.

[45] Xiaoyu Wu, Zhenqi Hao, Di Wu, Lu Zheng, Zhanzhi Jiang, Vishal Ganesan, Yayu Wang, and Keji Lai. Quantitative measurements of nanoscale permittivity and conductivity using tuning-fork-based microwave impedance microscopy. *Review of Scientific Instruments*, 89(4):043704, 04 2018.

[46] Monica Allen, Yongtao Cui, Eric Yue Ma, Masataka Mogi, Minoru Kawamura, Ion Cosma Fulga, David Goldhaber-Gordon, Yoshinori Tokura, and Zhi-Xun Shen. Visualization of an axion insulating state at the transition between 2 chiral quantum anomalous Hall states. *Proceedings of the National Academy of Sciences*, 116(29):14511–14515, 2019.

[47] Zhaodong Chu, Emma C. Regan, Xuejian Ma, Danqing Wang, Zifan Xu, M. Iqbal Bakti Utama, Kentaro Yumigeta, Mark Blei, Kenji Watanabe, Takashi Taniguchi, Sefaattin Tongay, Feng Wang, and Keji Lai. Nanoscale conductivity imaging of correlated electronic states in $\mathrm{wse_2/ws_2}$ moiré superlattices. *Phys. Rev. Lett.*, 125:186803, Oct 2020.

[48] Leonard Weihao Cao, Chen Wu, Rajarshi Bhattacharyya, Ruolun Zhang, and Monica T. Allen. Millikelvin microwave impedance microscopy in a dry dilution refrigerator. *Review of Scientific Instruments*, 94(9):093705, 09 2023.

[49] M Tabib-Azar, N S Shoemaker, and S Harris. Non-destructive characterization of materials by evanescent microwaves. *Measurement Science and Technology*, 4(5):583, may 1993.

[50] C. P. Vlahacos, R. C. Black, S. M. Anlage, A. Amar, and F. C. Wellstood. Near-field scanning microwave microscope with 100 μm resolution. *Applied Physics Letters*, 69(21):3272–3274, 11 1996.

[51] D. E. Steinhauer, C. P. Vlahacos, S. K. Dutta, F. C. Wellstood, and Steven M. Anlage. Surface resistance imaging with a scanning near-field microwave microscope. *Applied Physics Letters*, 71(12):1736–1738, 09 1997.

[52] D. E. Steinhauer, C. P. Vlahacos, S. K. Dutta, B. J. Feenstra, F. C. Wellstood, and Steven M. Anlage. Quantitative imaging of sheet resistance with a scanning near-field microwave microscope. *Applied Physics Letters*, 72(7):861–863, 02 1998.

[53] C. P. Vlahacos, D. E. Steinhauer, S. K. Dutta, B. J. Feenstra, Steven M. Anlage, and F. C. Wellstood. Quantitative topographic imaging using a near-field scanning microwave microscope. *Applied Physics Letters*, 72(14):1778–1780, 04 1998.

[54] M. Tabib-Azar, P. S. Pathak, G. Ponchak, and S. LeClair. Nondestructive superresolution imaging of defects and nonuniformities in metals, semiconductors, dielectrics, composites, and plants using evanescent microwaves. *Review of Scientific Instruments*, 70(6):2783–2792, 06 1999.

[55] S.M. Anlage, D.E. Steinhauer, C.P. Vlahacos, B.J. Feenstra, A.S. Thanawalla, Wensheng Hu, S.K. Dutta, and F.C. Wellstood. Superconducting material diagnostics using a scanning near-field microwave microscope. *IEEE Transactions on Applied Superconductivity*, 9(2):4127–4132, 1999.

[56] D. E. Steinhauer, C. P. Vlahacos, F. C. Wellstood, Steven M. Anlage, C. Canedy, R. Ramesh, A. Stanishevsky, and J. Melngailis. Quantitative imaging of dielectric permittivity and tunability with a near-field scanning microwave microscope. *Review of Scientific Instruments*, 71(7):2751–2758, 07 2000.

[57] Björn T. Rosner and Daniel W. van der Weide. High-frequency near-field microscopy. *Review of Scientific Instruments*, 73(7):2505–2525, 07 2002.

[58] Atif Imtiaz and Steven M. Anlage. A novel STM-assisted microwave microscope with capacitance and loss imaging capability. *Ultramicroscopy*, 94(3):209–216, 2003.

[59] Alexander Tselev, Steven M. Anlage, Hans M. Christen, Robert L. Moreland, Vladimir V. Talanov, and Andrew R. Schwartz. Near-field microwave microscope with improved sensitivity and spatial resolution. *Review of Scientific Instruments*, 74(6):3167–3170, 06 2003.

[60] Atif Imtiaz, Marc Pollak, Steven M. Anlage, John D. Barry, and John Melngailis. Near-field microwave microscopy on nanometer length scales. *Journal of Applied Physics*, 97(4):044302, 01 2005.

[61] Atif Imtiaz and Steven M. Anlage. Effect of tip geometry on contrast and spatial resolution of the near-field microwave microscope. *Journal of Applied Physics*, 100(4):044304, 08 2006.

[62] Atif Imtiaz, Steven M. Anlage, John D. Barry, and John Melngailis. Nanometer-scale material contrast imaging with a near-field microwave microscope. *Applied Physics Letters*, 90(14):143106, 04 2007.

[63] Alexander Tselev, Steven M. Anlage, Zhengkun Ma, and John Melngailis. Broadband dielectric microwave microscopy on micron length scales. *Review of Scientific Instruments*, 78(4):044701, 04 2007.

[64] S.M. Anlage, C.P. Vlahacos, S. Dutta, and F.C. Wellstood. Scanning microwave microscopy of active superconducting microwave devices. *IEEE Transactions on Applied Superconductivity*, 7(2):3686–3689, 1997.

[65] Ashfaq S. Thanawalla, S. K. Dutta, C. P. Vlahacos, D. E. Steinhauer, B. J. Feenstra, Steven M. Anlage, F. C. Wellstood, and Robert B. Hammond. Microwave near-field imaging of electric fields in a superconducting microstrip resonator. *Applied Physics Letters*, 73(17):2491–2493, 10 1998.

[66] Wensheng Hu, A. S. Thanawalla, B. J. Feenstra, F. C. Wellstood, and Steven M. Anlage. Imaging of microwave intermodulation fields in a superconducting microstrip resonator. *Applied Physics Letters*, 75(18):2824–2826, 11 1999.

[67] Sheng-Chiang Lee and S.M. Anlage. Study of local nonlinear properties using a near-field microwave microscope. *IEEE Transactions on Applied Superconductivity*, 13(2):3594–3597, 2003.

[68] Bakhrom Oripov. *Superconducting radio frequency materials science through near-field magnetic microscopy*. Ph.d. thesis, University of Maryland, College Park, 2020.

[69] Chung-Yang Wang and Steven M. Anlage. Near-field nonlinear microwave microscope for fundamental superconducting studies. In *2024 IEEE/MTT-S International Microwave Symposium - IMS 2024*, pages 998–1001, 2024.

[70] Bharat Bhushan. Current status and outlook of magnetic data storage devices. *Microsystem Technologies*, 29:1529–1546, 2023.

[71] Fritz London and Heinz London. The electromagnetic equations of the supraconductor. *Proceedings of the Royal Society of London. Series A-Mathematical and Physical Sciences*, 149(866):71–88, 1935.

[72] Cornelis Jacobus Gorter and Hendrik Casimir. On supraconductivity I. *Physica*, 1(1-6):306–320, 1934.

[73] WPMR Pathirana and A Gurevich. Superheating field in superconductors with nanostructured surfaces. *Frontiers in Electronic Materials*, 3:1246016, 2023.

[74] Yusuke Kato. Charging effect on the Hall conductivity of single vortex in type II superconductors. *Journal of the Physical Society of Japan*, 68(12):3798–3801, 1999.

[75] Jennifer Deang, Qiang Du, and Max D. Gunzburger. Stochastic dynamics of Ginzburg-Landau vortices in superconductors. *Phys. Rev. B*, 64:052506, Jul 2001.

[76] Jennifer Deang, Qiang Du, and Max D. Gunzburger. Modeling and computation of random thermal fluctuations and material defects in the Ginzburg–Landau model for superconductivity. *Journal of Computational Physics*, 181(1):45–67, 2002.

[77] Alexander D. Hernández and Daniel Domínguez. Dissipation spots generated by vortex nucleation points in mesoscopic superconductors driven by microwave magnetic fields. *Physical Review B*, 77(22):224505, 2008.

[78] Antonio Lara, Farkhad G. Aliev, Alejandro V. Silhanek, and Victor V. Moshchalkov. Microwave-stimulated superconductivity due to presence of vortices. *Scientific reports*, 5(1):9187, 2015.

[79] O.V. Dobrovolskiy, C. González-Ruano, A. Lara, R. Sachser, V.M. Bevz, V.A. Shklovskij, A.I. Bezuglyj, R.V. Vovk, M. Huth, and F.G. Aliev. Moving flux quanta cool superconductors by a microwave breath. *Communications Physics*, 3(1):64, 2020.

[80] Alden R. Pack, Jared Carlson, Spencer Wadsworth, and Mark K. Transtrum. Vortex nucleation in superconductors within time-dependent Ginzburg-Landau theory in two and three dimensions: role of surface defects and material inhomogeneities. *Physical Review B*, 101(14):144504, 2020.

[81] Jared Carlson, Alden Pack, Mark K. Transtrum, Jaeyel Lee, David N. Seidman, Danilo B. Liarte, Nathan S. Sitaraman, Alen Senanian, Michelle M. Kelley, James P. Sethna, et al. Analysis of magnetic vortex dissipation in Sn-segregated boundaries in Nb3Sn superconducting RF cavities. *Physical Review B*, 103(2):024516, 2021.

[82] Qing-Yu Wang, Cun Xue, Chao Dong, and You-He Zhou. Effects of defects and surface roughness on the vortex penetration and vortex dynamics in superconductor–insulator–superconductor multilayer structures exposed to RF magnetic fields: numerical simulations within TDGL theory. *Superconductor Science and Technology*, 35(4):045004, 2022.

[83] Igor Bogush, Oleksandr V. Dobrovolskiy, and Vladimir M. Fomin. Microwave generation and vortex jets in superconductor nanotubes. *Phys. Rev. B*, 109:104516, Mar 2024.

[84] Armen Gulian. *Shortcut to superconductivity*. Springer Nature, Switzerland, 2020.

[85] Anne-Marie Valente-Feliciano. Superconducting RF materials other than bulk niobium: a review. *Superconductor Science and Technology*, 29(11):113002, 2016.

[86] A. Gurevich and G. Ciovati. Dynamics of vortex penetration, jumpwise instabilities, and nonlinear surface resistance of type-II superconductors in strong rf fields. *Phys. Rev. B*, 77:104501, Mar 2008.

[87] Kevin E. Yoon, David N. Seidman, Claire Antoine, and Pierre Bauer. Atomic-scale chemical analyses of niobium oxide/niobium interfaces via atom-probe tomography. *Applied Physics Letters*, 93(13):132502, 2008.

[88] Th Proslier, John F. Zasadzinski, L. Cooley, C. Antoine, J. Moore, J. Norem, M. Pellin, and K.E. Gray. Tunneling study of cavity grade Nb: Possible magnetic scattering at the surface. *Applied Physics Letters*, 92(21):212505, 2008.

[89] A. Romanenko and D.I. Schuster. Understanding quality factor degradation in superconducting niobium cavities at low microwave field amplitudes. *Physical Review Letters*, 119(26):264801, 2017.

[90] Guilherme Dalla Lana Semione, A. Dangwal Pandey, S. Tober, J. Pfrommer, A. Poulain, J. Drnec, G. Schütz, T.F. Keller, H. Noei, V. Vonk, et al. Niobium near-surface composition during nitrogen infusion relevant for superconducting radio-frequency cavities. *Physical Review Accelerators and Beams*, 22(10):103102, 2019.

[91] Guilherme Dalla Lana Semione, Vedran Vonk, Arti Dangwal Pandey, Elin Grånäs, Björn Arndt, Marc Wenskat, Wolfgang Hillert, Heshmat Noei, and Andreas Stierle. Temperature-dependent near-surface interstitial segregation in niobium. *Journal of Physics: Condensed Matter*, 33(26):265001, 2021.

[92] J. Halbritter. On the oxidation and on the superconductivity of niobium. *Applied Physics A*, 43(1):1–28, 1987.

[93] Warren DeSorbo. Effect of dissolved gases on some superconducting properties of niobium. *Physical Review*, 132(1):107, 1963.

[94] C.C. Koch, J.O. Scarbrough, and D.M. Kroeger. Effects of interstitial oxygen on the superconductivity of niobium. *Physical Review B*, 9(3):888, 1974.

[95] Wolfgang Weingarten. Field-dependent surface resistance for superconducting niobium accelerating cavities-condensed overview of weak superconducting defect model. *IEEE Transactions on Applied Superconductivity*, 33(4):3500309, 2023.

[96] Mingmin Wang, Anatolii Polyanskii, Shreyas Balachandran, Santosh Chetri, Martin A. Crimp, Peter J. Lee, and Thomas R. Bieler. Investigation of the effect of structural defects from hydride precipitation on superconducting properties of high purity SRF cavity Nb using magneto-optical and electron imaging methods. *Superconductor Science and Technology*, 35(4):045001, 2022.

[97] Denise C Ford, Lance D Cooley, and David N Seidman. First-principles calculations of niobium hydride formation in superconducting radio-frequency cavities. *Superconductor Science and Technology*, 26(9):095002, 2013.

[98] S Isagawa. Hydrogen absorption and its effect on low-temperature electric properties of niobium. *Journal of Applied Physics*, 51(8):4460–4470, 1980.

[99] Philip Bambade, Tim Barklow, Ties Behnke, Mikael Berggren, James Brau, Philip Burrows, Dmitri Denisov, Angeles Faus-Golfe, Brian Foster, Keisuke Fujii, et al. The international linear collider: a global project. *arXiv preprint arXiv:1903.01629*, 2019.

[100] Gianluigi Ciovati. Review of the frontier workshop and Q-slope results. *Physica C: Superconductivity*, 441(1-2):44–50, 2006.

[101] A. Gurevich. Multiscale mechanisms of SRF breakdown. *Physica C: Superconductivity*, 441(1-2):38–43, 2006.

[102] Alex Gurevich. Superconducting radio-frequency fundamentals for particle accelerators. *Reviews of Accelerator Science and Technology*, 5:119–146, 2012.

[103] Alex Gurevich. Theory of RF superconductivity for resonant cavities. *Superconductor Science and Technology*, 30(3):034004, 2017.

[104] Mark S. Champion, Lance D. Cooley, Camille M. Ginsburg, Dmitri A. Sergatskov, Rongli L. Geng, Hitoshi Hayano, Yoshihisa Iwashita, and Yujiro Tajima. Quench-limited SRF cavities: Failure at the heat-affected zone. *IEEE transactions on applied superconductivity*, 19(3):1384–1386, 2009.

[105] Shiran Bao and Wei Guo. Quench-spot detection for superconducting accelerator cavities via flow visualization in superfluid helium-4. *Physical Review Applied*, 11(4):044003, 2019.

[106] S. Posen, N. Valles, and M. Liepe. Radio frequency magnetic field limits of Nb and Nb3Sn. *Physical review letters*, 115(4):047001, 2015.

[107] P. Kneisel, G. Ciovati, P. Dhakal, K. Saito, W. Singer, Xenia Singer, and G.R. Myneni. Review of ingot niobium as a material for superconducting radiofrequency accelerating cavities. *Nuclear Instruments and Methods in Physics Research Section A: Accelerators, Spectrometers, Detectors and Associated Equipment*, 774:133–150, 2015.

[108] C.Z. Antoine. Influence of crystalline structure on rf dissipation in superconducting niobium. *Physical Review Accelerators and Beams*, 22(3):034801, 2019.

[109] Roberto Russo. Quality measurement of niobium thin films for Nb/Cu superconducting RF cavities. *Measurement Science and Technology*, 18(8):2299, 2007.

[110] Maxim Kharitonov, Thomas Proslier, Andreas Glatz, and Michael J. Pellin. Surface impedance of superconductors with magnetic impurities. *Physical Review B*, 86(2):024514, 2012.

[111] P.J. Lee, A.A. Polyanskii, Zu-Hawn Sung, D.C. Larbalestier, C. Antoine, P.C. Bauer, C. Boffo, and H.T. Edwards. Flux penetration into grain boundaries large grain niobium sheet for SRF cavities: Angular sensitivity. In *Single crystal and large grain international niobium workshop. 2006. Aranxa, Brazil, AIP Conference Proceedings*, volume 927, pages 113–120. American Institute of Physics, 2007.

[112] A.A. Polyanskii, P.J. Lee, A. Gurevich, Zu-Hawn Sung, and D.C. Larbalestier. Magneto-Optical study high-purity Niobium for superconducting RF application. In *Proceedings of the Symposium on the Superconducting Science and Technology of Ingot Niobium, Newport News VA, AIP Conference Proceedings*, volume 1352, pages 186–202. American Institute of Physics, 2011.

[113] J Köszegi, O. Kugeler, D. Abou-Ras, J. Knobloch, and R. Schäfer. A magneto-optical study on magnetic flux expulsion and pinning in high-purity niobium. *Journal of Applied Physics*, 122(17):173901, 2017.

[114] Mingmin Wang, Shreyas Balachandran, Thomas Bieler, Santosh Chetri, Chris Compton, Peter Lee, Anatolii Polyanskii, et al. Investigation of the effect of strategically selected grain boundaries on superconducting properties of SRF cavity niobium. In *Proceedings of the 18th International Conference on rf Superconductivity (SRF'17), Lanzhou, China, 2017 (JACoW, Geneva, Switzerland)*, pages 787–791, 2018.

[115] Jaeyel Lee, Zugang Mao, Kai He, Tiziana Spina, Sung-Il Baik, Daniel L. Hall, Matthias Liepe, David N. Seidman, Sam Posen, et al. Grain-boundary structure and segregation in Nb3Sn coatings on Nb for high-performance superconducting radiofrequency cavity applications. *Acta Materialia*, 188:155–165, 2020.

[116] A. Romanenko and H. Padamsee. The role of near-surface dislocations in the high magnetic field performance of superconducting niobium cavities. *Superconductor Science and Technology*, 23(4):045008, 2010.

[117] T.R. Bieler, N.T. Wright, F. Pourboghrat, C. Compton, K.T. Hartwig, D. Baars, A. Zamiri, S. Chandrasekaran, P. Darbandi, H. Jiang, et al. Physical and mechanical metallurgy of high purity Nb for accelerator cavities. *Physical Review Special Topics-Accelerators and Beams*, 13(3):031002, 2010.

[118] R. Ries, E. Seiler, F Gömöry, A. Medvids, C. Pira, and O.B. Malyshev. Superconducting properties and surface roughness of thin Nb samples fabricated for SRF applications. In *Journal of Physics: Conference Series*, volume 1559, page 012040. IOP Publishing, 2020.

[119] Pashupati Dhakal, Gianluigi Ciovati, Peter Kneisel, and Ganapati Rao Myneni. Enhancement in quality factor of SRF niobium cavities by material diffusion. *IEEE Transactions on Applied Superconductivity*, 25(3):1–4, 2014.

[120] Dan Gonnella, Matthias Liepe, et al. Cool down and flux trapping studies on SRF cavities. 2014.

[121] Raphael Kleindienst, Andrew Burrill, Oliver Kugeler, and Jens Knobloch. Commissioning results of the HZB quadrupole resonator. Technical report, 2015.

[122] S. Keckert, R. Kleindienst, O. Kugeler, D. Tikhonov, and J. Knobloch. Characterizing materials for superconducting radiofrequency applications—a comprehensive overview of the quadrupole resonator design and measurement capabilities. *Review of Scientific Instruments*, 92(6):064710, 2021.

[123] Marco Arzeo, F. Avino, S. Pfeiffer, G. Rosaz, M. Taborelli, L. Vega-Cid, and W. Venturini-Delsolaro. Enhanced radio-frequency performance of niobium films on copper substrates deposited by high power impulse magnetron sputtering. *Superconductor Science and Technology*, 35(5):054008, 2022.

[124] S. Keckert, W. Ackermann, H. De Gersem, X. Jiang, AÖ Sezgin, M. Vogel, M. Wenskat, R. Kleindienst, J. Knobloch, O. Kugeler, et al. Mitigation of parasitic losses in the quadrupole resonator enabling direct measurements of low residual resistances of SRF samples. *Aip Advances*, 11(12):125326, 2021.

[125] Colt James, Mahadevan Krishnan, Brian Bures, Tsuyoshi Tajima, Leonardo Civale, Randy Edwards, Josh Spradlin, and Hitoshi Inoue. Superconducting Nb thin films on Cu for applications in SRF accelerators. *IEEE transactions on applied superconductivity*, 23(3):3500205–3500205, 2012.

[126] Claire Z. Antoine, M. Aburas, A. Four, F. Weiss, Y. Iwashita, H. Hayano, S. Kato, Takayuki Kubo, and T. Saeki. Optimization of tailored multilayer superconductors for RF application and protection against premature vortex penetration. *Superconductor Science and Technology*, 32(8):085005, 2019.

[127] G. Lamura, M. Aurino, A. Andreone, and J-C Villégier. First critical field measurements of superconducting films by third harmonic analysis. *Journal of Applied Physics*, 106(5):053903, 2009.

[128] C.Z. Antoine, S. Berry, S. Bouat, J.F. Jacquot, J.C. Villegier, G. Lamura, and A. Gurevich. Characterization of superconducting nanometric multilayer samples for superconducting rf applications: First evidence of magnetic screening effect. *Physical Review Special Topics-Accelerators and Beams*, 13(12):121001, 2010.

[129] C.Z. Antoine, S. Berry, M. Aurino, J-F Jacquot, J-C Villegier, G. Lamura, and A. Andreone. Characterization of field penetration in superconducting multilayers samples. *IEEE Transactions on Applied Superconductivity*, 21(3):2601–2604, 2011.

[130] C.Z. Antoine, J-C Villegier, and G. Martinet. Study of nanometric superconducting multilayers for RF field screening applications. *Applied Physics Letters*, 102(10):102603, 2013.

[131] N. Katyan and C.Z. Antoine. Characterization of thin films using local magneometer. Technical report, 2015.

[132] Muhammad Aburas, C.Z. Antoine, Aurelien Four, et al. Local magnetometer: first critical field measurement of multilayer superconductors. In *Proc. 18th Int. Conf. RF Superconductivity (SRF'17)*, pages 830–834, 2017.

[133] Hayato Ito, H. Hayano, T. Kubo, T. Saeki, Y. Iwashita, R. Katayama, H. Tongu, Kyoto ICR, R. Ito, T. Nagata, et al. Lower critical field measurement of thin film superconductor. In *29\textsuperscript {th} Linear Accelerator Conf.(LINAC'18), Beijing, China, 16-21 September 2018*, pages 484–487. JACOW Publishing, Geneva, Switzerland, 2019.

[134] Hayato Ito, Hitoshi Hayano, Takayuki Kubo, and Takayuki Saeki. Vortex penetration field measurement system based on third-harmonic method for superconducting RF materials. *Nuclear Instruments and Methods in Physics Research Section A: Accelerators, Spectrometers, Detectors and Associated Equipment*, 955:163284, 2020.

[135] V. Arbet-Engels, Cristoforo Benvenuti, S. Calatroni, Pierre Darriulat, M.A. Peck, A-M Valente, and C.A. Van't Hof. Superconducting niobium cavities, a case for the film technology. *Nuclear Instruments and Methods in Physics Research Section A: Accelerators, Spectrometers, Detectors and Associated Equipment*, 463(1-2):1–8, 2001.

[136] Alban Sublet, Walter Venturini Delsolaro, Mathieu Therasse, Thibaut Richard, Guillaume Rosaz, Sarah Aull, Pei Zhang, Barbora Bártová, Sergio Calatroni, and Mauro Taborelli. Developments on SRF coatings at CERN. TUPB027:617–621, 2015.

[137] W.M. Roach, D.B. Beringer, J.R. Skuza, W.A. Oliver, C. Clavero, C.E. Reece, and R.A. Lukaszew. Niobium thin film deposition studies on copper surfaces for superconducting radio frequency cavity applications. *Physical Review Special Topics-Accelerators and Beams*, 15(6):062002, 2012.

[138] Guillaume Rosaz, Aleksandra Bartkowska, Carlota P.A. Carlos, Thibaut Richard, and Mauro Taborelli. Niobium thin film thickness profile tailoring on complex shape substrates using unbalanced biased High Power Impulse Magnetron Sputtering. *Surface and Coatings Technology*, 436:128306, 2022.

[139] M. Ghaemi, A. Lopez-Cazalilla, K. Sarakinos, G.J. Rosaz, C.P.A. Carlos, S. Leith, S. Calatroni, M. Himmerlich, and F. Djurabekova. Growth of Nb films on Cu for superconducting radio frequency cavities by direct current and high power impulse magnetron sputtering: A molecular dynamics and experimental study. *Surface and Coatings Technology*, page 130199, 2024.

[140] S. Posen, M. Liepe, and D.L. Hall. Proof-of-principle demonstration of Nb3Sn superconducting radiofrequency cavities for high Q applications. *Applied Physics Letters*, 106(8):082601, 2015.

[141] Sam Posen and Daniel Leslie Hall. Nb3Sn superconducting radiofrequency cavities: fabrication, results, properties, and prospects. *Superconductor Science and Technology*, 30(3):033004, 2017.

[142] Y. Trenikhina, S. Posen, A. Romanenko, M. Sardela, J.M. Zuo, D.L. Hall, and M. Liepe. Performance-defining properties of Nb3Sn coating in SRF cavities. *Superconductor Science and Technology*, 31(1):015004, 2017.

[143] E.A. Ilyina, Guillaume Rosaz, Josep Busom Descarrega, Wilhelmus Vollenberg, AJG Lunt, Floriane Leaux, Sergio Calatroni, W. Venturini-Delsolaro, and Mauro Taborelli. Development of sputtered Nb3Sn films on copper substrates for superconducting radiofrequency applications. *Superconductor Science and Technology*, 32(3):035002, 2019.

[144] Alexander Gurevich. Enhancement of rf breakdown field of superconductors by multilayer coating. *Applied Physics Letters*, 88(1):012511, 2006.

[145] Takayuki Kubo, Yoshihisa Iwashita, and Takayuki Saeki. Radio-frequency electromagnetic field and vortex penetration in multilayered superconductors. *Applied Physics Letters*, 104(3):032603, 2014.

[146] Takayuki Kubo. Multilayer coating for higher accelerating fields in superconducting radio-frequency cavities: a review of theoretical aspects. *Superconductor Science and Technology*, 30(2):023001, 2016.

[147] S. Calatroni. 20 years of experience with the Nb/Cu technology for superconducting cavities and perspectives for future developments. *Physica C: Superconductivity*, 441(1-2):95–101, 2006.

[148] Cristoforo Benvenuti, N. Circelli, and M. Hauer. Niobium films for superconducting accelerating cavities. *Applied Physics Letters*, 45(5):583–584, 1984.

[149] Sarah Aull, Walter Venturini Delsolaro, Tobias Junginger, Anne-Marie Valente-Feliciano, Jens Knobloch, Alban Sublet, and Pei Zhang. On the understanding of Q-slope of niobium thin films. 2015.

[150] V. Palmieri and R. Vaglio. Thermal contact resistance at the Nb/Cu interface as a limiting factor for sputtered thin film RF superconducting cavities. *Superconductor Science and Technology*, 29(1):015004, 2015.

[151] Antonio Bianchi, Marco Bonura, Carlota PA Carlos, Stewart Leith, Guillaume Rosaz, Carmine Senatore, and Walter Venturini Delsolaro. Thickness effect on superconducting properties of niobium films for radio-frequency cavity applications. *Superconductor Science and Technology*, 37(8):085005, 2024.

[152] L. Vega Cid, G. Bellini, A. Bianchi, L.M.A. Ferreira, S.B. Leith, C. Pereira Carlos, G.J. Rosaz, and W. Venturini Delsolaro. Results of the R&D RF Testing Campaign of 1.3 GHz Nb/Cu Cavities. In *Proc. 21th Int. Conf. RF Supercond. (SRF'23)*, number 21 in International Conference on RF Superconductivity, pages 621–626. JACoW Publishing, Geneva, Switzerland, 09 2023.

[153] Ryohei Wakatsuki, Yu Saito, Shintaro Hoshino, Yuki M. Itahashi, Toshiya Ideue, Motohiko Ezawa, Yoshihiro Iwasa, and Naoto Nagaosa. Nonreciprocal charge transport in noncentrosymmetric superconductors. *Science Advances*, 3(4):e1602390, 2017.

[154] Yuki M. Itahashi, Yu Saito, Toshiya Ideue, Tsutomu Nojima, and Yoshihiro Iwasa. Quantum and classical ratchet motions of vortices in a two-dimensional trigonal superconductor. *Phys. Rev. Res.*, 2:023127, May 2020.

[155] C-S Lee, Boldizsar Janko, Imre Derenyi, and A-L Barabási. Reducing vortex density in superconductors using the 'ratchet effect'. *Nature*, 400(6742):337–340, 1999.

[156] Clécio C. de Souza Silva, J. Van de Vondel, B. Y. Zhu, M. Morelle, and V. V. Moshchalkov. Vortex ratchet effects in films with a periodic array of antidots. *Phys. Rev. B*, 73:014507, Jan 2006.

[157] Britton LT Plourde. Nanostructured superconductors with asymmetric pinning potentials: Vortex ratchets. *IEEE transactions on applied superconductivity*, 19(5):3698–3714, 2009.

[158] B. B. Jin, B. Y. Zhu, R. Wördenweber, C. C. de Souza Silva, P. H. Wu, and V. V. Moshchalkov. High-frequency vortex ratchet effect in a superconducting film with a nanoengineered array of asymmetric pinning sites. *Phys. Rev. B*, 81:174505, May 2010.

[159] Jonathan I. Gittleman and Bruce Rosenblum. Radio-Frequency resistance in the mixed state for subcritical currents. *Phys. Rev. Lett.*, 16:734–736, Apr 1966.

[160] Mark W. Coffey and John R. Clem. Unified theory of effects of vortex pinning and flux creep upon the rf surface impedance of type-II superconductors. *Phys. Rev. Lett.*, 67:386–389, Jul 1991.

[161] C. Benvenuti, S. Calatroni, I.E. Campisi, P. Darriulat, M.A. Peck, R. Russo, and A.-M. Valente. Study of the surface resistance of superconducting niobium films at 1.5 GHz. *Physica C: Superconductivity*, 316(3):153–188, 1999.

[162] G. Ciovati and A. Gurevich. Evidence of high-field radio-frequency hot spots due to trapped vortices in niobium cavities. *Phys. Rev. ST Accel. Beams*, 11:122001, Dec 2008.

[163] S. Aull, O. Kugeler, and J. Knobloch. Trapped magnetic flux in superconducting niobium samples. *Phys. Rev. ST Accel. Beams*, 15:062001, Jun 2012.

[164] A. Gurevich and G. Ciovati. Effect of vortex hotspots on the radio-frequency surface resistance of superconductors. *Phys. Rev. B*, 87:054502, Feb 2013.

[165] A. Romanenko, A. Grassellino, A. C. Crawford, D. A. Sergatskov, and O. Melnychuk. Ultra-high quality factors in superconducting niobium cavities in ambient magnetic fields up to 190 mG. *Applied Physics Letters*, 105(23):234103, 12 2014.

[166] A. Romanenko, A. Grassellino, O. Melnychuk, and D. A. Sergatskov. Dependence of the residual surface resistance of superconducting radio frequency cavities on the cooling dynamics around Tc. *Journal of Applied Physics*, 115(18):184903, 05 2014.

[167] Dan Gonnella, John Kaufman, and Matthias Liepe. Impact of nitrogen doping of niobium superconducting cavities on the sensitivity of surface resistance to trapped magnetic flux. *Journal of Applied Physics*, 119(7):073904, 02 2016.

[168] S. Posen, M. Checchin, A. C. Crawford, A. Grassellino, M. Martinello, O. S. Melnychuk, A. Romanenko, D. A. Sergatskov, and Y. Trenikhina. Efficient expulsion of magnetic flux in superconducting radiofrequency cavities for high Q applications. *Journal of Applied Physics*, 119(21):213903, 06 2016.

[169] Pashupati Dhakal and Gianluigi Ciovati. Effect of cooldown and residual magnetic field on the performance of niobium–copper clad superconducting radio-frequency cavity. *Superconductor Science and Technology*, 31(1):015006, nov 2017.

[170] M Checchin, M Martinello, A Grassellino, A Romanenko, and J F Zasadzinski. Electron mean free path dependence of the vortex surface impedance. *Superconductor Science and Technology*, 30(3):034003, jan 2017.

[171] Danilo B. Liarte, Daniel Hall, Peter N. Koufalis, Akira Miyazaki, Alen Senanian, Matthias Liepe, and James P. Sethna. Vortex dynamics and losses due to pinning: Dissipation from trapped magnetic flux in resonant superconducting radio-frequency cavities. *Phys. Rev. Appl.*, 10:054057, Nov 2018.

[172] B D Khanal, S Balachandran, S Chetri, M Barron, R Mullinix, A Williams, P Xu, A Ingrole, P J Lee, G Ciovati, and P Dhakal. Role of microstructure on flux expulsion of superconducting radio frequency cavities. *Superconductor Science and Technology*, 38(1):015015, dec 2024.

[173] C. Song, M. P. DeFeo, K. Yu, and B. L. T. Plourde. Reducing microwave loss in superconducting resonators due to trapped vortices. *Applied Physics Letters*, 95(23):232501, 12 2009.

[174] C. Song, T. W. Heitmann, M. P. DeFeo, K. Yu, R. McDermott, M. Neeley, John M. Martinis, and B. L. T. Plourde. Microwave response of vortices in superconducting thin films of Re and Al. *Phys. Rev. B*, 79:174512, May 2009.

[175] Serena Eley, Andreas Glatz, and Roland Willa. Challenges and transformative opportunities in superconductor vortex physics. *Journal of Applied Physics*, 130(5):050901, 08 2021.

[176] I. Nsanzineza and B. L. T. Plourde. Trapping a single vortex and reducing quasiparticles in a superconducting resonator. *Phys. Rev. Lett.*, 113:117002, Sep 2014.

[177] S. Bermon and T. Gheewala. Moat-guarded Josephson SQUIDs. *IEEE Transactions on Magnetics*, 19(3):1160–1164, 1983.

[178] Mark Jeffery, T. Van Duzer, J. R. Kirtley, and M. B. Ketchen. Magnetic imaging of moat-guarded superconducting electronic circuits. *Applied Physics Letters*, 67(12):1769–1771, 09 1995.

[179] K Suzuki, H Kawamura, M Maruyama, T Hato, H Suzuki, S Yorozu, Y Kameda, Y Ishimaru, K Nakayama, H Wakana, S Adachi, Y Tarutani, and K Tanabe. Investigation of the flux state in single-flux-quantum circuits with moats by scanning SQUID microscope. *Superconductor Science and Technology*, 19(5):S316, mar 2006.

[180] Yuri Polyakov, Supradeep Narayana, and Vasili K. Semenov. Flux trapping in superconducting circuits. *IEEE Transactions on Applied Superconductivity*, 17(2):520–525, 2007.

[181] Supradeep Narayana, Yuri A. Polyakov, and Vasili K. Semenov. Evaluation of flux trapping in superconducting circuits. *IEEE Transactions on Applied Superconductivity*, 19(3):640–643, 2009.

[182] Kan Fujiwara, Shuichi Nagasawa, Yoshihito Hashimoto, Mutsuo Hidaka, Nobuyuki Yoshikawa, Masamitsu Tanaka, Hiroyuki Akaike, Akira Fujimaki, Kazuyoshi Takagi, and Naofumi Takagi. Research on effective moat configuration for Nb multi-layer device structure. *IEEE Transactions on Applied Superconductivity*, 19(3):603–606, 2009.

[183] Vasili K. Semenov and Mikhail M. Khapaev. How moats protect superconductor films from flux trapping. *IEEE Transactions on Applied Superconductivity*, 26(3):1300710, 2016.

[184] Kyle Jackman and Coenrad Johann Fourie. Flux trapping analysis in superconducting circuits. *IEEE Transactions on Applied Superconductivity*, 27(4):1300105, 2017.

[185] Uday S. Goteti, Han Cai, Jay C. LeFebvre, Shane A. Cybart, and Robert C. Dynes. Superconducting disordered neural networks for neuromorphic processing with fluxons. *Science Advances*, 8(16):eabn4485, 2022.

[186] Lieze Schindler, Christopher L. Ayala, Naoki Takeuchi, and Nobuyuki Yoshikawa. The effect of quantised flux on AQFP circuits for a double-active-layered Niobium fabrication process. *IEEE Transactions on Applied Superconductivity*, 34(3):1100908, 2024.

[187] W. P. M. R. Pathirana and A. Gurevich. Effect of random pinning on nonlinear dynamics and dissipation of a vortex driven by a strong microwave current. *Phys. Rev. B*, 103:184518, May 2021.

[188] M. Golosovsky, M. Tsindlekht, H. Chayet, and D. Davidov. Vortex depinning frequency in YBa2Cu3O7$-x$ superconducting thin films: Anisotropy and temperature dependence. *Phys. Rev. B*, 50:470–477, Jul 1994.

[189] V. V. Moshchalkov, M. Baert, V. V. Metlushko, E. Rosseel, M. J. Van Bael, K. Temst, Y. Bruynseraede, and R. Jonckheere. Pinning by an antidot lattice: The problem of the optimum antidot size. *Phys. Rev. B*, 57:3615–3622, Feb 1998.

[190] S. Raedts, A. V. Silhanek, M. J. Van Bael, and V. V. Moshchalkov. Flux-pinning properties of superconducting films with arrays of blind holes. *Phys. Rev. B*, 70:024509, Jul 2004.

[191] A. V. Silhanek, L. Van Look, R. Jonckheere, B. Y. Zhu, S. Raedts, and V. V. Moshchalkov. Enhanced vortex pinning by a composite antidot lattice in a superconducting Pb film. *Phys. Rev. B*, 72:014507, Jul 2005.

[192] Pedro-de-Jesús Cuadra-Solís, Antoni Fernández-Martínez, Joan Manel Hernàndez, Antoni García-Santiago, Johan Vanacken, and Victor V. Moshchalkov. A radio-frequency coil for the microwave characterization of vortex dynamics in thin film superconductors. *Review of Scientific Instruments*, 86(6):064701, 06 2015.

[193] Andrea Alimenti, Nicola Pompeo, Kostiantyn Torokhtii, Tiziana Spina, René Flükiger, Luigi Muzzi, and Enrico Silva. Microwave measurements of the high magnetic field vortex motion pinning parameters in Nb3Sn. *Superconductor Science and Technology*, 34(1):014003, Nov 2020.

[194] M. S. Pambianchi, D. H. Wu, L. Ganapathi, and S. M. Anlage. DC magnetic field dependence of the surface impedance in superconducting parallel plate transmission line resonators. *IEEE Transactions on Applied Superconductivity*, 3(1):2774–2777, 1993.

[195] Dong Ho Wu, J. C. Booth, and Steven M. Anlage. Frequency and field variation of vortex dynamics in YBa2Cu3O7$-\delta$. *Phys. Rev. Lett.*, 75:525–528, Jul 1995.

[196] Viacheslav V Dremov, Sergey Yu Grebenchuk, Andrey G Shishkin, Denis S Baranov, Razmik A Hovhannisyan, Olga V Skryabina, Nickolay Lebedev, Igor A Golovchanskiy, Vladimir I Chichkov, Christophe Brun, et al. Local Josephson vortex generation and manipulation with a magnetic force microscope. *Nature communications*, 10(1):4009, 2019.

[197] Lior Embon, Yonathan Anahory, Alexander Suhov, Dorri Halbertal, Jo Cuppens, Anton Yakovenko, Aviram Uri, Yuri Myasoedov, Michael L Rappaport, Martin E Huber, et al. Probing dynamics and pinning of single vortices in superconductors at nanometer scales. *Scientific reports*, 5(1):7598, 2015.

[198] Logan Bishop-Van Horn, Eli Mueller, and Kathryn A. Moler. Vortex dynamics induced by scanning SQUID susceptometry. *Phys. Rev. B*, 107:224509, Jun 2023.

[199] Marek Foltyn, Konrad Norowski, Alexander Savin, and Maciej Zgirski. Quantum thermodynamics with a single superconducting vortex. *Science Advances*, 10(31):eado4032, 2024.

[200] An-Lei Zhang, Cun Xue, and Jun-Yi Ge. Direct imaging of vortex pinning at artificial antidots with different geometries. *Applied Physics Letters*, 115(13):132601, 09 2019.

[201] C. Chen, Y. Liu, Y. Chen, Y. N. Hu, T. Z. Zhang, D. Li, X. Wang, C. X. Wang, Z. Y. W. Lu, Y. H. Zhang, Q. L. Zhang, X. L. Dong, R. Wang, D. L. Feng, and T. Zhang. Revealing the microscopic mechanism of elementary vortex pinning in superconductors. *Phys. Rev. X*, 14:041039, Nov 2024.

[202] G. R. Berdiyorov, M. V. Milošević, and F. M. Peeters. Novel commensurability effects in superconducting films with antidot arrays. *Phys. Rev. Lett.*, 96:207001, May 2006.

[203] G. R. Berdiyorov, M. V. Milošević, and F. M. Peeters. Superconducting film with weak pinning centers: Incommensurate vortex lattices. *Phys. Rev. B*, 76:134508, Oct 2007.

[204] S. C. Sanders, J. Sok, D. K. Finnemore, and Qiang Li. Thermally activated hopping of a single Abrikosov vortex. *Phys. Rev. B*, 47:8996–9000, Apr 1993.

[205] M. R. Beasley, R. Labusch, and W. W. Webb. Flux creep in type-II superconductors. *Phys. Rev.*, 181:682–700, May 1969.

[206] Junghyun Sok and D. K. Finnemore. Thermal depinning of a single superconducting vortex in Nb. *Phys. Rev. B*, 50:12770–12773, Nov 1994.

[207] J. Gail, M. Mück, and C. Heiden. Pinning and depinning of single vortices in niobium thin film dc superconducting quantum interference devices. *Applied Physics Letters*, 73(18):2663–2665, 11 1998.

[208] Y. Yeshurun and A. P. Malozemoff. Giant flux creep and irreversibility in an Y-Ba-Cu-O crystal: An alternative to the superconducting-glass model. *Phys. Rev. Lett.*, 60:2202–2205, May 1988.

[209] M. Tinkham. Resistive transition of high-temperature superconductors. *Phys. Rev. Lett.*, 61:1658–1661, Oct 1988.

[210] J. I. Martín, M. Vélez, A. Hoffmann, Ivan K. Schuller, and J. L. Vicent. Temperature dependence and mechanisms of vortex pinning by periodic arrays of Ni dots in Nb films. *Phys. Rev. B*, 62:9110–9116, Oct 2000.

[211] Y. Z. Zhang, H. H. Wen, and Z. Wang. Thermally activated energies of YBa2Cu3O7$-\delta$ and Y0.8Ca0.2Ba2Cu3O7$-\delta$ thin films. *Phys. Rev. B*, 74:144521, Oct 2006.

[212] Y Z Zhang, Z A Ren, and Z X Zhao. Thermally activated energy and critical magnetic fields of SmFeAsO0.9F0.1. *Superconductor Science and Technology*, 22(6):065012, apr 2009.

[213] WJ Choi, YI Seo, D Ahmad, and Yong Seung Kwon. Thermal activation energy of 3D vortex matter in NaFe1-xCoxAs (x= 0.01, 0.03 and 0.07) single crystals. *Scientific Reports*, 7(1):10900, 2017.

[214] Sameh M. Altanany, I. Zajcewa, T. Zajarniuk, A. Szewczyk, and Marta Z. Cieplak. Vortex dynamics in disordered niobium thin films. *Phys. Rev. B*, 109:214504, Jun 2024.

[215] Zeming Sun, Zhaslan Baraissov, Catherine A Dukes, Darrah K Dare, Thomas Oseroff, Michael O Thompson, David A Muller, and Matthias U Liepe. Surface oxides, carbides, and impurities on rf superconducting Nb and Nb3Sn: A comprehensive analysis. *Superconductor Science and Technology*, 36(11):115030, 2023.

[216] Katrina Howard, Matthias U. Liepe, and Zeming Sun. Thermal annealing of DC sputtered Nb3Sn and V3Si thin films for superconducting radio-frequency cavities. *Journal of Applied Physics*, 134(22):225301, 12 2023.

[217] Zeming Sun, G Gaitan, M Ge, K Howard, MU Liepe, RD Porter, T Oseroff, T Arias, Z Baraissov, Michelle Kelly, et al. Toward stoichiometric and low-surface-roughness Nb3Sn thin films via direct electrochemical deposition. *Proc. SRF'21*, pages 516–521, 2021.

[218] Zeming Sun, Zhaslan Baraissov, Ryan D Porter, Liana Shpani, Yu-Tsun Shao, Thomas Oseroff, Michael O Thompson, David A Muller, and Matthias U Liepe. Smooth, homogeneous, high-purity Nb3Sn superconducting rf resonant cavity by seed-free electrochemical synthesis. *Superconductor Science and Technology*, 36(11):115003, 2023.